



UPPSALA
UNIVERSITET

UPTEC XX XXXXX

Degree project 30 credits

January, 2026

Annealing and Radiation Hardness Studies of p-type Silicon Diodes for CMS HGCAL under HL-LHC Fluence and Annealing Conditions

Max Andersson

Degree: Master of Science in Engineering
Specialisation: Engineering Physics

A large, faint watermark of the Uppsala University seal is visible in the background, centered on the page.



UPPSALA
UNIVERSITET

Annealing and Radiation Hardness Studies of p-type Silicon Diodes for CMS HGCAL under HL-LHC Fluence and Annealing Conditions

Max Andersson

Abstract

To handle the higher levels of radiation expected from the 10-fold increase in integrated luminosity during the High Luminosity LHC, the endcap calorimeters of the CMS detector will be replaced by the High Granularity Calorimeter (HGCAL). Hexagonal silicon pad sensor, fabricated on 8-inch p-type silicon wafers with active thicknesses of 300 µm, 200 µm, and 120 µm, will cover 620 m² of the HGCAL, resulting in more than 6 M silicon readout channels. The remaining wafer space from the hexagonal cut hosts small test structures for quality assurance and radiation hardness studies.

A previous annealing study investigated silicon diodes exposed to fluences corresponding to the end of the HL-LHC of $2 \cdot 10^{15}$ to $1.5 \cdot 10^{16}$ n_{eq}/cm². In a more realistic operational scenario, the detector accumulates fluence over 10 years with a two-year maintenance break in between, corresponding to Long Shutdown 4, which allows the sensors to anneal. In this study, diodes were initially exposed to one quarter of the final fluence, followed by in between annealing at 20.5 °C, 40 °C, and 60 °C, before further irradiation to reach fluences comparable to the previous study. Charge collection efficiency, saturation voltage, and leakage current damage rate are compared between the two studies to investigate the effect of the in between annealing.

Results show that in between annealing of the first quarter of the fluence generally improves the electrical characteristics of all diodes across all temperatures. Thickness and fluence dependencies are observed in the charge collection efficiency and saturation voltage. Thicker diodes exhibit a more substantial reduction of the beneficial effect with increasing fluence, whereas thinner diodes show no significant impact from the in between annealing. As a result, this study improves the understanding of the expected behaviour of silicon sensors in the HGCAL during the HL-LHC phase.

Keywords: *Silicon Sensors, Radiation Damage, Annealing, CMS, HGCAL, HL-LHC*

Faculty of Science and Technology

Uppsala University, Place of publication: Uppsala

Supervisors: Dr. Leena Diehl, Dr. Eva Sicking Subject reader: Dr. Geoffrey Mullier

Examiner: Dr. Tomas Nyberg

Populärvetenskaplig Sammanfattning

Sedan 2008 har CERN accelererat partiklar i motsatta riktningar runt en 27 kilometer lång ring till 99.9999991 % av ljusets hastighet. Partiklarna kolliderar vid fyra experiment, CMS, ATLAS, ALICE, och LHCb, för att studera universums fundamentala byggstenar. Den nuvarande acceleratoren, Large Hadron Collider (LHC), har bland annat lett till upptäckten av Higgsbosonen, belönad med Nobelpriset, och därmed bekräftat mekanismen som ger massa åt elementarpartiklar inom standardmodellen. För att möjliggöra studier av fenomen bortom standardmodellen, såsom supersymmetri och mörk materia, samt för att förbättra precisionen i Higgsfysik, kommer LHC att uppgraderas till High Luminosity LHC. Uppgraderingen innebär en kraftig ökning av antalet proton-proton kollisioner och därmed betydligt högre nivåer av strålning.

De nuvarande detektorerna är inte konstruerade för dessa strålningsmängder, vilket kräver att flera komponenter ersätts. I CMS-experimentet kommer endcap calorimeter att bytas ut mot High Granularity Calorimeter (HGCAL). HGCAL byggs av totalt 620 m^2 hexagonala kiselbaserade sensorer tillverkade på wafers med en diameter på 20.32 cm och med tjocklekar på 300 μm , 200 μm , och 120 μm . Den resterande ytan av dessa wafers innehåller teststrukturer med motsvarande materialegenskaper, vilka används för kvalitetskontroll och för studier av strålningsinducerande förändringar som påverkar de elektriska egenskaperna.

En tidigare studie undersökte hur de elektriska egenskaperna hos kiselsensorer förändras vid neutronstrålning upp till $1.5 \cdot 10^{16}\text{ n}_{\text{eq}}/\text{cm}^2$ samt hur dessa påverkas av termisk uppvärmning. I ett mer realistisk driftscenario ackumulerar detektorn strålning med tiden under en tioårsperiod, med tekniska stopp emellan som möjliggör att sensorerna ”läker” genom uppvärmning. I denna studie exponerades sensorerna först för neutronstrålning mellan $5 \cdot 10^{14}$ till $5 \cdot 10^{15}\text{ n}_{\text{eq}}/\text{cm}^2$, för att sedan värmas upp vid tre olika temperaturer, 20.5 °C, 40 °C, and 60 °C. Därefter exponerades sensorerna för ytterligare strålning motsvarande den tidigare studien, för att kunna jämföra de elektriska egenskaperna och undersöka effekten från den mellanliggande uppvärmningen.

Resultatet visar att den mellanliggande uppvärmningen generellt förbättrar de elektriska egenskaperna hos sensorerna vid samtliga temperaturer. Dess effekt beror både på sensorernas tjocklek men också på strålningsmängden. Tjockare sensorer visar en starkare förändring vid ökande strålningsmängd, medan tunnare sensorer påverkas mindre av den mellanliggande uppvärmningen. Denna studie förbättrar förståelsen för hur kiselsensorernas elektriska egenskaper förändras i HGCAL under HL-LHC fasen.

Acknowledgement

I want to express my gratitude to my supervisors, Dr. Leena Diehl and Dr. Eva Sicking, and to my colleague, Marie Christin Mühlinkel, at CERN, for their excellent guidance, support, and insightful feedback. Thank you to all in the Silicon State Detector group at CERN who helped me along the way and allowed me to use their laboratory equipment. I would also like to thank my subject reader, Dr. Geoffrey Mullier at Uppsala University, for his continuous feedback on my thesis and valuable advice. Finally, I thank CERN for the opportunity to work and write my thesis in such an inspiring environment.

List of Abbreviations and Acronyms

Abbreviation	Description
CERN	European Organisation for Nuclear Research
LHC	Large Hadron Collider
SM	Standard Model
BSM	Beyond the Standard Model
HL-LHC	High-Luminosity Large Hadron Collider
CMS	Compact Muon Solenoid
ECAL	Electromagnetic Calorimeter
HCAL	Hadron Calorimeter
HGCAL	High-Granularity Calorimeter
CE-E	Electromagnetic Endcap Calorimeter
CE-H	Hadronic Endcap Calorimeter
FZ	Float Zone
EPI	Epitaxial
LD	Low Density
HD	High Density
HF	High Fluence (campaign)
DI	Double Irradiation (campaign)
DI SR	Double Irradiation Second Round (campaign)
HEP	High Energy Physics
CCE	Charge Collection Efficiency
PCB	Printed Circuit Board
IV	Current-Voltage (measurement)
CV	Capacitance-Voltage (measurement)
TCT	Transient Current Technique (measurement)
DUT	Device Under Test
TRIGA	Training, Research, Isotopes, General Atomics (reactor)
HV	High Voltage
GUI	Graphical User Interface

Contents

1	Introduction to CERN & CMS	1
1.1	CERN and Large Hadron Collider	1
1.2	Standard Model	2
1.3	High-Luminosity LHC	3
1.4	CMS	3
1.4.1	Magnet System	4
1.4.2	Tracking System	4
1.4.3	Calorimeter System	5
1.4.4	Muon System	5
1.5	Current Limitations of CMS	6
1.6	High Granularity Calorimeter	8
1.7	Thesis Objective, Contributions & Outline	10
2	Silicon Sensors	11
2.1	Material Properties	11
2.1.1	Energy Band	11
2.1.2	Bond Model of Semiconductors	13
2.2	Intrinsic Semiconductors	13
2.2.1	Carrier Concentration, Fermi Level, Density of States	13
2.2.2	Mobility, Drift Velocity and Scattering	14
2.3	Extrinsic Semiconductors	15
2.3.1	Doping	15
2.3.2	PN-Junction	16
2.3.3	PN-Junction under External Voltage	18
2.4	Silicon Sensor Characteristics	19
2.4.1	Leakage Current	20
2.4.2	Capacitance and Depletion Voltage	20
2.4.3	Effective Doping Concentration	21
2.4.4	Charge Collection	21
3	Radiation Damage & Annealing	23
3.1	Radiation Damage Mechanism	23
3.2	Change of Sensor Characteristics	25
3.2.1	Leakage Current	25
3.2.2	Effective Doping Concentration	26
3.2.3	Trapping	26
3.3	Annealing	27
3.3.1	Leakage Current	27
3.3.2	Effective Doping Concentration	28
4	Methodology	30
4.1	Silicon Wafer and Test Diodes	30
4.2	Campaign Overview & Irradiation of Unpowered Test Diodes	32
4.3	Measurement Setups	34
4.3.1	IVCV Setup - Probe Station	34

4.3.2	IVCV & TCT Setup - Test Diode on PCB	35
4.3.3	IVCV & TCT Software Development	37
4.4	Data Analysis - Developed Python GUI	37
4.4.1	Saturation Voltage Extraction: CV & TCT Measurements	39
4.5	Annealing	40
4.6	Uncertainties	42
5	Results and Discussion	43
5.1	Charge Collection Efficiency	43
5.2	Saturation Voltage	49
5.3	Leakage Current	55
6	Summary	62
6.1	Radiation Hardness and Annealing Effects of Electrical Characteristics . .	62
6.2	Limitations and Future Work	63
Bibliography		65
A	Appendices	68
A.1	Schedule and Expected Integrated Luminosity of LHC & HL-LHC	68
A.2	Leakage Current Deviation from IVCV Probe Station	69
A.3	Charge Collection Efficiency at 400 V and 800 V	70
A.4	Electrical Characteristics Ratios with Shifted Annealing Time	71

CHAPTER 1

INTRODUCTION TO CERN & CMS

This chapter first provides an overview of the European Organisation for Nuclear Research (CERN, *Conseil Européen pour la Recherche Nucléaire*) and the Large Hadron Collider (LHC) in §1.1, introducing key performance parameters such as integrated luminosity, instantaneous luminosity, and bunch crossing. These concepts provide the basis for understanding the performance expected from the High-Luminosity LHC (HL-LHC). A brief introduction to the Standard Model (SM) is given in §1.2. The Compact Muon Solenoid (CMS), one of the four detectors around the LHC, is presented in §1.4, which describes how particles are tracked and measured in the CMS detector. The limitations of the current CMS design in the HL-LHC environment are discussed in §1.5. A planned CMS upgrade involves replacing the current endcaps with the High Granularity Calorimeter (HGCAL), as described in §1.6. Finally, §1.7 outlines the thesis objective, describes the contributions, and provides an overview of the remaining chapters.

1.1 CERN and Large Hadron Collider

CERN was established in 1954 and has become a central organisation for particle physics research, involving scientists from around the world. In 2008, CERN launched the start of the Large Hadron Collider, a 27-kilometre ring crossing the Swiss-French border near Geneva, which has since become the world’s largest and most powerful particle accelerator.

The LHC consists of superconducting dipoles, quadrupole magnets, and radiofrequency cavities, bending, focusing, and accelerating particles in opposite directions. The dipole magnets operates at 1.9 Kelvin at 11 850 Ampere to produce a magnetic field of 8.33 Tesla to bend the particles around the LHC at a speed of 99.9999991 % of the speed of light, delivering centre-of-mass energies collisions up to 13.6 TeV at the four detectors, CMS, ATLAS, ALICE and LHCb [1].

During Run 3 in 2024, over 21 weeks of proton-proton collisions, the CMS experiment collected a large amount of data that illustrates the capabilities of the LHC. Over this period, CMS accumulated an integrated luminosity of 122.2 fb^{-1} , corresponding to 12.3 quadrillion proton-proton collisions, providing sufficient statistics to study rare physics phenomena, such as the Higgs Mechanism [2]. The maximum instantaneous luminosity, which reflects how tightly particles are packed into a given space and indicates the number of potential collisions per surface unit, reached $2.2 \cdot 10^{34} \text{ cm}^{-2}\text{s}^{-1}$, with a maximum of 60 collisions per bunch crossing. Each bunch crossing contains about 10 billion protons on each side, and the number of collisions per crossing is referred to as pileup. At this energy, and with the large amount of data collected, measurement of fundamental particle interactions and rare processes becomes possible, allowing predictions of the SM and search for physics Beyond the Standard Model (BSM).

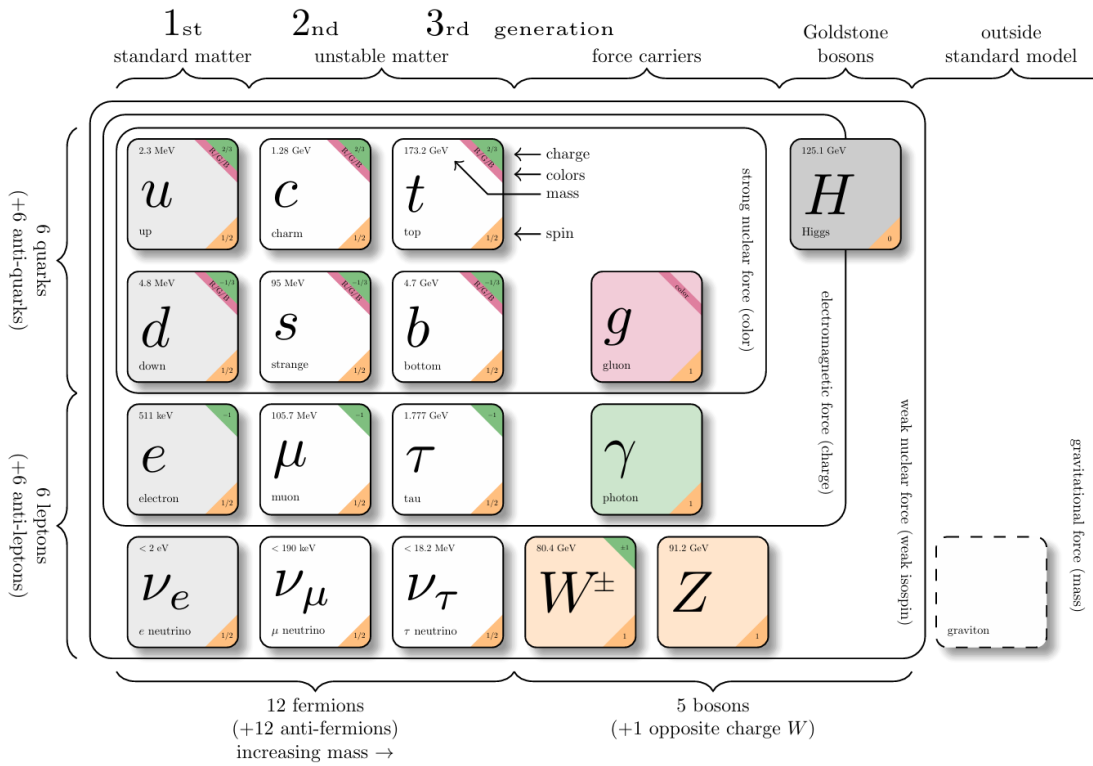


Figure 1.1.1: The SM is divided into six quarks, six leptons, and five bosons. The fermions appear in three generations, with higher generations corresponding to higher masses. Neutrino masses are shown but are not part of the SM. The graviton is a theoretical elementary particle proposed to mediate the gravitational interaction and is associated with physics beyond the SM. Credit: [3].

1.2 Standard Model

The SM is the most precisely tested theory of elementary particles, but remains incomplete, as it does not explain neutrino masses, dark matter, dark energy, the matter-antimatter asymmetry, or gravity. It identifies 12 fundamental fermions, which are spin-1/2 particles and are considered the basic building blocks of matter. Their interactions are mediated by force-carrier particles known as bosons, which have integer spin. Photons mediate electromagnetic interactions, W and Z bosons govern weak interactions, and gluons mediate strong interactions. The SM accounts for three of the four fundamental forces, but not gravity, because a quantum theory of gravity compatible with the SM does not yet exist [4].

An overview of the fundamental particles and their corresponding force carriers is shown in Figure 1.1.1. In the three left columns, the fermions, divided into six quarks and six leptons, are the elementary particles that form the building blocks of matter. Each fermion has a corresponding antiparticle, with identical mass but opposite charge. Because of fermions' defined half-integer spin, they obey the Pauli exclusion principle, which prohibits two identical fermions from occupying the same quantum state.

In 2012, the ATLAS and CMS experiments at CERN confirmed the discovery of the Higgs boson, the only known scalar boson [4, 5]. This discovery confirmed the mechanism through which elementary particles acquire mass via interactions with the Higgs field.

To enable a more precise and detailed study of the SM and Higgs physics, and to increase sensitivity to hypothetical rare physics BSM phenomena, the integrated luminosity, i.e., the total number of collisions recorded over a specific time, must increase.

1.3 High-Luminosity LHC

The LHC will undergo an upgrade to the HL-LHC during Long Shutdown 3, after Run 3, enabling higher luminosity and improved sensitivity to rare physics BSM phenomena, with operations expected to begin in September 2026 [6]. The primary physics motivations include precision studies of the Higgs boson, such as its Yukawa couplings and self-coupling, as well as searches for physics BSM, including Supersymmetry, additional gauge bosons, and extra dimensions.

The HL-LHC is expected to reach instantaneous peak luminosities of $5 \cdot 10^{34} \text{ cm}^{-2}\text{s}^{-1}$ to $7.5 \cdot 10^{34} \text{ cm}^{-2}\text{s}^{-1}$, together with an average pileup of 140 to 200 events per bunch crossing separated with 25 ns. This will enable the CMS experiment to obtain yearly integrated luminosities of 300 fb^{-1} , integrating to a total of 3000 fb^{-1} during the 10-year lifetime of HL-LHC at a centre-of-mass energy of 14 TeV. The increase in luminosity will lead to significantly higher radiation levels. Over the expected lifetime of HL-LHC, the innermost detector regions are expected to receive a 1 MeV neutron equivalent fluence of $2.3 \cdot 10^{16} \text{ n}_{\text{eq}}/\text{cm}^2$. This fluence measures the total number of particles passing through a unit area, normalised to the displacement damage caused by 1 MeV neutrons. Using 1 MeV neutron-equivalent fluence allows different particle types and energies to be compared on a standard radiation damage scale. The total corresponding ionising dose is 12 MGy, which measures the absorbed energy per unit mass and is relevant for the degradation of electronics and scintillating materials. This dose of radiation is equivalent to 200 000 full cancer treatments, placing high demands on radiation hardness electronics and sensors. Under these harsh conditions, together with the increased data rates, the current detectors reach the limits of their original design, as they were never built to operate in the HL-LHC environment [7].

1.4 CMS

CMS is one of the four main experiments at the LHC where particles collide. It functions like a high-speed camera, sampling detector signals at the 40 MHz LHC bunch crossing frequency, while only a subset of events is recorded after trigger selection at about 100 kHz. Among the LHC experiments, CMS is the most compact, 15 meters in height and 21 meters in length, with a total weight of about 14 000 tonnes. To identify the produced particles, CMS is composed of several layers, each designed for a specific purpose, and features a powerful solenoid magnet, which is also its heaviest component, weighing around 10 800 tonnes [9].

The following sections introduce the fundamental design of the CMS detector, illustrated in Figure 1.4.1. Figure 1.4.2 shows how different particles traverse and interact with the various detector layers, depending on their charge and type.

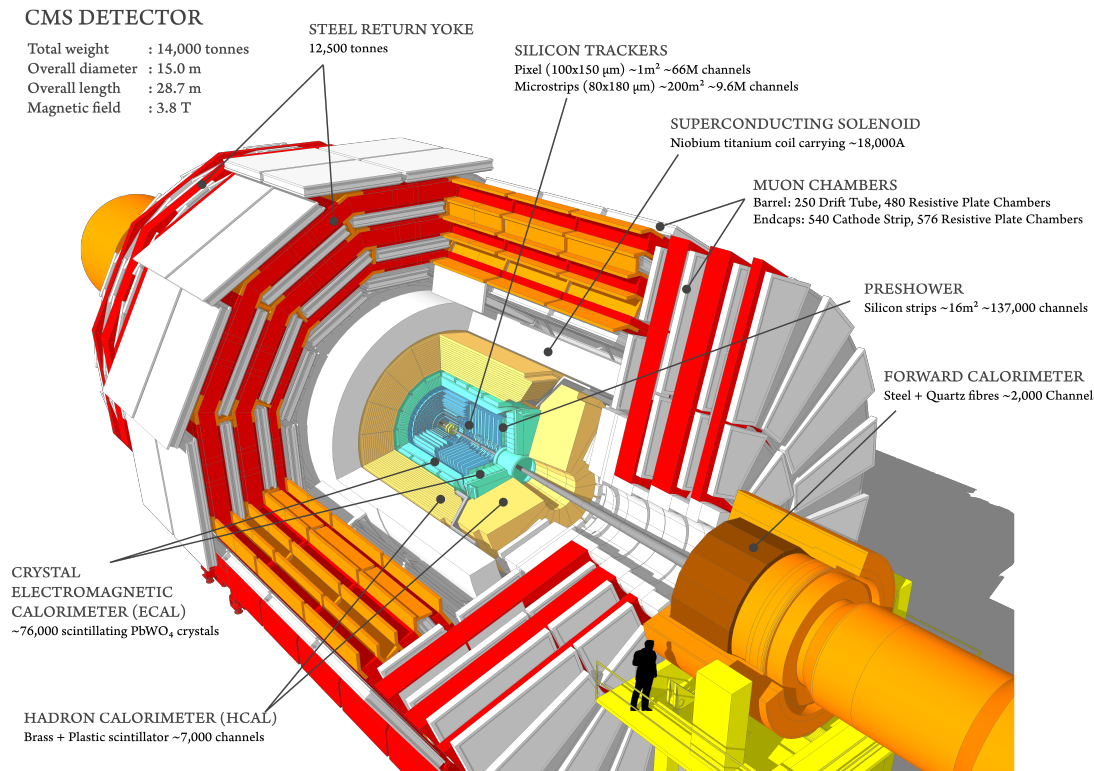


Figure 1.4.1: Design of the CMS detector. Credit: [8].

1.4.1 Magnet System

To identify particles within the detector, their trajectories must be bent as they move outward from the collision point. Charged particles curve in opposite directions depending on their charge sign, positive or negative, when passing through a magnetic field. The momentum of these particles can be determined from the curvature of their tracks, high-momentum particles follow straighter paths, while low-momentum particles exhibit stronger curvature.

Bending particles within the limited space of a compact detector requires a powerful magnet. The solenoid is therefore one of the key components of CMS, reflected in its name, *Compact Muon Solenoid*. It consists of a cylindrical coil made of superconducting material, operated at 5 Kelvin to maintain superconductivity. This allows a current of 18 164 Ampere to flow without resistance, generating a magnetic field of 3.81 Tesla, about 100 000 times stronger than Earth's magnetic field [10].

1.4.2 Tracking System

The curved trajectories of charged particles, including electrons and high-energy muons, are measured as they move through a magnetic field to determine their momentum. With silicon pixel sensors closest to the interaction point and silicon microstrip sensors surrounding them, the CMS tracker is entirely based on silicon detector technology because of its radiation-hard material properties.

When charged particles traverse the silicon layers, they generate small electronic signals that are amplified and processed by integrated readout chips before being transmitted via optical fibres for further analysis. By precisely reconstructing the sequence of hits across

the silicon layers, the trajectories of charged particles can be determined with a spatial resolution of $10\text{ }\mu\text{m}$, enabling accurate momentum measurements [11].

1.4.3 Calorimeter System

To reconstruct what happens during a collision, the energies of particles traversing the detector are measured using the Electromagnetic Calorimeter (ECAL) and the Hadron Calorimeter (HCAL).

The ECAL is the inner of the two calorimeters, located between the silicon tracker and the HCAL. It is designed as a cylindrical barrel with two endcaps. The ECAL is a homogeneous calorimeter consisting of approximately 76 000 scintillating PbWO_4 crystals, which function as both absorber and scintillator. This material was chosen because of its fast scintillation response, and its short radiation length of $X_0 = 0.89\text{ cm}$, which is the mean length into the material at which the energy of a particle is reduced by $1/e$. To limit the longitudinal shower leakage of high-energy electromagnetic showers to an acceptable level, a total thickness of 26 radiation lengths at pseudorapidity $|\eta| = 0$ is required [12]. Pseudorapidity is defined as $\eta = -\ln(\tan(\theta/2))$ and describes the polar angle θ relative to the beam axis, with $\eta = 0$ corresponding to directions perpendicular to the beam. The ECAL measures the energy of photons and electrons by converting their energy into light through the scintillating crystals. The light is proportional to the energy deposited by the electromagnetic particles. This light is then converted into electrical signals by photodetectors and sent to the readout electronics for analysis.

Surrounding the ECAL and enclosed by the superconducting solenoid is the HCAL. It shares a similar geometry to the ECAL, with a barrel section and two endcaps. Unlike the ECAL, the HCAL is designed to measure the energy of hadrons, particles composed of quarks and gluons, including both baryons, e.g., protons and neutrons, and mesons, e.g., pions and kaons. Hadrons interact primarily through the strong nuclear force and therefore traverse the ECAL with relatively little energy loss before being absorbed in the HCAL. The HCAL is a heterogeneous sampling calorimeter, built from alternating layers of dense absorber material and plastic scintillators. When hadrons interact within the absorbers, they produce secondary particles that may either interact again or deposit energy in the scintillators, generating light signals that are read out by photodetectors. This cascading process continues until most of the incident particle's energy is absorbed. A similar cascading process occurs in the ECAL, known as an electromagnetic shower. The HCAL is composed of two barrels, the inner barrel calorimeter, positioned inside the solenoid with an interaction length of 5.15λ deep at $|\eta| = 0$. The interaction length is the mean distance a hadron travels through a material before undergoing a nuclear interaction. The outer barrel calorimeter, located outside of the solenoid, is designed to measure the tails of these showers. The HCAL endcaps average about 10.5λ , sufficient to contain hadronic showers in the endcap region [13].

1.4.4 Muon System

Muons are the final particles detected directly by the CMS experiment. They are charged leptons, about 200 times heavier than electrons, with a mass of roughly $105.7\text{ MeV}/c^2$. The muon system is particularly important because one of the Higgs boson decay channels is $H \rightarrow ZZ^* \rightarrow \mu^+\mu^-\mu^+\mu^-$, where the Higgs boson decays into two Z bosons, each producing

a muon pair.

Because of the large mass of muons and their weak interaction with matter, muons pass through the ECAL and HCAL with minimal energy loss. The muon chambers are located at the outer edge of the detector, where most other particles have been absorbed, allowing muons to be measured with a clear signal. This placement also improves momentum resolution, as muon trajectories can be reconstructed over a longer distance. The momentum is determined by combining the track measured in the silicon tracker with the hits recorded in the four muon detector layers by bending the muons through the strong magnetic field [14].

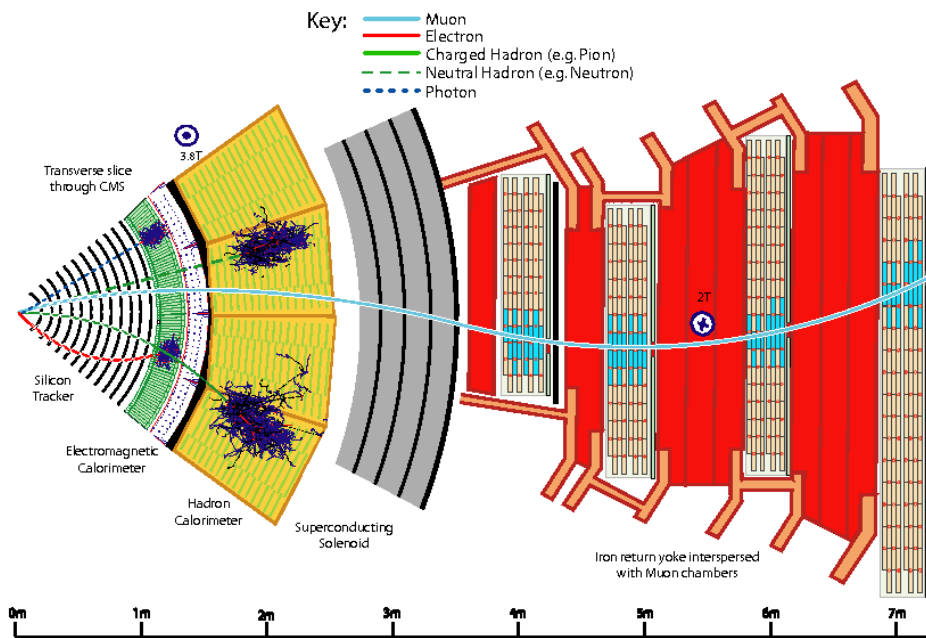


Figure 1.4.2: Different types of particles traversing the CMS detector. Electrons and charged Hadrons have a bent trajectory through the strong magnetic field because they are charged. Photons and neutrons are neutrally charged and therefore travel in a straight line. Particle showers can be seen in both the ECAL and the HCAL when particles interact with the different layers. Muons traverse all layers without being stopped. Credit: [15].

1.5 Current Limitations of CMS

With the HL-LHC, the integrated luminosity will increase by a factor of 10, and the pile-up will increase from about 60 to 140–200 interactions per bunch crossing. This causes significant challenges due to radiation damage in sub-detectors and from the management of high pile-up. To preserve efficiency, resolution, and background rejection for all physics objects used for data analysis, CMS is planning an upgrade during Long Shutdown 3. There are several upgrades to be made throughout the detector, but this thesis will focus on the calorimeter endcap upgrade to withstand the harsh radiation conditions caused by the increased fluence. Particles produced in collisions are more likely to travel along the beam axis than perpendicular to it, because they inherit the initial momentum of the colliding particles. Consequently, the endcap calorimeters, located along the axis, are exposed to more particles and accumulate more radiation damage than the barrel sections.

The Electromagnetic and Hadron Calorimeter Endcaps (CE-E and CE-H) are currently limited to an integrated luminosity of 500 fb^{-1} . The current PbWO_4 crystals for ECAL and the plastic scintillators in HCAL will both experience optical transmission loss due to radiation damage. Radiation will not affect the ability of the scintillation mechanism to produce light, but it reduces optical transparency, meaning less light reaches the photodetectors which can reduce signal strength by up to 90 %. An unacceptable loss of physics performance of the detector will occur if the current endcap calorimeter accumulates more than 500 fb^{-1} . [16]

To study the choice of base material for the upgraded calorimeter endcaps and to understand the radiation-harsh conditions the detector will face in the HL-LHC environment, simulations have been performed with a Monte Carlo simulation using FLUKA. Simulations were mostly based on proton-proton collisions, as the primary source of radiation comes from the particles produced from them.

Figure 1.5.1 presents a FLUKA simulation of the accumulated 1 MeV neutron-equivalent fluence on one side of the inner sector of the CMS detector, including the silicon tracker as well as the endcap and barrel calorimeters. The simulation indicates that the highest fluence, reaching approximately $1 \cdot 10^{16} \text{ n}_{\text{eq}}/\text{cm}^2$, occurs at the closest region of the CE-E to the collision point, corresponding to a dose of 2 MGy. To maintain detector performance under these extreme radiation levels and the expected integrated luminosity of 3000 fb^{-1} over the HL-LHC lifetime, the endcaps will be replaced with the High Granularity Calorimeter [7].

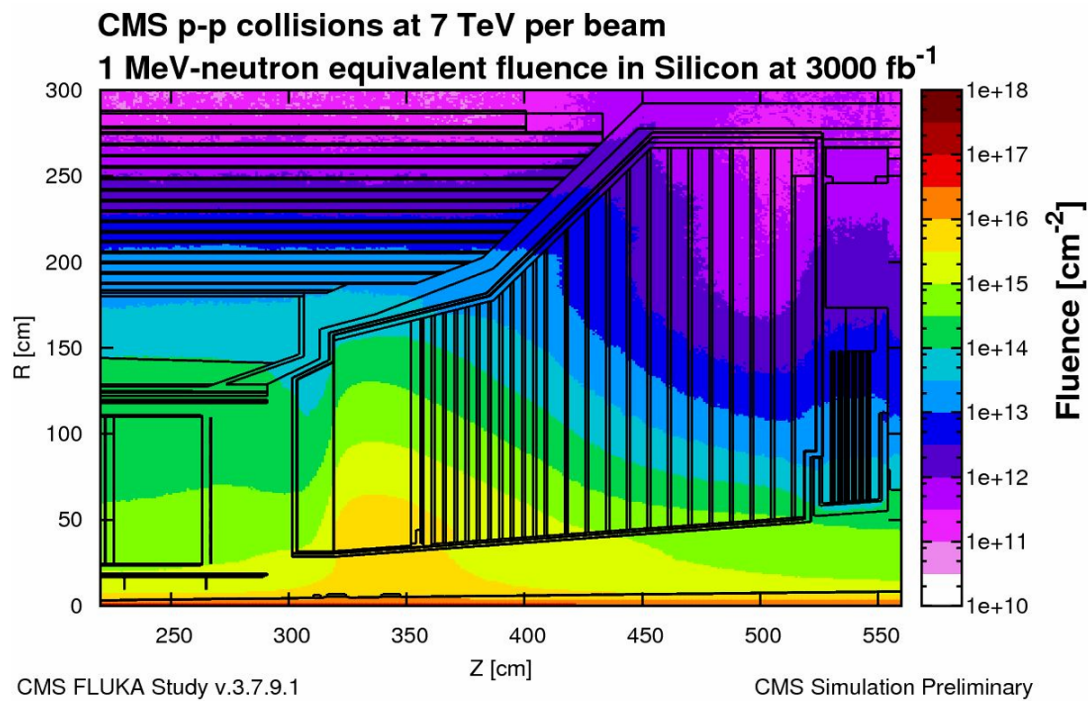
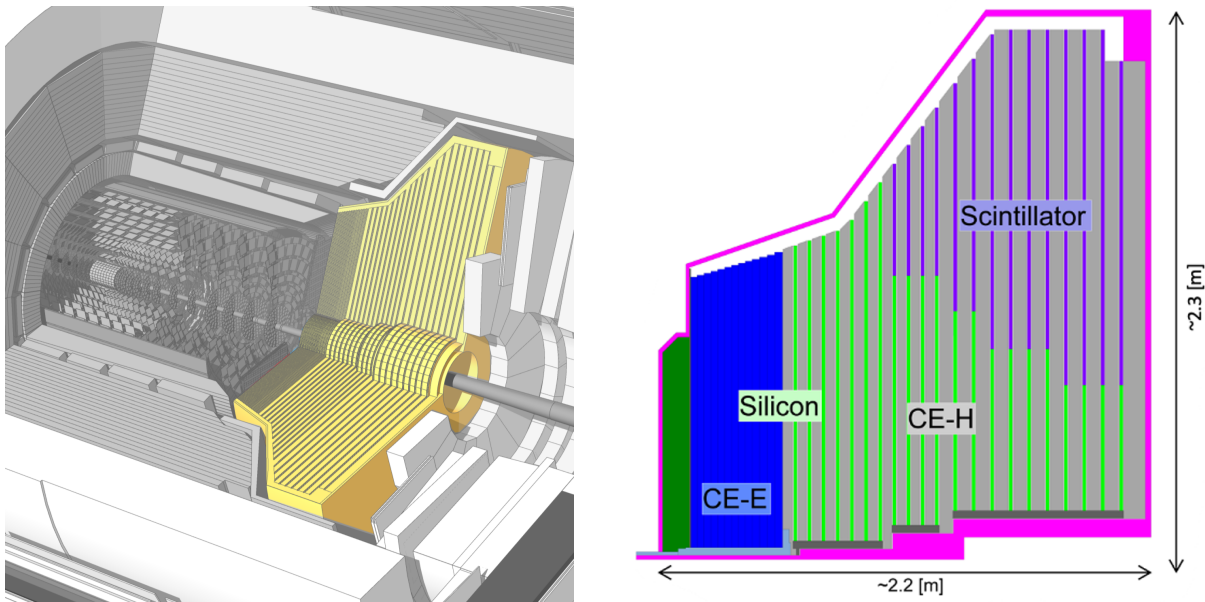


Figure 1.5.1: Accumulated fluence of 1 MeV equivalent neutrons using FLUKA simulation for integrated luminosity 3000 fb^{-1} . R is the radial direction, and Z is the longitudinal direction of the detector. Credit: [7].



(a) HGCAL highlighted in yellow as the replacement for the previous endcap calorimeters. Credit: [17].

(b) Cross-section of the upper half of the upgraded endcap calorimeter. CE-E is the Electromagnetic Endcap Calorimeter, and CE-H is the Hadronic Endcap Calorimeter. Credit: [18].

Figure 1.6.1: Overview of the HGCAL upgrade.

1.6 High Granularity Calorimeter

HGCAL is based on silicon sensors in the high radiation areas, covering the CE-E and part of the CE-H, together with plastic-scintillator tiles in the lower radiation areas, reaching up to an accumulated fluence of $8 \cdot 10^{13} \text{ n}_{\text{eq}}/\text{cm}^2$ with a dose of 3 kGy. A cross-section of the upper half of HGCAL can be shown in Figure 1.6.1b. Silicon sensors were chosen for the high-radiation regions because they maintain sufficient charge collection even after receiving 50 % more fluence than the HL-LHC lifetime expectation, i.e. $1.5 \cdot 10^{16} \text{ n}_{\text{eq}}/\text{cm}^2$ [7]. To mitigate the radiation-induced effects, such as increased leakage current and reduced charge collection, the HGCAL will operate at approximately -35°C .

HGCAL will consist of 47 active layers with approximately 26 000 individual modules, resulting in a total of 6 M readout channels, covering the pseudo-rapidity of $|1.5| < \eta < |3|$. In total, about 620 m^2 of silicon sensors will be used in the high-radiation regions of the CE-E and CE-H, complemented by about 400 m^2 of plastic scintillators in the outer, lower-radiation regions. This makes HGCAL the largest silicon-based detector system in high-energy physics. The design follows the principle of a sampling calorimeter, similar to the current HCAL, absorber layers initiate electromagnetic or hadronic showers when traversed by particles, while the active layers measure the resulting energy deposition.

The silicon sensors are produced by Hamamatsu Photonics K.K. on 8-inch circular silicon wafers and cut into hexagonal shapes. The hexagonal geometry was selected because it allows the sensors to cover a surface efficiently without leaving gaps, improving wafer usage and minimising inactive regions. The HGCAL silicon sensors are produced with three different active thicknesses, 300 μm and 200 μm produced with the Float Zone (FZ) process, and 120 μm produced with the Epitaxial (EPI) process on top of a handling wafer

of $180\text{ }\mu\text{m}$ to prevent breakage [19].

In the FZ process, silicon crystals are grown by melting a small zone of a silicon rod using radio-frequency induction, yielding ultra-pure silicon with high resistivity. In contrast, the EPI process involves growing a thin, high-quality silicon layer on top of a substrate, enabling precise control of the active layer thickness and doping during growth.

The different thicknesses of the silicon sensors are distributed across various regions of the HGCAL due to their differing electrical characterisation properties. $120\text{ }\mu\text{m}$ have lower leakage current, lower depletion voltage, and higher charge collection efficiency and are therefore more suitable for high-radiation regions compared to FZ sensors.

Each module, corresponding to one 8-inch silicon sensor, contains several hundred individual hexagonal cells, each read out separately. Two types of sensors are used, Low Density (LD) and High Density (HD). The distinction between them lies in the number and size of the cells. LD sensors consist of 192 cells, each with an area of 1.18 cm^2 , whereas HD sensors contain 432 smaller cells with an area of 0.52 cm^2 . The placement of LD and HD sensors depends on the expected particle distribution in a given region. In areas closer to the collision point, where the particle density is the highest, HD sensors are placed for finer granularity. Both sensor modules are displayed in Figure 1.6.2, where the 8-inch silicon wafer is cut into a hexagonal shape. The remaining space on the wafer, referred to as half-moons, contains test structures with the same properties as the individual cells in the main sensor part. The measurements in this thesis utilise squared silicon sensors diced from half-moons with a width of 0.5 cm to study the radiation hardness and annealing effects of silicon sensors. [7, 20]

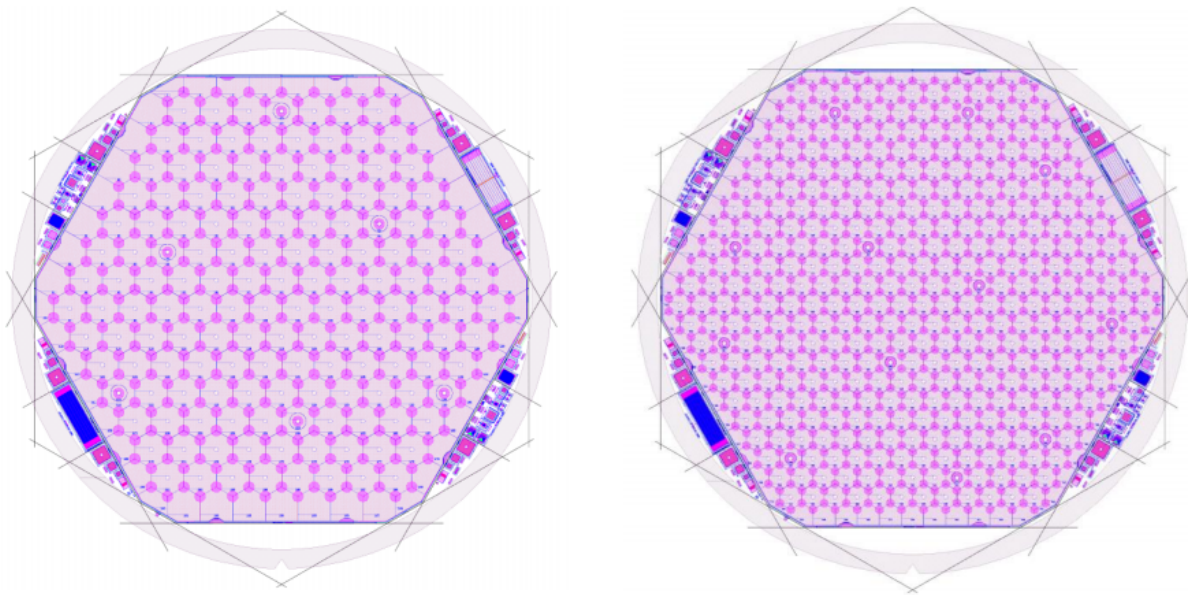


Figure 1.6.2: Structure of 8-inch Low Density and High Density silicon sensors together with the test structures outside of the hexagonal cut. Credit: [20].

1.7 Thesis Objective, Contributions & Outline

This thesis studies the radiation hardness properties and annealing effects of silicon diodes for the CMS endcap calorimeter upgrade, HGCAL. A previous study has examined the performance of silicon diodes exposed to fluences corresponding to the end of the HL-LHC, referred to as the High Fluence (HF) campaign [21]. The goal of this thesis is to investigate a more realistic scenario that mimics the HL-LHC timeline. Run 4 will deliver one quarter of the end-of-life fluence, followed by Long Shutdown 4, during which the silicon sensors are planned to undergo beneficial annealing. The first round of irradiation and beneficial annealing is referred to as the Double Irradiation (DI) campaign. Run 5 will deliver the remaining three quarters of the fluence, reaching levels similar to those of the HF campaign. After the second round of irradiation, the diodes undergo both beneficial and reverse annealing, referred to as the Double Irradiation Second Round (DI SR) campaign. Comparisons are made between the HF and DI SR campaigns for the current related damage rate α , the saturation voltage, and the charge collection efficiency. The irradiations used to mimic the HL-LHC conditions are performed in the *Training, Research, Isotopes, General Atomics* (TRIGA) Nuclear reactor at the Jožef Stefan Institute, Ljubljana, Slovenia. To accelerate the study, annealing is performed at three temperatures, 20.5 °C, 40 °C, and 60 °C, allowing extraction of the annealing constants at lower temperatures by interpolation. During Long Shutdown 4, the planned temperature for HGCAL is approximately 0 °C.

In addition to the measurements, the IV, CV, and TCT measurement software has been improved for greater efficiency, allowing more data to be collected for the comparison analyses between the HF and DI SR campaigns. A new Python-based GUI analysis software was also developed to provide easy access to the measured data, automatically generate databases, and produce all plots and analyses used in this thesis.

The remainder of this thesis is structured as follows. Chapter 2 introduces the basic semiconductor theory required to understand the working principles of silicon sensors. This chapter covers material properties in §2.1, intrinsic and extrinsic semiconductors in §2.2, and §2.3. §2.4 covers the key electrical characteristics, such as leakage current, depletion voltage, which will later be referred to as saturation voltage for irradiated diodes, and charge collection.

Chapter 3 presents radiation damage and annealing mechanisms, explaining how these processes affect the bulk and electrical properties of the sensors.

Chapter 4 describes the methods used in this thesis. §4.1 presents the $0.5 \cdot 0.5 \text{ cm}^2$ test silicon sensors diced from an 8-inch silicon wafer, only these are referred to as diodes throughout this thesis. §4.2 provides an overview of the irradiation campaigns. §4.3.1 presents the IV and CV probe station setup used before mounting the diodes on Printed Circuit Boards (PCBs), which is required to identify outlier diodes with the same fluence and thickness before measurements in the IV, CV, and TCT setup described in §4.3.2. §4.5 describes the annealing process of the diodes done in the laboratory. More detailed descriptions of the software upgrades and development are presented in §4.3.3 and §4.4.

Finally, Chapters 5 and 6 present and discuss the electrical characterisation comparisons between the HF and DI SR campaigns.

CHAPTER 2

SILICON SENSORS

Silicon sensors are widely used in High Energy Physics (HEP) detectors due to their combination of radiation hardness, fine segmentation, and suitable electrical properties in the high-radiation environment. These characteristics allow accurate particle detection and particle-flow reconstruction , a technique that combines information from all subdetectors to identify and measure individual particles in an event [15].

The performance of silicon sensors depends on the behaviour of the charge carriers, electrons and holes, which is determined by the electronic structure of the material. Electrons can be bound to atoms in the valence band or unbound in the conduction band, where they contribute to electrical conduction. Holes represent the absence of a bound electron in the valence band and behave as positively charged carriers. Materials are generally classified as conductors, insulators, or semiconductors according to their electrical conductivity.

This chapter provides a general introduction to semiconductor physics, giving the essential understanding for the rest of the thesis. For more detailed information, the following theory is based mainly on *Particle Detectors Fundamentals and Applications* and *Evolution of Silicon Sensor Technology in Particle Physics* [22, 23]. It first introduces the material properties in §2.1, namely the energy band structures of different materials, and then focuses on semiconductor properties, such as bonding, intrinsic carrier concentration, and carrier transport. These fundamental concepts provide the basis for understanding the behaviour of a PN-junction, which is presented in §2.3.2. PN-junctions form the core of silicon sensors, and their electrical characteristics, including the effects of induced current, electric field, depletion zones, and forward and reverse bias.

The final section, §2.4, focuses on the practical characteristics of silicon sensors, including leakage current, capacitance, depletion voltage, and charge collection, and links fundamental semiconductor physics to the experimental performance of silicon sensors.

2.1 Material Properties

This section introduces the material properties of semiconductors, including the energy band structures of different solids in §2.1.1 and the bond model of a pure silicon semiconductor presented in §2.1.2.

2.1.1 Energy Band

In a solid-state lattice, the periodic potential of the atoms allows only certain energy levels, forming closely spaced, discrete energy levels, known as energy bands. Their distribution depends on the composition of the material, which determines its electrical properties. Electrons in the valence band are bound to atoms, while the conduction band

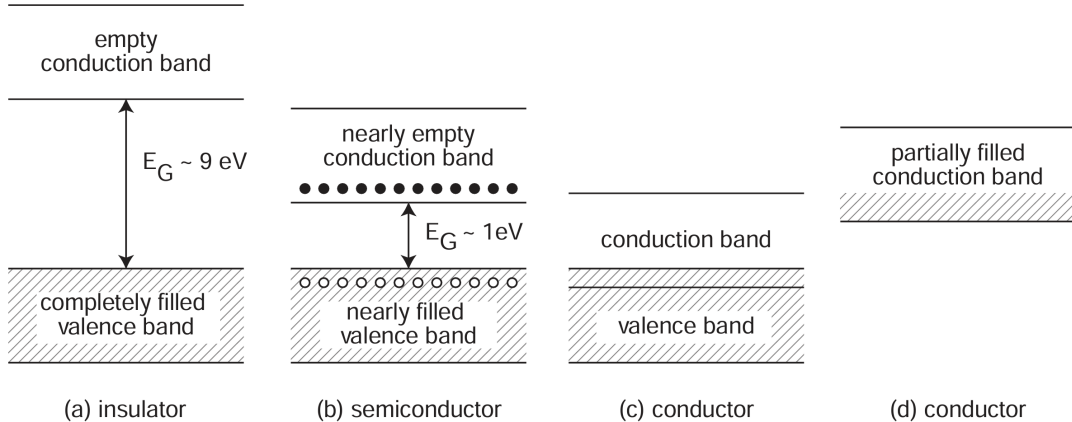


Figure 2.1.1: Overview of the energy-band structures for insulators, semiconductors, and conductors where E_G is the energy band gap of the material. Credit: [22].

provides states where electrons can move within the lattice, contributing to current. Electrical conduction depends on the occupancy of these bands. If the valence band is filled and the conduction band is empty, electrons cannot contribute to electrical conduction, and no current can flow. The energy band structures of insulators, semiconductors, and conductors are shown in Figure 2.1.1 to illustrate the difference in electrical conductivity.

In insulators, the electrons in the valence band are strongly bound to their atoms and cannot easily move to neighbouring atoms. According to the Pauli exclusion principle, each quantum state can hold at most one electron, or two with opposite spins in an orbital. In an insulator, all quantum states in the valence band are fully occupied. The conduction band in an insulator is empty. Because of the strong interatomic bonds, there is a large energy band gap E_G , between the valence and conduction bands, typically around 9 eV [22]. The large band gap prevents electrons from moving from the valence band to the conduction band by thermal excitations at room temperature and atmospheric pressure, resulting in a material that does not conduct electricity.

In conductors, the conduction band is either partially filled or overlaps with the valence band, leaving no significant energy gap. This allows electrons to move within the lattice under an external electric field. Therefore, transitions between energy levels within the bands require minimal energy, enabling efficient electrical conduction at room temperature.

In semiconductors, the bonds between neighbouring atoms are weaker than in insulators, which leads to a smaller energy band gap. For silicon, E_G is 1.12 eV at room temperature. This band gap can be exceeded by thermal excitation or by an external electric field if the absorbed energy is $E \geq E_G$, which lifts electrons from the valence band to the conduction band, leaving behind holes in the valence band. Both the free electrons in the conduction band and the corresponding holes in the valence band act as charge carriers, with electrons carrying negative charge and holes carrying positive charge. The size of E_G depends on the lattice spacing and can vary with temperature and pressure, which consequently affects the conductivity of the material [22].

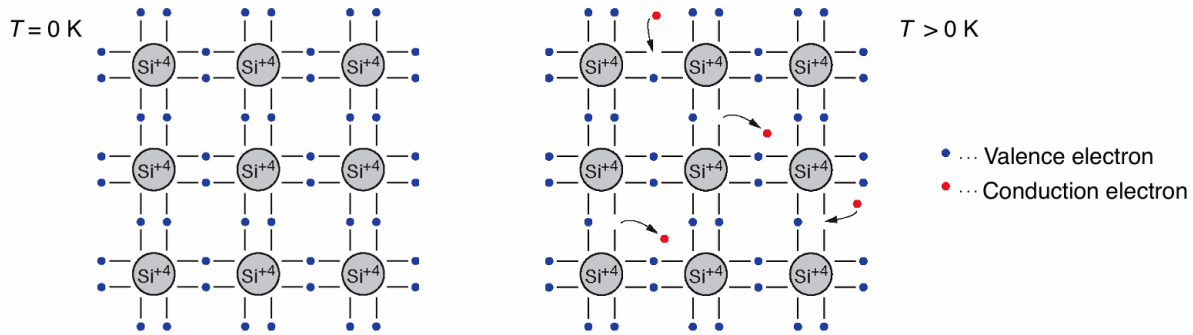


Figure 2.1.2: Bond model of a pure silicon semiconductor. At low temperatures (left), electrons remain bound to the atoms. Thermal vibrations break some bonds (right), enabling electron conduction. Credit: [24].

2.1.2 Bond Model of Semiconductors

Semiconductors can be either pure elements or compounds made from elements of different groups in the periodic table. In silicon, each atom forms four covalent bonds with its nearest neighbours, sharing one electron per bond to complete its outer shell.

Theoretically, at absolute zero and in the absence of impurities, all electrons remain bound within the covalent bonds, and the material behaves as an insulator. As the temperature rises, thermal vibrations can break some of these bonds, lifting electrons from the valence band to the conduction band. These free electrons enable electrical conduction. Holes can move through the lattice as neighbouring electrons fill the empty sites, giving rise to hole conduction. This process, along with the bond structure of intrinsic silicon, is illustrated in Figure 2.1.2.

2.2 Intrinsic Semiconductors

When no external impurities are introduced into the crystal lattice, the semiconductor is referred to as intrinsic. As mentioned previously, electrons and holes can be treated as free particles within their respective bands, differing only by their effective masses, m_e^* for electrons and m_h^* for holes.

§2.2.1 presents briefly, in general, the carrier concentrations, density of states, and occupation probabilities for an intrinsic semiconductor, with their relationships illustrated in Figure 2.2.1. §2.2.2 describes charge carrier motion and scattering within the lattice. More detailed derivations and explanations for §2.2 and §2.3 can be found in [22, 23].

2.2.1 Carrier Concentration, Fermi Level, Density of States

In an intrinsic semiconductor, the electron concentration, n , in the conduction band equals the hole concentration, p , in the valence band, so that $n_i = n = p$, where n_i is the intrinsic carrier concentration. This equality reflects the global charge neutrality in thermal equilibrium, resulting in no net electrical charge within the crystal. Charge neutrality is broken when external carriers are injected, e.g., by applying a bias voltage, generating electron-hole pairs with light, or introducing a doping imbalance.

Carrier concentrations are determined by the density of states in each band and the

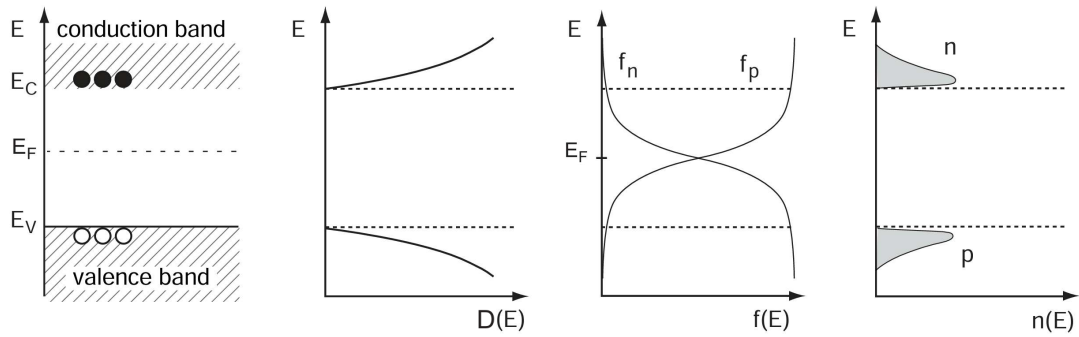


Figure 2.2.1: Schematic overview of the energy band model for intrinsic silicon, showing (from left to right) the band diagram, density of states, occupation probabilities, and charge carrier concentrations in the conduction and valence bands. Credit: [22].

probability that a state is occupied at energy E . In thermal equilibrium at temperature T , the electron occupation probability is given by the Fermi-Dirac distribution,

$$f_n(E, T) = \frac{1}{e^{(E-E_F)/k_B T} + 1}, \quad (2.2.1)$$

where E_F is the Fermi level and k_B is the Boltzmann constant. By definition, the Fermi level corresponds to the energy at which a state has a 50 % probability of being occupied. For an intrinsic semiconductor, the Fermi level lies near the middle of the bandgap.

The concentrations of electrons and holes in an intrinsic semiconductor are,

$$n = N_C e^{-\frac{E_C - E_F}{k_B T}}, \quad N_C = 2 \left(\frac{2\pi m_e^* k_B T}{h^2} \right)^{3/2}, \quad (2.2.2)$$

$$p = N_V e^{-\frac{E_F - E_V}{k_B T}}, \quad N_V = 2 \left(\frac{2\pi m_h^* k_B T}{h^2} \right)^{3/2}, \quad (2.2.3)$$

where N_C and N_V represent the effective density of states in the conduction and valence bands. As the charge neutrality holds, dependencies on the Fermi level can be eliminated by multiplying the electron and hole densities, giving the mass action law

$$n_i^2 = n \cdot p = N_C N_V e^{-E_G/k_B T}, \quad (2.2.4)$$

where $E_G = E_C - E_V$ is the bandgap energy.

2.2.2 Mobility, Drift Velocity and Scattering

When an electric field, E , is applied to a semiconductor, free charge carriers, electrons and holes, experience a force that causes them to drift within the lattice. Their motion is interrupted repeatedly by scattering events. Scattering arises from crystal defects that may form during crystal growth or as a consequence of radiation damage, from impurity atoms introduced by doping, or from phonons generated by thermal lattice vibrations. These events limit the carrier motion and lead to an average drift velocity that is proportional to the applied electric field:

$$v_D = \mu E, \quad (2.2.5)$$

where μ is the mobility of the carrier, a quantity that determines how easily the free charge carriers can move through the crystal lattice under an applied electric field. Electrons and holes generally have different mobilities, denoted respectively as μ_e and μ_h .

At the microscopic level, the electron and hole mobility can be expressed as

$$\mu_{e,h} = \frac{e\tau_s}{m_{e,h}^*}, \quad (2.2.6)$$

where e is the electron charge, and τ_s is the time between scattering events. A reduction in τ_s due to increased scattering leads to a decrease in charge carrier mobility within the crystal lattice. The mobility for electrons and holes is $\mu_e = 1350 \text{ cm}^2/\text{Vs}$ and $\mu_h = 450 \text{ cm}^2/\text{Vs}$ [23].

2.3 Extrinsic Semiconductors

This section introduces extrinsic semiconductors, explaining how the addition of impurities modifies the electrical properties. In §2.3.1, the effect of donor and acceptor atoms on charge carrier concentrations, energy bands, and electronic properties is presented. The formation of a PN-junction is described in §2.3.2, along with its behaviour under external voltages in §2.3.3.

2.3.1 Doping

The electrical conductivity of a semiconductor can be modified by introducing impurity atoms into the crystal lattice, known as doping. A doped semiconductor is referred to as extrinsic, in contrast to an intrinsic semiconductor. Doping increases the number of free charge carriers, electrons or holes, thereby increasing the electron or hole conduction in the material.

Silicon is a type IV material, meaning each atom has four valence electrons. It can be doped with either type III or type V materials to modify its free charge carrier concentration. To produce a semiconductor that has an excess of electrons as majority charge carriers, it is possible to add type V material, e.g., phosphorus, which is a donor impurity. The excess of electrons increases the electron charge carrier concentration, making it n-type silicon. The same way for p-type silicon, where it is possible to add type III material, acceptor impurities, to get an excess of holes as the major charge carriers.

Doping increases the concentration of one type of charge carrier, but the semiconductor remains electrically neutral because the impurity atoms are neutrally charged. The mass action law, $n_i^2 = n \cdot p$, introduced in section §2.2.1 for intrinsic semiconductors still holds for extrinsic semiconductors. As the number of majority carriers increases, the minority carrier concentration decreases.

When impurities are uniformly distributed, the semiconductor has a net charge density of zero within any volume, known as space-charge neutrality. If all donors and acceptors are fully ionised, i.e., that all dopant atoms have donated or accepted their extra electron or hole to the conduction or valence band, respectively, the charge density of an extrinsic semiconductor can be expressed as

$$\rho = e(n - p + N_D - N_A) = 0 \quad \Rightarrow \quad n - p = N_D - N_A, \quad (2.3.1)$$

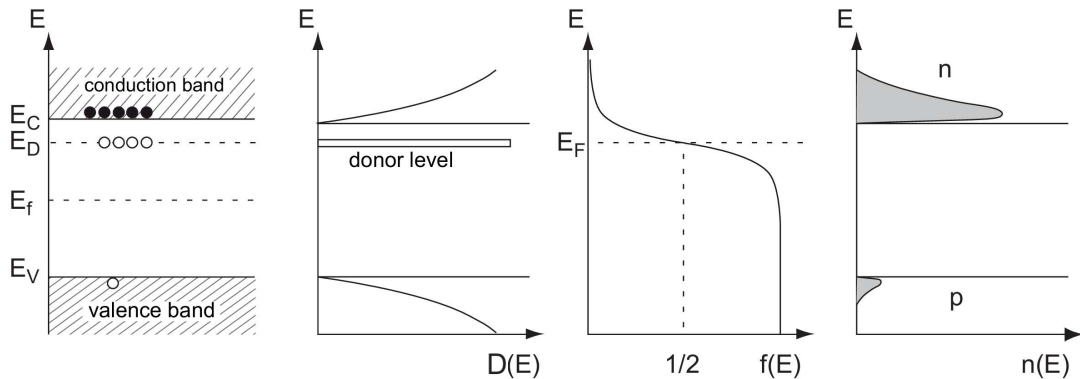


Figure 2.3.1: Schematic overview of the energy band model for an extrinsic n-doped silicon, showing (from left to right) the band diagram and the density of states with the additional donor level, the occupation probabilities for electrons in the presence of this level, and finally the charge carrier densities in the conduction and valence bands. In p-doped silicon, the acceptor level, E_A , appears close to the valence band instead of the donor level, E_D . The Fermi level, E_F , moves below the intrinsic Fermi level, E_f , and the hole density exceeds the electron density. Credit: [22].

where N_D and N_A are the donor and acceptor concentrations. Combining Equation (2.3.1) with Equation (2.2.4) derives to the majority charge densities,

$$n \approx |N_D - N_A| \approx N_D, \quad \text{n-type } (N_D \gg n_i \gg N_A) \quad (2.3.2)$$

$$p \approx |N_A - N_D| \approx N_A, \quad \text{p-type } (N_A \gg n_i \gg N_D) \quad (2.3.3)$$

where n_n and p_p denote the electron and hole densities in n-type and p-type semiconductors, respectively.

Doping not only changes the concentration of charge carriers but also the energy band structure of the semiconductor. In n-type semiconductors, donor atoms introduce energy levels slightly below the conduction band, allowing electrons to be easily thermally excited into the conduction band. This shifts the Fermi level upward, closer to the conduction band.

Similar to the illustration of the energy band model, density of states, occupation probabilities of electrons and holes, and charge carrier densities for an intrinsic semiconductor, an illustration of an n-type extrinsic semiconductor, shown in Figure 2.3.1, displays the shift between the extrinsic Fermi level E_F and the intrinsic Fermi level E_f . For a p-type extrinsic semiconductor, the properties are reversed. The extrinsic Fermi level lies closer to the valence band, the hole concentration p , is larger than the electron concentration n , and the probability of hole occupation in higher energy states becomes greater compared to the n-type semiconductor [22].

2.3.2 PN-Junction

When a p-type and an n-type semiconductor are brought into contact, a PN-junction is formed. At the junction, the majority carriers, holes in the p-type region and electrons in the n-type region, begin to diffuse across the boundary due to the strong concentration gradients, as illustrated in Figure 2.3.2. In the energy band model, the Fermi levels of the two regions differ initially due to their distinct doping concentrations. Once contact is

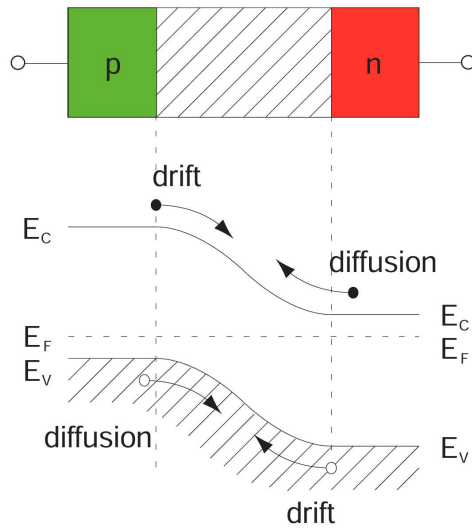


Figure 2.3.2: Drift and diffusion of holes and electrons at the junction between p-type and n-type semiconductors. Credit: [22].

established, charge diffusion continues until thermal equilibrium is reached, aligning the Fermi level across the entire junction.

As the electrons and holes diffuse across the junction, they recombine near the boundary. This leaves behind immobile ionised donor and acceptor atoms, forming a region depleted of free charge carriers. This region is known as the depletion region or space charge region. While free charge carriers are absent in this zone, the fixed charged ions give rise to a non-zero space charge density $\rho(x)$. The p-type side becomes negatively charged, and the n-type side positively charged. This charge separation produces an internal electric field that points from the n-type toward the p-type region, forming a drift current I_{drift} that counteracts the diffusion current I_{diff} .

The balance between drift and diffusion reaches a steady state, known as thermal equilibrium, in which no net current flows across the junction. The potential difference created by this internal field, referred to as the built-in voltage V_{bi} , causes the energy bands to bend near the junction while the Fermi level remains constant. In this equilibrium, the space-charge region only depends on the doping concentration of the p-type and n-type regions:

$$\rho(x) = \begin{cases} -eN_A, & \text{if } -x_p < x < 0, \\ +eN_D, & \text{if } 0 < x < x_n, \end{cases} \quad (2.3.4)$$

where x_p and x_n are the depletion widths in the p-type and n-type regions, respectively.

Because charge neutrality must be preserved, the depletion regions extend further into the more weakly doped side of the junction, giving the relation

$$N_A \gg N_D \Rightarrow x_p \ll x_n. \quad (2.3.5)$$

The built-in voltage V_{bi} can be expressed in terms of the carrier concentrations as the potential difference between the p-type and n-type sides outside the space charge region:

$$V_{bi} = \phi_p - \phi_n = \frac{kT}{e} \ln \left(\frac{N_A N_D}{n_i^2} \right), \quad (2.3.6)$$

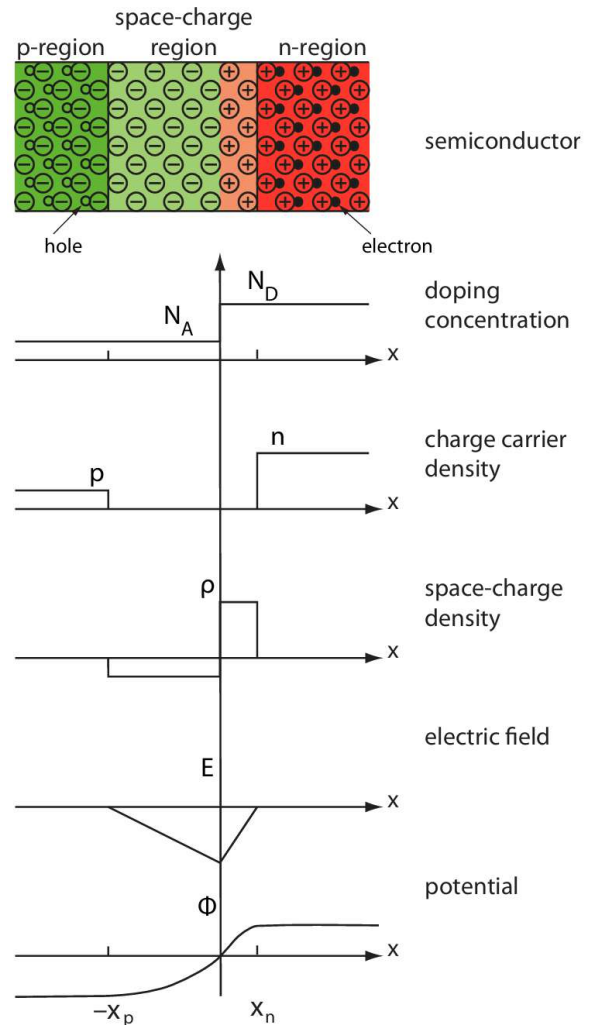


Figure 2.3.3: Schematic overview of a PN-junction at thermal equilibrium. The upper section shows the spatial distribution of ionised acceptor (−) and donor (+) atoms forming the depletion region. The diagrams from top to bottom show the doping concentrations N_A and N_D , carrier densities p and n , space-charge density $\rho(x)$, electric field $E(x)$, and electrostatic potential $\phi(x)$. The built-in electric field points from the n-side to the p-side, resulting in a potential difference V_{bi} across the depletion region. Credit: [22].

where $\phi_p = \phi(-x_p)$ and $\phi_n = \phi(x_n)$ are the electrostatic potentials at the boundaries of the depletion region.

Assuming that the depletion extends primarily into the more lightly doped side, $x_p \ll x_n$, the depletion width d can be approximated by

$$d \approx x_n \approx \sqrt{\frac{2\epsilon\epsilon_0}{e} \frac{1}{N_D} V_{bi}}, \quad (2.3.7)$$

where ϵ and ϵ_0 are the vacuum and relative permittivity, respectively.

The relation between doping concentrations, charge carrier densities, space-charge distribution, electric field, and potential across a PN-junction is illustrated in Figure 2.3.3 [22].

2.3.3 PN-Junction under External Voltage

Applying an external voltage across the n- and p-sides of a junction changes the width of the depletion region depending on both the magnitude and polarity of the applied bias. This drives the system out of thermal equilibrium, and consequently, the mass action law, Equation (2.2.4), is modified such that $np > n_i^2$ or $np < n_i^2$, depending on the polarity. As a result, the Fermi level varies across the junction, following the changes of the electrostatic potential.

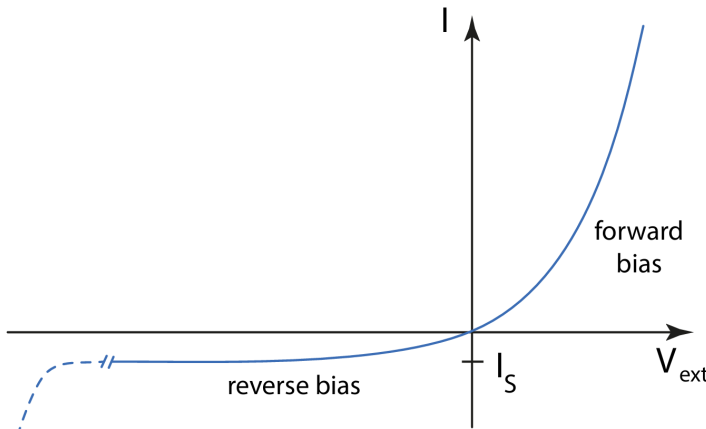


Figure 2.3.4: Current-voltage characteristics of an ideal PN-diode according to Equation (2.3.8) under forward and reverse bias. The dashed line indicates a breakdown at high reverse bias voltages, which is not described in Equation (2.3.8). Credit: [22].

There are two configurations of external bias, forward bias and reverse bias. When the applied voltage V_{ext} is positive on the p-side relative to the n-side, $V_{ext} > 0$, the junction is forward biased. In this case, the electrostatic potential difference $V_{bi} - V_{ext}$ across the depletion region is reduced, leading to a decrease in drift current relative to diffusion current. The depletion region narrows, and band bending weakens.

Under reverse bias, V_{ext} acts in the same direction as V_{bi} , which increases the electrostatic potential difference compared to the equilibrium. As a result, the diffusion current decreases, the energy band bending increases, and the depletion region widens [22].

The forward bias allows the majority carriers to more easily overcome the potential barrier, leading to an exponential increase in current, and can be described as

$$I = I_S(e^{eV_{ext}/kT} - 1), \quad (2.3.8)$$

where I_S is the reverse saturation current and kT is the thermal energy. In reverse bias, the current remains small and approximately constant until the applied external voltage reaches a critical threshold, at which point avalanche breakdown occurs. The strong electric field beyond the breakdown voltage in the depletion region can accelerate carriers to energies sufficient to generate additional electron-hole pairs, producing an uncontrolled high current. This effect is shown in Figure 2.3.4.

To calculate the depletion width of a PN-junction under an applied voltage, the built-in potential V_{bi} is replaced by $V_{bi} - V_{ext}$ in Equation (2.3.7),

$$d_{n,p} \approx x_{n,p} \approx \sqrt{\frac{2\epsilon\epsilon_0}{e} \frac{1}{N_D} (V_{bi} - V_{ext})}. \quad (2.3.9)$$

where V_{ext} is negative in reverse bias and positive in forward bias.

2.4 Silicon Sensor Characteristics

Silicon sensors are typically operated under reverse bias in particle physics, with a positive potential applied to the n-doped side. This maximises the width of the depletion region,

which serves as the active volume for particle detection. When a charged particle passes through the sensor, it deposits energy, generating electron–hole pairs. These charge carriers are collected and measured as a signal. If the sensors are not fully depleted, many of these carriers would recombine before being collected, reducing the detectable signal. Understanding the depletion voltage is therefore essential to ensure complete signal retrieval.

Connecting the theoretical concepts discussed in previous chapters with practical silicon sensors used in HEP, particularly in the CMS experiment, the following sections present key parameters and characteristics of silicon sensors operated under reverse bias. The leakage current follows the same behaviour described in §2.3.3. Additional characteristics include capacitance and depletion voltage, effective doping concentration, and charge collection properties.

2.4.1 Leakage Current

Silicon sensors produce a small current under reverse bias, known as the leakage current. The current arises primarily from the thermal generation of electron–hole pairs within the depletion region. Under an applied reverse voltage, these carriers are swept across the space-charge region by the internal electric field, producing a measurable current even in the absence of external excitation. The magnitude of the leakage current is strongly influenced by temperature, impurities, and defects in the crystal lattice, which act as generation and recombination centres within the band gap. Radiation damage can further enhance these effects by introducing additional defect states, increasing the rate of thermally generated carriers.

There are typically two contributions to the leakage current, the surface contribution, which originates mainly from the fabrication and the handling of the detector, and the volume contribution from the bulk structure, impurities, and radiation-induced defects. The volume current contribution is proportional to the depletion width, $d \propto \sqrt{V_{ext}}$, meaning that as the reverse bias increases, the depletion region widens, and a larger volume of the bulk contributes to thermally generated carriers, increasing the leakage current. In contrast, the surface current contribution increases linearly with the applied voltage [22, 23].

2.4.2 Capacitance and Depletion Voltage

Due to the depletion region, which is free of charge carriers, the capacitance can be calculated by treating the sensor as a parallel-plate capacitor with silicon as the dielectric medium. It decreases proportionally to $1/\sqrt{V_{bias}}$ until the sensor reaches full depletion width, thereafter it remains constant. The capacitance can be expressed as

$$C = \begin{cases} A\sqrt{\frac{\varepsilon_0\varepsilon_{Si}}{2\rho\mu V_{bias}}}, & \text{if } V_{bias} \leq V_{dep}, \\ A\frac{\varepsilon_0\varepsilon_{Si}}{D}, & \text{if } V_{bias} > V_{dep}, \end{cases} \quad (2.4.1)$$

where V_{dep} is the depletion voltage required to deplete the sensor to its full depletion width D , A the active sensor area, ε_{Si} and ε_0 the permittivity of silicon and vacuum, μ the charge carrier mobility, and ρ the material resistivity.

It is common to represent experimental data as $1/C^2$ rather than C as a function of V_{bias} , as the inverse capacitance squared shows a linear dependence on the applied voltage. The

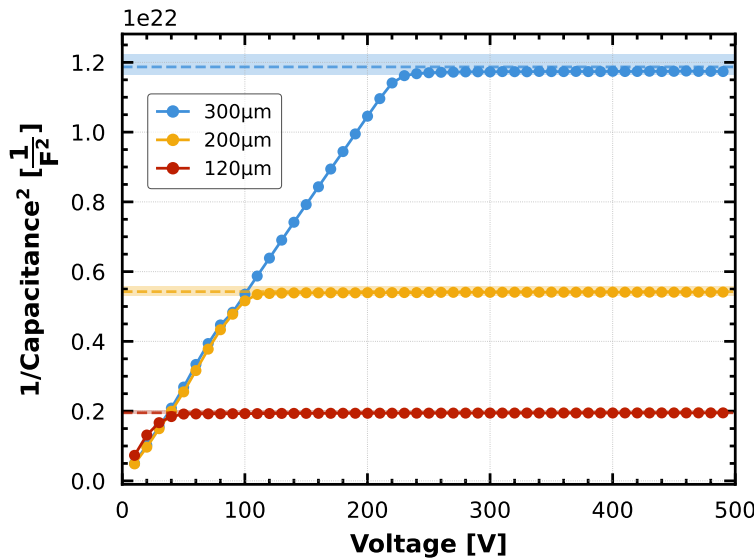


Figure 2.4.1: Inverse squared capacitance as a function of reverse voltage bias for three unirradiated diodes with thicknesses 300 μm in blue, 200 μm in yellow, and 120 μm in red. The dashed line represents the assumed end capacitance, obtained as the mean of the plateau values across all campaigns.

depletion voltage can be determined by identifying the voltage at which the capacitance becomes constant, i.e., when the sensor has reached its full depletion width. The inverse capacitance squared as a function of the reverse voltage bias for unirradiated sensors with thicknesses 300 μm , 200 μm , and 120 μm is shown in Figure 2.4.1.

2.4.3 Effective Doping Concentration

The effective doping concentration N_{eff} describes the net amount of active impurity atoms, such as donors and acceptors. If the donor and acceptor concentrations are known, N_{eff} can be determined by

$$N_{\text{eff}} = N_A - N_D. \quad (2.4.2)$$

As described in Chapter 3, in a p-type silicon sensor, radiation damage modifies the bulk by removing donors and creating acceptor-like defects, which introduce unknown changes to the doping concentrations. As a result, Equation (2.4.2) becomes irrelevant, and the effective doping concentration can instead be obtained from

$$N_{\text{eff}} = \frac{2\varepsilon\varepsilon_0}{e} \frac{V_{\text{dep}}}{D^2}, \quad (2.4.3)$$

which is valid for both unirradiated and irradiated sensors.

2.4.4 Charge Collection

Ionising particles deposit energy as they traverse the sensor, creating electron-hole pairs proportional to the energy loss. The internal electric field, enhanced by the applied voltage bias, causes these charge carriers to drift toward the electrodes and induces current.

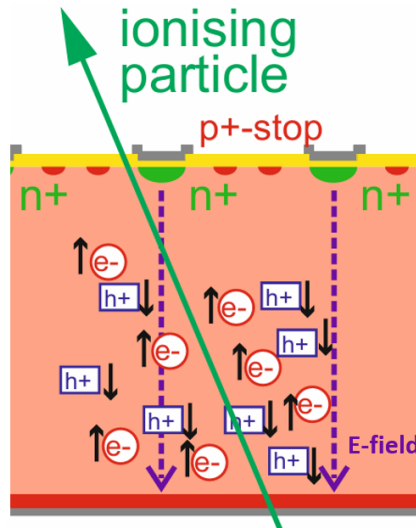


Figure 2.4.2: An ionising particle traversing the volume of a silicon sensor, depositing energy that generates electron-hole pairs. Electrons and holes drift in opposite directions under the internal electric field. Credit: [23].

Electrons move toward the n-side and the holes toward the p-side, as illustrated in Figure 2.4.2. The collected charge is given by

$$Q = \int I(t)dt = \{\text{Ohm's Law}\} = \int \frac{V(t)}{R}dt, \quad (2.4.4)$$

where $I(t)$ is the measured current and $V(t)$ the corresponding voltage signal.

The collected charge increases with depletion width, as a larger fraction of the generated electron-hole pairs is collected because recombination in undepleted regions decreases. In a fully depleted unirradiated sensor, the collected charge reaches a plateau, indicating that all charge carriers generated in the active volume are efficiently collected. This plateau can be used to determine the depletion voltage, similarly to CV measurements [22, 23].

CHAPTER 3

RADIATION DAMAGE & ANNEALING

In HEP detectors such as CMS, silicon detectors are positioned close to the interaction point, where they are exposed to high fluence of charged and neutral particles. These particles interact with the silicon lattice, depositing energy and displacing atoms from their regular positions. Over time, this exposure leads to cumulative degradation of the detector material, referred to as radiation damage. Understanding the impact of this damage on the electrical and operational characteristics of silicon sensors, which for sufficiently large sensors represents the bulk material behaviour, is essential for optimising performance and ensuring reliable operation under extreme irradiation.

This chapter first presents the mechanisms of radiation damage, focusing on bulk damage caused by non-ionising interactions in §3.1. §3.2 discusses how electrical characteristics, such as leakage current, effective doping concentration, and charge collection due to trapping, change with radiation damage. Silicon sensors can partially reverse radiation-induced damage by exposure to thermal energy, an effect known as beneficial annealing. Exposure to temperatures above 0 °C for a sufficient duration can damage the bulk, known as reverse annealing. Both of these effects are described in §3.3.

For more detailed information, the following theory of radiation damage and annealing is based mainly on *Radiation Damage in Silicon Particle Detectors*, *Particle Detector Fundamentals and Applications*, and *Evolution of Silicon Sensor Technology in Particle Physics* [22, 23, 25].

3.1 Radiation Damage Mechanism

There are two types of radiation damage, bulk damage and surface damage. Surface damage is caused by ionising particles, where traversing particles deposit energy via the electromagnetic force. This energy primarily affects the $Si - SiO_2$ interfaces, influencing sensor operation and readout performance. In silicon sensors, ionisation is largely reversible and does not leave permanent damage in the bulk [22]. Therefore, this thesis will not discuss ionising energy loss in further detail, but instead focus on radiation damage arising from non-ionising interactions.

Bulk damage, originating from non-ionising interactions by hadrons, e.g., neutrons, protons, or higher energetic leptons, is caused by direct collisions which displace atoms from their lattice positions. The collisions can knock atoms out of place, creating defects such as vacancies and interstitials, and more complex structures, e.g., di-vacancies V_2 and di-interstitials I_2 , as illustrated in Figure 3.1.1. Vacancies and interstitials are mobile within the lattice and can form defect complexes with impurities.

Simulations of short-distance Frenkel pairs, i.e., one vacancy together with its corresponding interstitial, have shown that 60 % pairs, up to 75 % – 90 % in disordered regions,

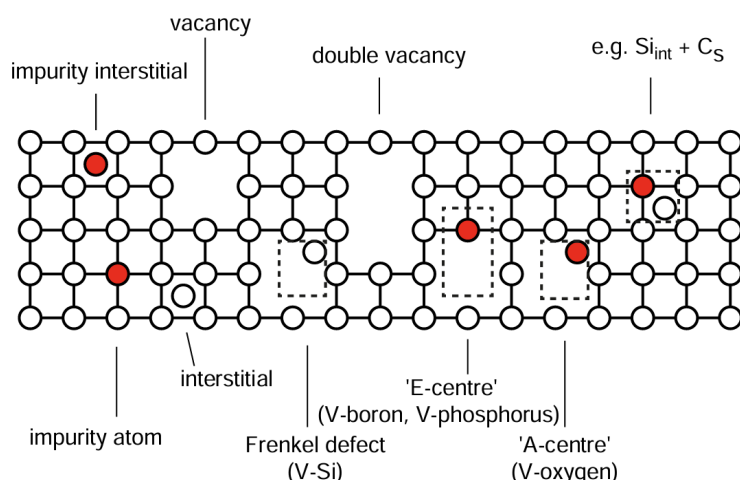


Figure 3.1.1: Vacancies and interstitials are created from non-ionising interaction with the lattice. Vacancies are when lattice atoms are knocked out of their regular position, and interstitials are when a displaced atom comes to rest at a non-lattice site somewhere else in the crystal. The vacancy together with the interstitial, in short distance, forms a Frenkel pair. Credit: [22].

annihilate at room temperature, leaving no permanent damage in the bulk [26]. The permanent damage to the silicon bulk is caused by defects within clusters, as illustrated in Figure 3.1.2, or the remaining vacancies and interstitials that migrate through the lattice and create stable defects with impurities or with each other [25].

To displace a silicon atom from its lattice position, a minimum energy exceeding the displacement threshold of approximately 25 eV is required [27]. The maximum kinematic energy transferred to a recoiling lattice atom of mass M by an incoming particle of mass m and kinetic energy E_{kin} is given by [22]

$$E_{kin,max} = 4 \frac{Mm}{(M+m)^2} E_{kin}. \quad (3.1.1)$$

If the kinematic energy of the primary knocked-out atom is sufficiently large, it can further displace other atoms from their lattice positions. As a result, point defects are created along the particle path through the bulk, and high-energy recoils can form defect clusters, as illustrated in Figure 3.1.2.

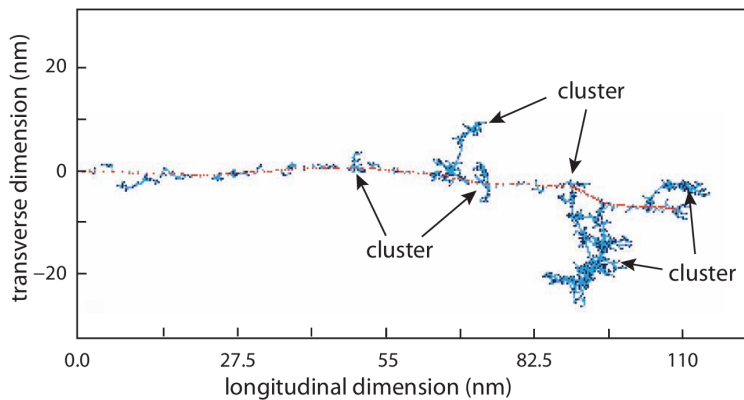


Figure 3.1.2: Simulated lattice damage, showing both point defects along the particle path and clusters from high-energy recoils, from a primary lattice atom with a recoil energy of 50 keV caused by 1 MeV neutrons. Credit: [22].

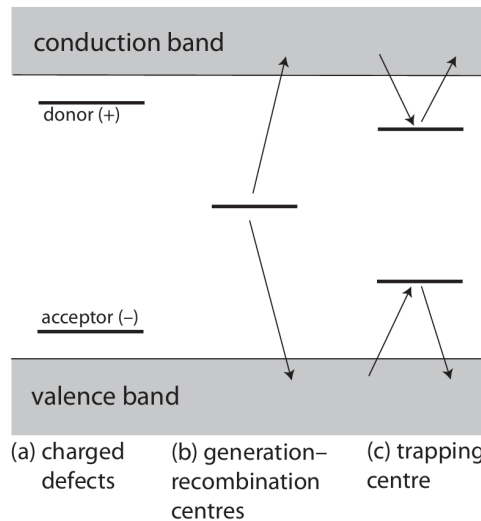


Figure 3.2.1: New energy levels caused by radiation damage: (a) donor and acceptor centres, (b) generation-recombination centres, and (c) trapping centres. Credit: [22].

3.2 Change of Sensor Characteristics

Defects caused by radiation introduce new energy levels within the band gap, changing the electrical characteristics of silicon sensors, including leakage current, saturation voltage, and charge collection efficiency. The three main consequences of defect-induced energy levels are illustrated in Figure 3.2.1, resulting in (a) generation of donor and acceptor centres, (b) leakage current through generation-recombination centres, and (c) creation of trapping centres. The relative importance of these effects depends on the amount of radiation damage. At fluences of $\Phi_{eq} = 10^{14} \text{ n}_{\text{eq}}/\text{cm}^2$, leakage current becomes the dominant problem. For $\Phi_{eq} = 10^{15} \text{ n}_{\text{eq}}/\text{cm}^2$, the saturation voltage becomes problematic, and from $\Phi_{eq} = 10^{16} \text{ n}_{\text{eq}}/\text{cm}^2$, the charge collection efficiency degradation becomes a fundamental problem [23]. The following sections discuss these three defect types and their impact on the electrical characteristics.

3.2.1 Leakage Current

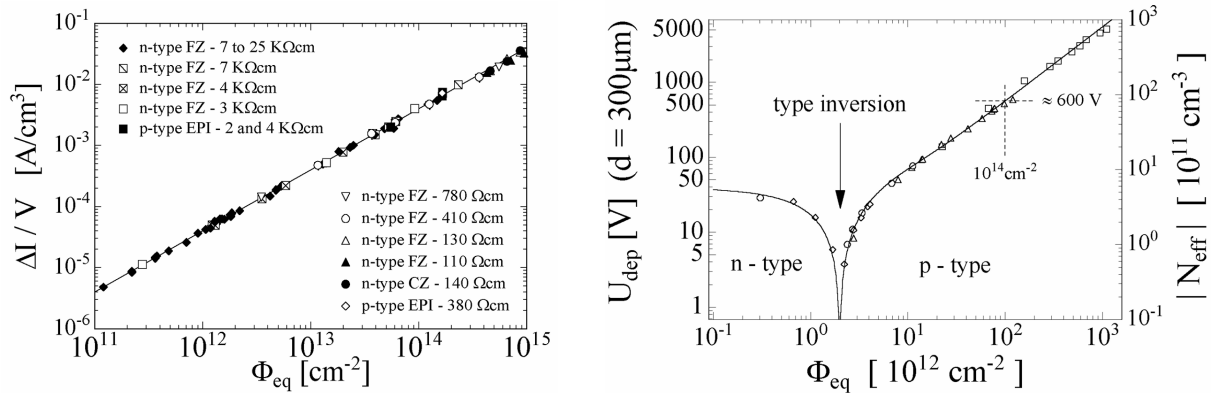
The new energy levels responsible for increased leakage current are generation-recombination centres located near the middle of the band gap, as shown in Figure 3.2.1(b). As these centres lie closer to both the valence and conduction bands, thermal excitation of electron-hole pairs occurs more easily, leading to an increased leakage current [22]. The leakage current scales linearly with fluence and can be expressed as

$$\Delta I = \alpha \Phi_{eq} V_{bias}, \quad (3.2.1)$$

where α is the current related damage rate, V_{bias} the applied voltage bias, Φ_{eq} the 1 MeV neutron equivalent fluence per cm^2 [25].

For a fixed annealing duration and temperature, see §3.3 for the definition of annealing, α becomes a universal constant when the leakage current is normalised to a temperature of 20 °C. The measured current can be converted to a target temperature using

$$I_{conv} = I_{meas} \cdot \left(\frac{T_{target}}{T_{meas}} \right)^2 \exp \left(-\frac{E_A}{2k_B} \left(\frac{1}{T_{target}} - \frac{1}{T_{meas}} \right) \right), \quad (3.2.2)$$



(a) Normalised leakage current to 20 °C as a function of fluence after 80 min annealing time at 60 °C. Credit: [25].

(b) Depletion voltage and effective charge carrier concentration as a function of fluence. Credit: [28].

Figure 3.2.2: Silicon sensor characteristics as functions of fluence Φ_{eq} , normalised to damage caused by 1 MeV neutrons.

where T_{target} is the target temperature, T_{meas} the measured temperature, k_B the Boltzmann constant, and E_A the activation energy of silicon.

α can be determined by first converting the measured leakage current to 20 °C using Equation (3.2.2). The converted current can then be normalised by the applied voltage bias and plotted as a function of fluence. The slope of the current-volume normalisation as a function of fluence corresponds to α , as shown in Figure 3.2.2a.

3.2.2 Effective Doping Concentration

Radiation creates defects that neutralise donors and acceptors, thereby changing the effective doping concentration. In n-type silicon sensors with phosphorus donors, donor removal ($P + V \rightarrow V P$ centre) and the formation of acceptor-like states (e.g. $V + V + O \rightarrow V_2 O$) introduce additional donor and acceptor energy levels in the band gap, as shown in Figure 3.2.1(a). As a result, n-type silicon sensors undergo type inversion, reversing the sign of the space charge from positive to negative [28]. After inversion, or for initially p-type sensors, the effective doping concentration continues to increase, leading to a higher saturation voltage.

3.2.3 Trapping

Trapping centres, as illustrated in Figure 3.2.1(c), can capture and release electrons and holes. Trapping reduces the carrier lifetime and the mean free path λ , thereby reducing the signal amplitude. The resulting impact is quantified by the Charge Collection Efficiency (CCE), defined as

$$CCE = \frac{Q_{irradiated}}{Q_{unirradiated}}, \quad (3.2.3)$$

where $Q_{irradiated}$ is the collected charge in an irradiated sensor, and $Q_{unirradiated}$ the collected charge in an unirradiated sensor of equal thickness [23].

At fluences of $\Phi_{eq} = 10^{15}$ n_{eq}/cm², trapping becomes a limiting factor for silicon sensors. The carrier mean free path can be expressed as

$$\lambda = v_D \tau_{eff}, \quad (3.2.4)$$

where v_D is the carrier drift velocity, and τ_{eff} the effective carrier lifetime. Using an electron drift velocity of $v_D = 10^7$ cm/s, the electron mean free path in silicon becomes

$$\begin{aligned}\tau_{eff}(\Phi_{eq} = 10^{15}) &= 2 \text{ ns} \rightarrow \lambda_e = 200 \mu\text{m} \\ \tau_{eff}(\Phi_{eq} = 10^{16}) &= 0.2 \text{ ns} \rightarrow \lambda_e = 20 \mu\text{m}.\end{aligned}$$

These values indicate that at high fluences, charge carriers generated by ionising particles may not reach the electrodes, thereby decreasing the CCE.

Sufficiently high bias voltages increase the electric field and the carrier drift velocity, reducing trapping probability. As a result, thinner sensors exposed to fluences below $\Phi_{eq} = 10^{15}$ n_{eq}/cm² can achieve a CCE close to 100 % [23].

3.3 Annealing

Radiation-induced damage in silicon sensors depends on temperature, as vacancies and interstitials become mobile above a certain threshold. Defects affecting leakage current, effective doping concentration, and charge collection begin to migrate at temperatures above 0 °C. At these temperatures, defects move through the lattice until they recombine with their counterparts ($V + I \rightarrow Si$) or form new defect complexes through association with identical or other impurities, e.g., multi-vacancy or multi-interstitial combinations such as $V + V \rightarrow V_2$ [23]. Exposing sensors to thermal energy causes physical changes in the crystal lattice, referred to as annealing. This process is divided into short- and long-term annealing, also known as beneficial and reverse annealing.

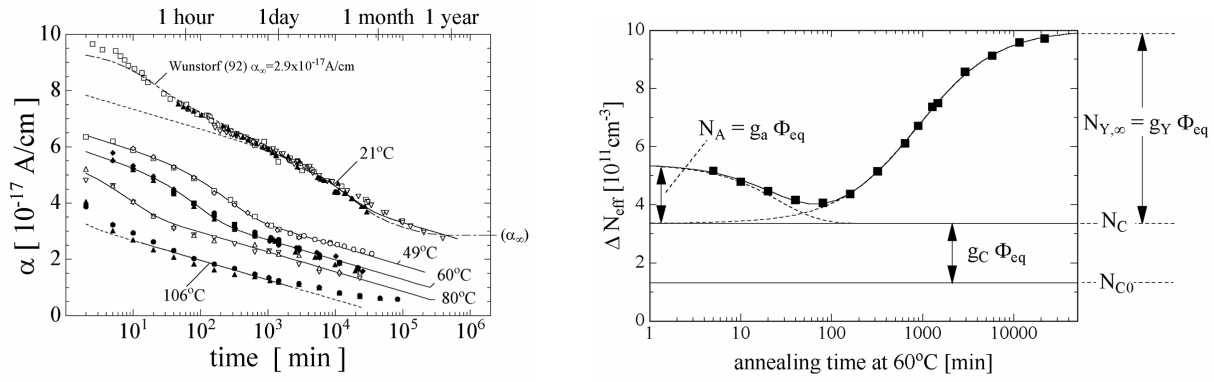
3.3.1 Leakage Current

The change of the current related damage rate α , during annealing, is temperature dependent and is illustrated in Figure 3.3.1a for different temperatures. According to [25], the behaviour of α during long-term annealing at room temperature and at higher temperatures can be parametrised as

$$\alpha = \alpha_0 + \alpha_I \cdot \exp\left(-\frac{t}{\tau_I}\right) - \beta \cdot \ln\left(\frac{t}{t_0}\right), \quad (3.3.1)$$

where α_0 , α_I , τ_I , and β are fit parameters.

The parameterisation describes an initial phase dominated by an exponential decrease in α , followed by a slower logarithmic decay at longer annealing times. At lower temperatures, α may flatten out. This behaviour is temperature dependent and is frozen out at temperatures below 0 °C. At room temperature and higher temperatures, the leakage current and the corresponding damage rate α are expected to decrease with increasing annealing time.



(a) Leakage current damage rate α as function of annealing time at different temperatures.

(b) Change in effective doping concentration ΔN_{eff} , as function of annealing time at 60 °C.

Figure 3.3.1: α and N_{eff} as functions of annealing time. α decreases with increasing annealing time, while N_{eff} first decreases and then increases, corresponding to beneficial and reverse annealing. Credit: [25].

3.3.2 Effective Doping Concentration

The effective doping concentration N_{eff} is affected by both beneficial and reverse annealing. Beneficial annealing corresponds to an increase of donor-like defects rather than acceptor removal [29]. In contrast, reverse annealing is associated with an increase of acceptor-like defects, similar to those caused by radiation damage, as described in §2.4.3. The change of effective doping concentration ΔN_{eff} as a function of annealing time is illustrated in Figure 3.3.1b, where the decrease up to the minimum corresponds to beneficial annealing, and the increase reflects reverse annealing. The change of effective doping concentration can be written as,

$$\Delta N_{eff}(\Phi_{eq}, t(T_a)) = N_{eff,0} - N_{eff}(\Phi_{eq}, t(T_a)). \quad (3.3.2)$$

where Φ_{eq} is the 1 MeV neutron equivalent fluence, t the annealing time, T_a the annealing temperature, and $N_{eff,0}$ the effective doping concentration before irradiation.

This equation can be further divided into three contributions,

$$\Delta N_{eff}(\Phi_{eq}, t(T_a)) = N_A(\Phi_{eq}, t(T_a)) + N_C(\Phi_{eq}, t(T_a)) + N_Y(\Phi_{eq}, t(T_a)), \quad (3.3.3)$$

also known as the Hamburg model. The three terms represent beneficial annealing N_A , reverse annealing N_Y , and a stable component independent of annealing N_C [25].

The beneficial annealing contribution is described as,

$$N_A(t) = g_A \Phi e^{-t/\tau_A}, \quad (3.3.4)$$

where g_A is the introduction rate. τ_A is a temperature-dependent time constant, describing how fast the annealing progresses at a given temperature, defined as

$$\frac{1}{\tau_A} = k_{0A} \exp\left(-\frac{E_{aA}}{k_B T_a}\right), \quad (3.3.5)$$

where E_{aA} is the activation energy, k_{0A} the frequency factor, and k_B the Boltzmann constant. It has been found in [25] that parameters describing the beneficial annealing

of N_{eff} are similar to those describing the exponential decay of α , indicating that the annealing involves similar microscopic defects.

Reverse annealing is represented by

$$N_Y(t) = g_Y \Phi_{eq} (1 - e^{-t/\tau_Y}), \quad (3.3.6)$$

which describes the build-up of acceptor-like defects, causing the space charge to become more negative. The separation of N_A and N_Y is necessary because the annealing effects immediately after irradiation differ from the effects at longer annealing times, resulting in different activation energies and time constants. At $t = 0$, the beneficial term dominates with an amplitude of $g_A \Phi_{eq}$, but becomes small after approximately 80 minutes at 60 °C [25]. At longer annealing times, the reverse annealing contribution dominates, and the change of effective doping concentration approaches saturation with amplitude $g_Y \Phi_{eq}$, in addition to the contribution from the stable term.

The stable contribution, independent of annealing time and temperature, is given by

$$N_C = N_{C,0} (1 - e^{-c \Phi_{eq}}) + g_C \Phi_{eq}, \quad (3.3.7)$$

where g_C is the introduction rate of stable acceptors, c the removal constant, and $N_{C,0}$ the initial removal of donor concentration after irradiation.

CHAPTER 4

METHODOLOGY

As mentioned in §1.7, the objective of this thesis is to investigate radiation hardness and annealing effects of silicon diodes under conditions similar to the operational timeline of the HL-LHC, and compare the results with the previously studied HF campaign. This chapter describes the experimental methodology used to achieve this goal.

The silicon test diodes used in this study are diced from 8-inch silicon wafers and have thicknesses of 300 µm, 200 µm, and 120 µm. The diodes, their corresponding cross sections, and the influence of the surrounding guard ring are described in §4.1. To simulate the radiation conditions expected during Run 4 and Run 5 of the HL-LHC, a total of 36 diodes were irradiated at the TRIGA nuclear reactor. An overview of the irradiation procedure, together with the DI, DI SR, and HF campaigns, is presented in §4.2.

After each irradiation round, the diodes were characterised using the IVCV probe setup, in which Current-Voltage (IV) and Capacitance-Voltage (CV) measurements were performed. These measurements were used to identify damaged diodes or deviations in the electrical characterisations within groups of identical fluence and thickness, as discussed in §4.3.1. From the 36 irradiated diodes, 21 were selected for the DI/DI SR campaign, with seven diodes per annealing temperature of 20.5 °C, 40 °C, and 60 °C.

In addition to leakage current and saturation voltage extracted from IV and CV measurements, charge collection was measured using the Transient Current Technique (TCT). These measurements were performed in the IVCV & TCT setup described in §4.3.2. All data used in the DI SR and HF comparison were acquired using this setup. After each measurement cycle, consisting of IV, CV, and TCT measurements, the diodes were annealed before the next cycle, as described in §4.5. To prevent unintended annealing between measurements, the diodes were stored at –20 °C.

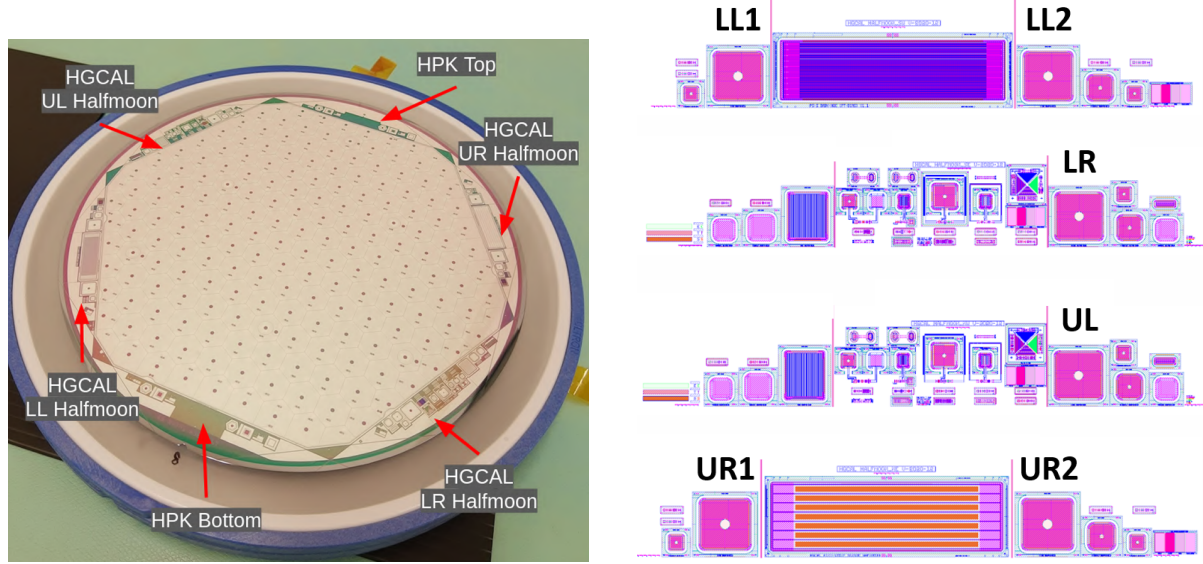
Improvements to the Python software used to run the IVCV & TCT setup are presented in §4.3.3. The newly developed Python-based Graphical User Interface (GUI) software for data analysis, used to produce all plots and analyses presented in this thesis, is described in §4.4, together with the algorithm used to extract the saturation voltage from CV and TCT data.

The IVCV probe station described in §4.3.1 has been used in previous studies [30, 31], while the IVCV & TCT setup presented in §4.3.2 was used to study the HF campaign in [21].

4.1 Silicon Wafer and Test Diodes

As mentioned in §1.6, the HGCAL will be based on p-type silicon modules manufactured from 8-inch (20.32 cm) circular wafers in three different thicknesses, 300 µm, 200 µm, and

$120\text{ }\mu\text{m}$, produced by Hamamatsu Photonics K.K. [32]. P-type bulk material is chosen because of its radiation hardness and signal-to-noise performance, and because it avoids type inversion after irradiation, as discussed in §3.2.2. To maximise the utilisation of the wafer area, they are diced in a hexagonal shape, leaving residual half-moon regions containing test structures as illustrated in Figure 4.1.1b. One type of test structure used in this study is the $0.5 \cdot 0.5\text{ cm}^2$ test silicon diode, labelled according to its half-moon position as Lower Left (LL), Lower Right (LR), Upper Left (UL), and Upper Right (UR). Each of these diodes shares the same electrical characteristics as the other 192 and 432 individual hexagonal cells of the LD and HD sensors.



(a) LD silicon sensor before being diced into a hexagonal shape. The red arrows are pointing to the respective half-moons, two half-moons to Hamamatsu, and four to CMS HGCAL. Credit: [30].

(b) Test structures on the half-moons, diced from the 8-inch silicon wafer. Modified from [33].

Figure 4.1.1: Full 8-inch LD silicon sensors for CMS HGCAL with the corresponding test structures

The cross sections for all three thicknesses $300\text{ }\mu\text{m}$, $200\text{ }\mu\text{m}$, and $120\text{ }\mu\text{m}$ are shown in Figure 4.1.2. To achieve precise position resolution and electrical isolation between neighbouring electrodes, denoted as n^+ pad, a p-stop implant is introduced. Signal readout is provided by metal contacts placed above the p-type bulk, with a thin silicon dioxide layer acting as a coupling dielectric. To protect the diode from environmental effects and ensure electrical isolation, the top surface is covered with a passivation layer of silicon dioxide [34].

Three test diodes located on two half-moons, LL and LR/UL, are shown in Figure 4.1.3. Each diode is surrounded by a guard ring, which can be either floating or grounded. In this study, the guard ring is grounded, which smooths the electric field at the edges, improving breakdown voltage and reducing the leakage current contributions from the surface [23, 35].

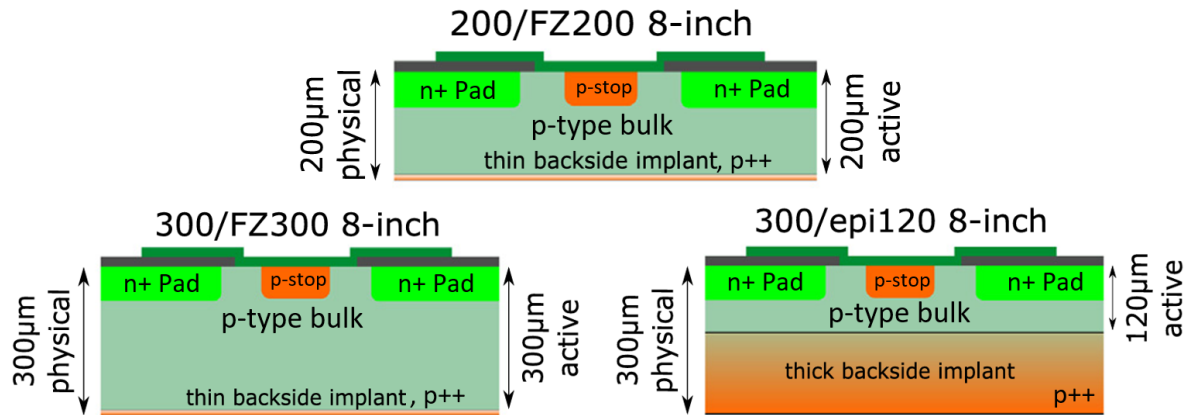


Figure 4.1.2: Cross section of silicon diodes of thicknesses 300 μm , 200 μm , and 120 μm . Schematics not to scale. Modified from [33].



Figure 4.1.3: Test structures on two half-moons diced from an 8-inch silicon wafer.

4.2 Campaign Overview & Irradiation of Unpowered Test Diodes

The three campaigns, Double Irradiation (DI), Double Irradiation Second Round (DI SR), and High Fluence (HF), are divided into three annealing temperature groups, 20.5 $^{\circ}\text{C}$, 40 $^{\circ}\text{C}$, and 60 $^{\circ}\text{C}$. As mentioned in §1.7, the HF campaign was exposed to fluences corresponding to the end of the HL-LHC. The DI campaign was exposed to one quarter of the HF campaign with beneficial annealing, mimicking Run 4 and Long Shutdown 4. A subsequent second round of irradiation, mimicking Run 5 and reaching fluences similar to HF, defines the DI SR campaign. Each HF group contains seven diodes, except the diode with 40 $^{\circ}\text{C}$, thickness 200 μm , and fluence $8 \cdot 10^{15} \text{ n}_{\text{eq}}/\text{cm}^2$. Similarly, the DI and DI SR campaigns contain seven diodes per temperature group, except the 20.5 $^{\circ}\text{C}$ 200 μm $6 \cdot 10^{15} \text{ n}_{\text{eq}}/\text{cm}^2$ diode, which was unfortunately damaged during transfer from the PCB for the second irradiation.

As introduced in §1.5, FLUKA simulations predicted an expected end-of-lifetime fluence close to the collision point of $1 \cdot 10^{16} \text{ n}_{\text{eq}}/\text{cm}^2$. To include an upper safety margin, the fluences were increased by 50 %. To simulate the radiation conditions of the HL-LHC,

36 test diodes were sent to the TRIGA Nuclear reactor at the Jožef Stefan Institute, Ljubljana, Slovenia [36, 37]. The diodes were irradiated in two rounds, the first with fluences from $5 \cdot 10^{14} \text{ n}_{\text{eq}}/\text{cm}^2$ to $4 \cdot 10^{15} \text{ n}_{\text{eq}}/\text{cm}^2$, and the second round of irradiation reaching final fluences of $2 \cdot 10^{15} \text{ n}_{\text{eq}}/\text{cm}^2$ to $1.5 \cdot 10^{16} \text{ n}_{\text{eq}}/\text{cm}^2$.

During irradiation in the TRIGA reactor, the diodes experience in-reactor temperatures starting at 25°C and reaching a maximum between 45°C and 55°C [38]. The temperature is recorded every 15 seconds and is used to determine the in-reactor annealing times. The in-reactor annealing time at 60°C is calculated using Arrhenius scaling from Equation (4.5.1), together with the activation energies extracted from the HF campaign [21]. These annealing times are subsequently scaled to 20.5°C and 40°C using the temperature scaling parameters in [21]. For fluences equal to or above $2 \cdot 10^{15} \text{ n}_{\text{eq}}/\text{cm}^2$, the temperature reaches approximately 50°C . As a result, diodes irradiated below this fluence experience significantly reduced in-reactor annealing, because most annealing occurs at temperatures close to 50°C . The resulting in-reactor annealing times are summarised in Table 4.2.1 together with the corresponding campaign, thickness, fluence, and annealing temperature for each diode.

Table 4.2.1: Overview of the three campaigns, DI, DI SR, and HF, listing the thickness, total fluence, annealing temperature, and in-reactor annealing time of each diode. The annealing times are calculated using a maximum reached temperature of $50^\circ\text{C} \pm 5^\circ\text{C}$.

Campaign	D [μm]	$\Phi_{\text{eq}} [\frac{\text{n}_{\text{eq}}}{\text{cm}^2}]$	$t_{20.5^\circ\text{C}}[\text{min}]$	$t_{40^\circ\text{C}}[\text{min}]$	$t_{60^\circ\text{C}}[\text{min}]$
DI	300	$5.0 \cdot 10^{14}$	0	0.0	0.00
DI	300, 200	$1.0 \cdot 10^{15}$	4^{+3}_{-2}	$0.3^{+0.2}_{-0.1}$	$0.03^{+0.02}_{-0.01}$
DI	200	$1.5 \cdot 10^{15}$	83^{+76}_{-41}	$5.9^{+5.4}_{-2.9}$	$0.54^{+0.50}_{-0.27}$
DI	120	$1.5 \cdot 10^{15}$	69^{+56}_{-31}	$6.0^{+4.8}_{-2.7}$	$0.74^{+0.59}_{-0.33}$
DI	200	$2.0 \cdot 10^{15}$	304^{+263}_{-145}	$21.6^{+19.8}_{-10.3}$	$2.0^{+1.70}_{-1.00}$
DI	120	$4.0 \cdot 10^{15}$	854^{+614}_{-365}	$74.1^{+53.3}_{-31.7}$	$9.10^{+6.52}_{-3.89}$
DI SR	300	$2.0 \cdot 10^{15}$	199^{+174}_{-95}	$14.2^{+12.2}_{-6.8}$	$1.30^{+1.14}_{-0.62}$
DI SR	300, 200	$4.0 \cdot 10^{15}$	660^{+558}_{-305}	$47.0^{+39.0}_{-21.8}$	$4.32^{+5.71}_{-2.30}$
DI SR	200	$6.0 \cdot 10^{15}$	1449^{+1196}_{-667}	$104.0^{+83.0}_{-58.0}$	$9.48^{+7.74}_{-4.37}$
DI SR	120	$6.0 \cdot 10^{15}$	1026^{+735}_{-439}	$89.0^{+64.0}_{-38.0}$	$10.90^{+7.80}_{-4.66}$
DI SR	200	$8.0 \cdot 10^{15}$	2177^{+1667}_{-998}	$155.0^{+126.0}_{-64.0}$	$14.20^{+11.60}_{-6.50}$
DI SR	120	$1.5 \cdot 10^{16}$	1467^{+1031}_{-620}	$127.0^{+89.0}_{-54.0}$	$15.58^{+10.95}_{-6.58}$
HF	300	$2.0 \cdot 10^{15}$	304^{+263}_{-145}	$21.6^{+19.8}_{-10.3}$	$2.0^{+1.70}_{-1.00}$
HF	300, 200	$4.0 \cdot 10^{15}$	1197^{+982}_{-551}	$85.0^{+70.0}_{-39.0}$	$7.8^{+6.40}_{-3.60}$
HF	200	$6.0 \cdot 10^{15}$	2177^{+1667}_{-998}	$155.0^{+126.0}_{-64.0}$	$14.2^{+11.60}_{-6.50}$
HF	120	$6.0 \cdot 10^{15}$	1527^{+1086}_{-770}	$133.0^{+97.0}_{-56.0}$	$16.2^{+11.50}_{-6.90}$
HF	200	$8.0 \cdot 10^{15}$	3157^{+2551}_{-1443}	$225.0^{+181.0}_{-103.0}$	$20.7^{+16.70}_{-9.40}$
HF	120	$1.5 \cdot 10^{16}$	4326^{+3058}_{-1835}	$376.0^{+266.0}_{-160.0}$	$45.9^{+32.50}_{-19.40}$



(a) Temperature-controlled chuck, needles, and DUT inside the conductive box.

(b) Close-up on needles connected to the pad and the guard ring of the DUT.

Figure 4.3.1: Overview of the probe station to perform IV and CV measurements of the $0.5 \cdot 0.5 \text{ cm}^2$ diodes. Credit: [30].

4.3 Measurement Setups

After each round of irradiation, measurements in the IVCV probe station setup, described in §4.3.1, are performed to identify damaged diodes or deviations in electrical characteristics within groups of identical fluence and thickness. The diodes are then mounted to PCBs using high-conductivity glue for IV, CV, and TCT measurements in the IVCV & TCT setup described in §4.3.2. Improvements to the software used to run the latter setup are described in §4.3.3, focusing on the implementation that reduces TCT data acquisition time by 80 %.

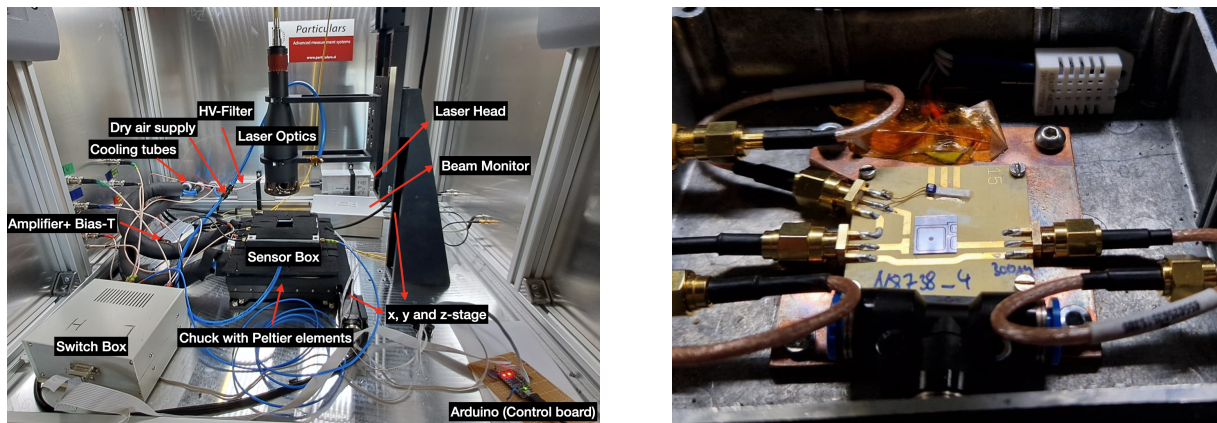
4.3.1 IVCV Setup - Probe Station

To perform IV and CV measurements in the probe station, the Device Under Test (DUT) is placed on a temperature-controlled chuck operated at $-20^\circ\text{C} \pm 1^\circ\text{C}$. Cooling is required as the leakage current is strongly temperature dependent, as mentioned in §2.4.1, and reducing the temperature limits the risk of damage when the current exceeds $100 \mu\text{A}$. The chuck is enclosed in a conductive box that acts as a Faraday cage to protect the DUT from light, and is flushed with dry air to lower humidity to prevent condensation and frost.

As illustrated in Figure 4.3.1b, two probe needles are connected to the DUT, one to the pad for signal readout and the other to the guard ring, which is grounded. Both IV and CV measurements are performed by ramping the reverse voltage bias from -25 V to -500 V in steps of 25 V with the reverse voltage bias applied to the backside of the diode.

The leakage current from IV measurements is measured using a picoammeter. Capacitance in CV measurements is determined with an LCR meter by measuring the phase shift and amplitude of the resulting current. A small AC signal of 0.5 V at 2 kHz is applied across the diode while the reverse voltage bias is applied as a DC signal. A switch box is used to change between IV and CV measurements [30, 31].

After completing the initial IV and CV measurements, the leakage current and capacitance



(a) Components inside the Faraday cage.
Credit: [40].

(b) DUT on a PCB inside the sensor box.

Figure 4.3.2: Overview of the IVCV & TCT setup. Displaying only the components inside the Faraday cage and not the instruments outside the cage.

are plotted as a function of the applied voltage. As mentioned earlier, this step identifies damaged diodes or deviations in electrical characteristics within groups of identical fluence and thickness. An example of a leakage current deviation is shown in §A.2. In total, 21 diodes were selected for the DI/DI SR campaigns and mounted on PCBs for measurements in the IVCV & TCT setup.

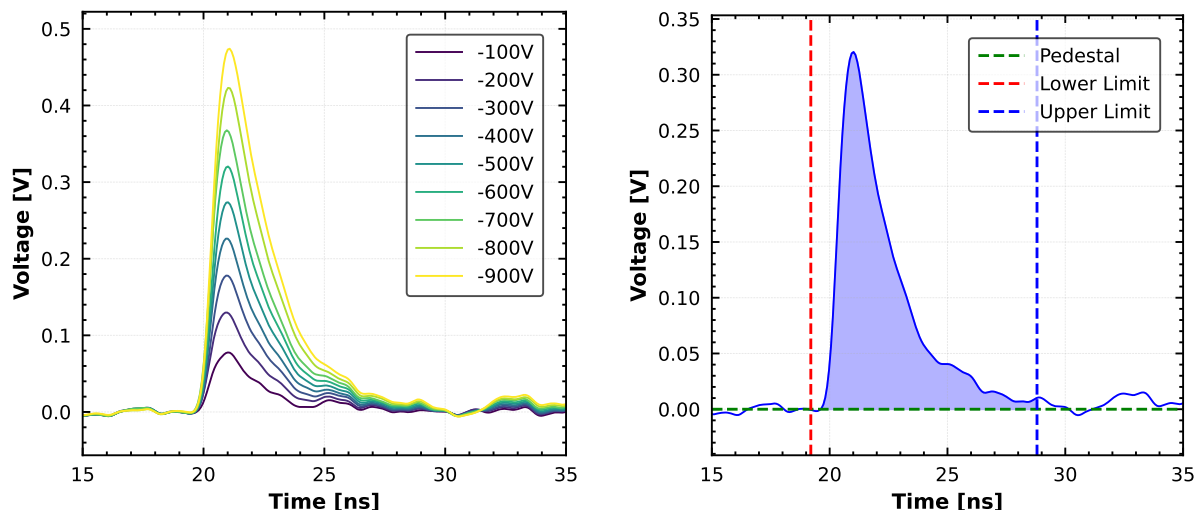
4.3.2 IVCV & TCT Setup - Test Diode on PCB

All data used in the final analyses of this thesis were measured using the IVCV & TCT setup based on a laser system provided by Particulars [39]. The DUT, glued onto a PCB, is shown in Figure 4.3.2b. As in the IVCV probe station setup, the pad is connected to the signal readout line and the guard ring is grounded, both via wire bonding. The components used for IV, CV, and TCT measurements inside the Faraday cage are shown in Figure 4.3.2a.

The PCB has been soldered with three connectors. The bottom right is connected to the High Voltage (HV) line, the bottom left to the readout line, and the top left to a PT1000 temperature sensor. The PT1000 is a positive temperature coefficient thermistor that increases in resistance with increasing temperature and is used to monitor PCB temperature.

All IV, CV, and TCT measurements are performed at $-20^{\circ}\text{C} \pm 1^{\circ}\text{C}$. This temperature is achieved by placing the PCB on a copper plate cooled by Peltier elements and a chiller pumping ethanol at -30°C . The PCB is enclosed in a small sensor box, located inside the larger Faraday cage. Both are flushed with dry air to reduce humidity to prevent condensation and frost. An Arduino controls the switch box, which is used to switch between measurement circuits, and monitors data from temperature and humidity sensors located inside the sensor box and the Faraday cage.

IV and CV measurements are performed in a similar way to the IVCV probe station setup. For IV measurements, the leakage current is measured with a picoammeter connected to the HV line, while the pad and guard ring are grounded. CV measurements are performed using an LCR meter with a 0.5 V AC signal at 2 kHz. In both measurements,



(a) 10 000 waveforms averaged for each voltage step. A larger reverse voltage bias creates a stronger electric field, reducing the risk of trapping and resulting in a larger signal, i.e., higher charge collection.

Figure 4.3.3: Converted transient current signal to voltage signal for diode with thickness $200\text{ }\mu\text{m}$, fluence $8 \cdot 10^{15}\text{ n}_{\text{eq}}/\text{cm}^2$, and 1550 min annealing time at 40°C for the DI SR campaign.

a reverse voltage bias is applied to the backside of the diode, ranging from -25 V to -900 V in steps of 25 V . The saturation voltage extracted from CV measurements at 2 kHz underestimates the actual saturation voltage because of the frequency dependence of the capacitance [31, 40]. A value closer to the true saturation voltage can be extracted from charge collection as a function of voltage obtained from TCT measurements.

For TCT measurements, the sensor box is mounted on an XY-stage to align an infra-red laser with wavelength 1064 nm to the 1 mm circular opening at the centre of the diode. The laser operates at 1 kHz and is mounted on a Z-stage to adjust the focal point to inside the volume of the diode. The laser intensity is monitored using a $300\text{ }\mu\text{m}$ unirradiated reference diode, measured at the end of each day, since the laser intensity is temperature-dependent and varies daily. Another way to monitor the laser intensity is through the beam monitor located inside the Faraday cage, which directs 50 % of the optics to the DUT and 50 % to a photodiode.

The transient current signal from the DUT is amplified using a 53 dB amplifier. Noise is reduced by a bias-T placed before the amplifier, and the reduction of noise in the HV line is achieved using an HV filter and a bias-T. The amplifier input impedance of 50Ω is used to convert the transient current pulse into a voltage signal to the oscilloscope. TCT measurements are performed with a reverse voltage bias ranging from -100 V to -900 V in steps of 100 V . For each voltage step, 10 000 waveforms are averaged, and the charge collection is calculated by integrating the average voltage signal over a fixed time window and dividing by the amplifier gain [21]. The average waveforms and the integration window are shown in Figures 4.3.3a and 4.3.3b.

4.3.3 IVCV & TCT Software Development

All measurements in the IVCV & TCT setup are controlled by a single Python GUI. The software was developed before this thesis and further developed within the scope of this thesis. At the start of the HF campaign, TCT measurements were performed using a separate LabVIEW program, while IV and CV measurements were controlled through the Python GUI. During summer 2024, the TCT functionality was integrated into the Python GUI, enabling all measurements to be performed within a single program without any difference in the measured charge collection [41].

One complete measurement cycle for a single diode consists of:

1. Diode exchange, start chiller, wait for the temperature to stabilise at -20°C , and perform a position alignment of the laser to align it to the circular opening of the DUT. (20 min)
2. IV measurement from -25 V to -900 V in steps of 25 V . (13 min)
3. CV measurement from -25 V to -900 V in steps of 25 V . (13 min)
4. TCT measurement from -100 V to -900 V in steps of 100 V . (33 min)
5. Stop cooling and wait until temperature exceeds 3°C . (30 min)

At the beginning of this thesis, the Python GUI had three main limitations. First, the IV, CV, and TCT measurements were not automated, resulting in inefficient dead time between individual measurements. Second, safety features were missing, including checks for file name mismatches, leading to inconsistent file naming and unstructured data storage. Third, the TCT measurements were slow.

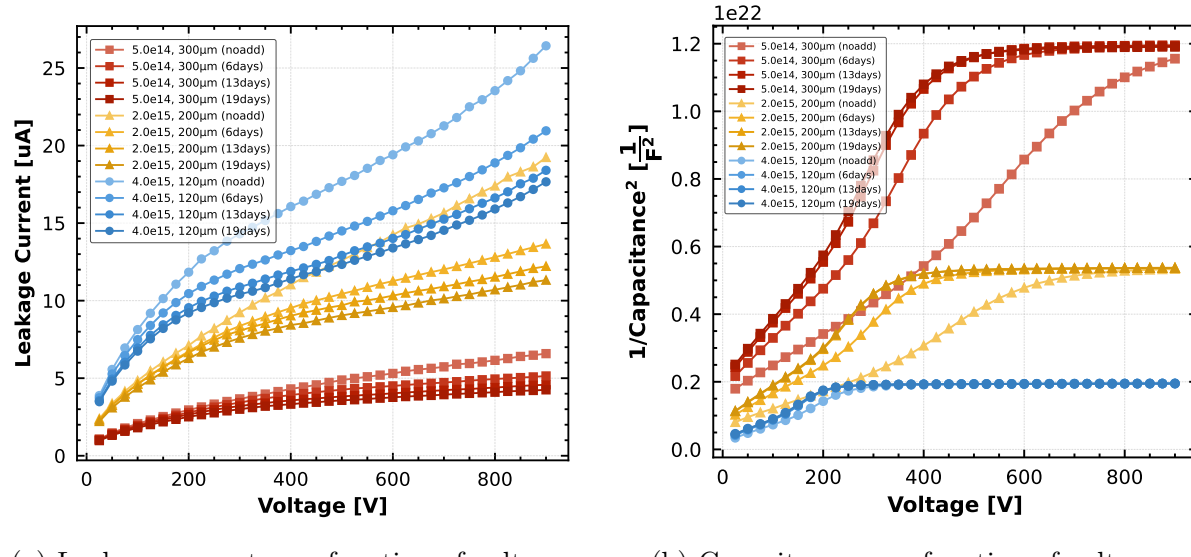
An optimisation study of the TCT measurement was done, as it was the bottleneck among the three individual measurements. At each voltage step, 200 average waveforms were recorded, with each average consisting of 50 individual waveforms. Previously, 200 individual communications were required per voltage step between the PC and the oscilloscope, one to acquire 50 waveforms and another to retrieve the average waveform. All 200 waveforms per voltage step were stored in compressed NumPy files for offline analysis.

The study identified the communication between the PC and the oscilloscope as the limiting factor. By enabling FastFrame mode on the oscilloscope, 10 000 waveforms, equivalent to 200×50 , could be acquired in a single query, followed by another to transfer the data to the PC and store it in the same format as before. As a result, the time required to perform a single TCT measurement decreased by almost 80 %, from 33 minutes to 7 minutes.

With automated measurements, safety features, and optimised TCT data acquisition, the number of diodes measured per day is now five to seven, representing an almost 50 % increase over the previous three to four. This improvement was essential for the scope of this thesis, as it enabled a larger dataset for comparison with the HF campaign.

4.4 Data Analysis - Developed Python GUI

During this thesis, a Python-based data analysis GUI was developed to simplify data access between the laboratory PC and external computers. All plots and analyses presented



(a) Leakage current as a function of voltage. (b) Capacitance as a function of voltage.

Figure 4.4.1: Leakage current and capacitance as functions of voltage of four full IV, CV, and TCT measurement cycles of each diode in a subset of the DI campaign at an annealing temperature of 20.5 °C. *Noadd* denotes diodes with no additional annealing beyond in-reactor annealing. Darker colours indicate longer annealing times, up to 19 days.

in this thesis were produced using this software.

Measurement metadata, including, e.g., diode ID, thickness, fluence, measurement data, and TCT correction factor, are stored in Google Sheets files. Previously, this information, together with absolute file paths, had to be manually coded into a Python file, resulting in databases that only functioned on specific computers. As multiple campaigns are ongoing in parallel, beyond the DI, DI SR, and HF campaigns, several users use the measurement setup and perform similar analyses using individual scripts.

The new software automatically creates a database with a single click by synchronising measurement data via Git, without hard-coded paths. Time-consuming saturation voltage fits extracted from CV and TCT data can therefore be shared between users. With the implemented safety features described in §4.3.3, file name mismatches are avoided, and a unique combination of diode ID and annealing time is used to retrieve metadata from the Google Sheets files. As a result, all users working on different campaigns obtain consistent information, analysis algorithms, and plot styles.

As a single click can generate the database, measurement data are checked before each annealing step to ensure data quality and consistency with the expected annealing behaviour. This step is essential, as annealing is irreversible. The expected electrical characteristics behaviour with annealing is as follows. Leakage current decreases with increasing annealing time. The saturation voltage decreases during beneficial annealing and increases during reverse annealing. Charge collection efficiency exhibit the opposite behaviour as the saturation voltage. Measurements that deviate from these expectations or show insufficient quality are repeated.

An example of this control check is shown in Figure 4.4.1, which presents leakage current and capacitance as functions of voltage for a subset of the 20.5 °C data from the DI campaign. Darker colours indicate longer annealing times. As shown in Figure 4.4.1a,

the leakage current decreases with annealing time, as expected. In Figure 4.4.1b, the capacitance “kink” shifts towards lower voltages with increasing annealing time, resulting in a decreasing saturation voltage consistent with beneficial annealing.

4.4.1 Saturation Voltage Extraction: CV & TCT Measurements

As discussed in §2.4.2 and §2.4.4, the saturation voltage is extracted from inverse capacitance squared and charge collection as a function of voltage, obtained from CV and TCT measurements.

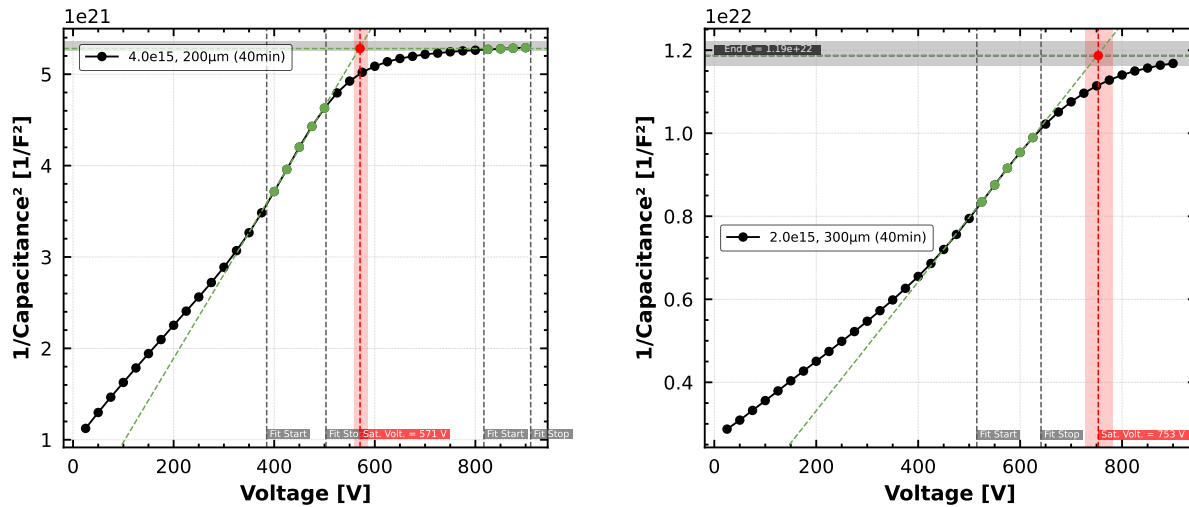
As the data varies with fluence, thickness, annealing time, and between CV and TCT measurements, the fitting procedure is non-trivial. For CV data, the saturation voltage is extracted from the capacitance plateau when observed, defined as the region where the capacitance is approximately constant. If no plateau is visible, an end capacitance assumption is applied. The end capacitance value is extracted as the mean of all observed plateaus across all campaigns for thicknesses of 300 μm , 200 μm , and 120 μm . The uncertainties in the end capacitance values were found to be -2% and $+3\%$, due to a wafer thickness variation of 10 μm . Both cases are illustrated in Figure 4.4.2, and the saturation voltage is extracted using a similar fit algorithm.

To incorporate uncertainties arising from the data, extract saturation voltage from both smooth and unstable datasets, and reduce bias from the user-defined fit range, manual fit intervals were implemented with the following algorithm. For the lower fit interval, corresponding to the linear slope before the “kink”, all possible combinations of data points are used to perform linear fits. For example, if six data points are enclosed, a linear fit is first performed using all points. Subsequent linear fits are obtained by excluding one point at a time until only three data points remain. Smooth data results in a smaller spread, while unstable data increases the resulting uncertainty.

For the upper fit, if a plateau is present, the interval is chosen to enclose it. The mean of the enclosed points defines the upper line, with an uncertainty of -0.5% and $+1.5\%$, resulting in three upper lines. The saturation voltage is defined as the mean of all intersection points between the lower linear fits and the upper lines. The minimum and maximum intersection values across all combinations give the asymmetric uncertainty.

For charge collection as a function of voltage, the same manual fit intervals are used. In contrast to CV data, irradiated diodes do not reach a plateau, and the upper line is not horizontal. Therefore, one linear fit is performed for each enclosed interval. The saturation voltage is extracted from the intersection of the lower and upper linear fits, with a fixed symmetric uncertainty of $\pm 5\%$. This uncertainty is determined from repeated TCT measurements of the same diode and analysis of the resulting variation in the extracted saturation voltage. The variation arises from the smaller number of data points and from larger fluctuations between neighbouring points compared to CV measurements. The fit-related uncertainties from CV measurements typically lie in the range of 1-3 %

If the “kink” in the charge collection occurs at high voltage, close to the reverse voltage bias measurement limit of -900 V , with a few points beyond it, or observed fluctuation in the charge collection after the “kink”, a synthetic upper line is introduced. The saturation voltage is obtained from the intersection of the lower linear fit and the synthetic line, again with a symmetric uncertainty of $\pm 5\%$.



(a) Diode with thickness 200 μm , fluence of $4 \cdot 10^{15} \text{ n}_{\text{eq}}/\text{cm}^2$ where the plateau is visible and fit interval can be used for both the linear part before the “kink” and for the plateau.

(b) Diode with thickness 300 μm and fluence of $2 \cdot 10^{15} \text{ n}_{\text{eq}}/\text{cm}^2$ where the plateau is not visible and end capacitance assumption is applied.

Figure 4.4.2: Two different modes of extracting the saturation voltage from CV measurement from the DI SR campaign for two diodes annealed at a temperature of 60 $^{\circ}\text{C}$ for 40 min.

4.5 Annealing

To study annealing effects, the diodes are exposed to different temperatures, 20.5 $^{\circ}\text{C}$, 40 $^{\circ}\text{C}$, and 60 $^{\circ}\text{C}$. These annealing steps are performed in an oven located in the laboratory, as shown in Figure 4.5.1. The diodes, mounted on PCBs, are placed on preheated copper blocks in the oven at the target temperature for a specified time. During annealing, the PCB temperature is recorded every second using a PT1000 temperature sensor. Since the PT1000 is not placed directly on the diode, small temperature deviations may exist between the recorded and the actual diode temperatures.

The measured temperature is converted to an equivalent annealing time at the target temperature for FZ (300 μm and 200 μm) and EPI (120 μm) diodes using Arrhenius equation

$$t_{eq} = t(T) \exp \left[-\frac{E_a}{k_B} \left(\frac{1}{T} - \frac{1}{T_{target}} \right) \right], \quad (4.5.1)$$

where $t(T)$ is the time spent at temperature T , t_{eq} the equivalent annealing time at the target temperature, and E_a the activation energy of annealing. Values of $E_a = 1.1$ and 1.01 are used for FZ and EPI diodes, respectively [21].

Figure 4.5.2 shows the measured PT1000 temperature together with the setpoint of the oven. The figure illustrates the need for Arrhenius scaling, as the diode does not instantaneously reach or remain at the target temperature. After annealing, the PCBs are placed on cooling plates to prevent condensation on the diodes once they are placed back into the freezer.



Figure 4.5.1: Diodes on PCBs placed on preheated copper blocks in the oven. Temperature is recorded every second using a PT1000.

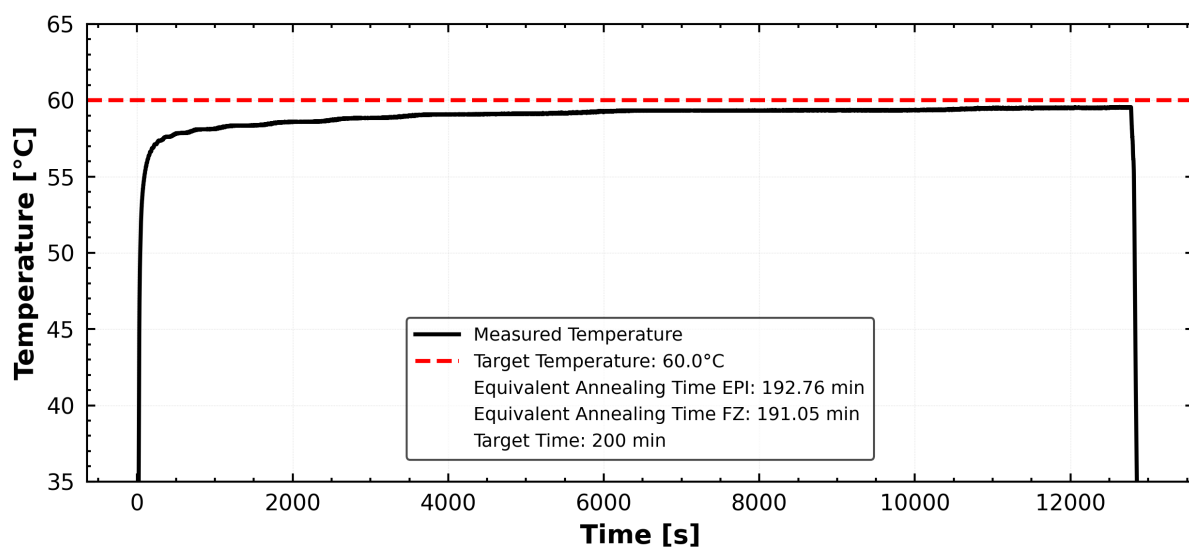


Figure 4.5.2: Measured temperature from the PT1000 in black solid line. Target temperature, which is the set temperature of the oven, is shown in red dashed line. The equivalent annealing time converted to the target temperature for EPI and FZ diodes are calculated using Equation (4.5.1).

4.6 Uncertainties

As all data in this thesis are obtained from experimental measurements, they are related to uncertainties that must be estimated. During irradiation in the TRIGA nuclear reactor, a 10 % fluence deviation was observed in a study from the facility and is therefore assigned as the uncertainty for all diodes. For all measurements, both in the IVCV probe station and in the IVCV & TCT setup, a temperature uncertainty of $\pm 1^\circ\text{C}$ is assigned, since the temperature is not measured directly on the diode. This uncertainty was observed in [31] by comparing the diode temperature to the PT1000 on the PCB using an infrared camera. Consequently, the current is scaled to -21°C and -19°C . According to the technical specification of the wafer production, all diodes exhibit a thickness variation of $10 \mu\text{m}$.

The charge collection is affected by several factors. Similar to leakage current, it is temperature-dependent, both due to photon absorption in the silicon diode and to variations in the laser intensity. The laser intensity changes with the temperature inside the Faraday cage and in the laboratory. As described in §4.3.2, a $300 \mu\text{m}$ reference diode is measured at the end of each day and used as a correction factor for all other measurements. Since the laser intensity vary during the day, this reference correction might not be entirely accurate for all measurements during the day. Because individual temperature-dependent effects are difficult to isolate, a fixed 5 % uncertainty is assigned to charge collection, based on observed laser intensity and temperature variations throughout the day.

During annealing in the oven, a 5 % uncertainty is assigned for the calculated annealing time based on the temperature logging. The value arises from that the PT1000 does not measure the diode temperature directly and because temperature variations are observed within the oven, depending on the copper block spacing. In addition, the temperature is recorded on only one of the PCBs. In rare cases when the logger malfunctions, a 10 % uncertainty is applied. Oven temperature can vary depending on when the diodes are inserted, which causes the annealing time to deviate slightly if the diodes are inserted two hours compared to three hours after the target temperature appears reached. This variability motivates the use of a 10 % uncertainty in the absence of temperature logging. This value corresponds to twice the uncertainty assigned when the temperature is recorded, ensuring that the uncertainty covers the actual annealing time.

For two independent uncertainties, assuming Gaussian distributions, the standard deviation of a sum is given by Gaussian error propagation as

$$\sigma = \sqrt{\sigma_A^2 + \sigma_B^2}, \quad (4.6.1)$$

For a ratio, the standard deviation is given by

$$\sigma = |f| \sqrt{\frac{\sigma_A^2}{A} + \frac{\sigma_B^2}{B}}, \quad (4.6.2)$$

where $f = \frac{A}{B}$.

CHAPTER 5

RESULTS AND DISCUSSION

In this section, a comparison between the HF and DI SR campaigns is presented. The charge collection efficiency results are discussed in §5.1, followed by the saturation voltage and effective doping concentration in §5.2. The leakage current damage rate α is presented in §5.3. Each section first presents the electrical characteristic as a function of fluence to analyse the radiation hardness for each diode thickness of 300 μm , 200 μm , and 120 μm . The electrical characteristics are then studied as a function of annealing time to investigate their dependence on annealing and observe potential differences in values and annealing time optima between the HF and DI SR campaigns.

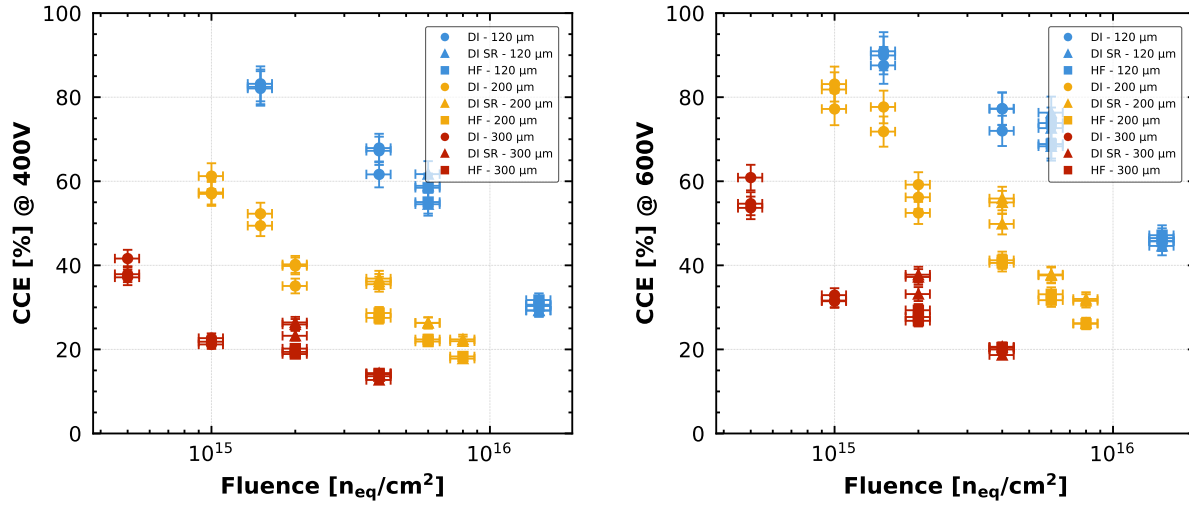
The considered operating voltages for the HGCAL silicon sensors are 400 V, 600 V, and 800 V. The leakage current damage rate is shown in detail at 400 V to reduce the risk of including charge multiplication and runaway leakage current present at higher voltages. Charge multiplication is a phenomenon that occurs after radiation damage, as high electric fields near the electrodes cause charge carriers to generate additional electron-hole pairs within the lattice. Comparing α values between DI SR and HF diodes at higher voltages may introduce inaccuracies, as some defects anneal during the in between annealing. Variations in defect density may modify the local electric field within the diode, affecting comparison results at higher voltages, while these effects are significantly reduced at lower voltages.

Charge collection efficiency is shown in detail at 600 V. The compressed average ratio plots, similar to Figure 5.1.6, at 400 V and 800 V are shown in §A.3, showing no significant difference in the CCE DI SR/HF ratio across voltages. During operation, particles traversing the sensors are measured through charge collection, and it is therefore of interest to analyse all considered operating voltages, even in the presence of phenomena such as charge multiplication.

5.1 Charge Collection Efficiency

The charge collection efficiency calculated using Equation (3.2.3) as a function of fluence is shown in Figure 5.1.1 for diodes with thicknesses of 300 μm , 200 μm , and 120 μm . The 300 μm diodes exhibit the lowest CCE at a given fluence, while the 120 μm diodes show the highest CCE. Three effects explain this thickness dependence. First, thicker diodes, in particular the DI SR and HF diodes, are not fully depleted at a reverse voltage bias of 600 V, increasing the probability that electrons generated by traversing ionising particles recombine before reaching the electrodes. Second, as discussed in §3.2.3, the effective carrier lifetime decreases with increasing fluence due to trapping. Third, thinner diodes exhibit stronger electric fields, leading to higher carrier drift velocities. As a result, electrons in thinner diodes have a higher probability of reaching the electrodes before being trapped.

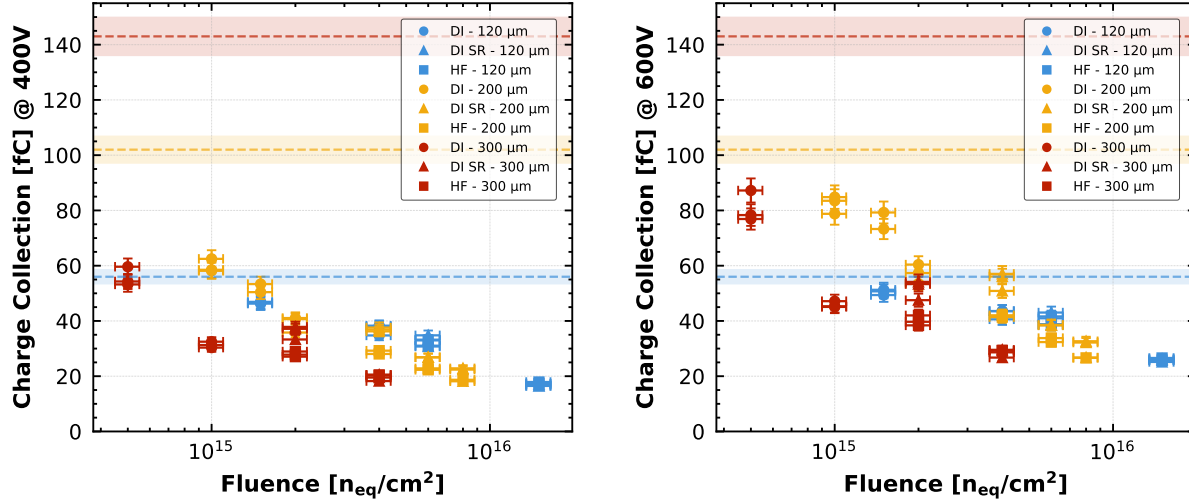
A comparison of Figures 5.1.1a and 5.1.1b shows that increasing the reverse voltage bias increases the CCE for all diodes. A higher voltage widens the depletion region and increases the internal electric field, thereby increasing the carrier drift velocity and reducing the probability of recombination or trapping. As a result, the CCE increases.



(a) Charge collection efficiency measured with an applied reverse voltage bias of 400 V.

(b) Charge collection efficiency measured with an applied reverse voltage bias of 600 V.

Figure 5.1.1: Charge collection efficiency as a function of fluence for all diodes in all campaigns with no additional annealing except for in-reactor annealing. The colours and markers represent different thicknesses and campaigns.



(a) Charge collection measured at 400 V.

(b) Charge collection measured at 600 V.

Figure 5.1.2: Charge collection as a function of fluence with similar diodes and annealing time as in Figure 5.1.1. Dashed lines indicate the charge collection for each thickness for unirradiated diodes.

To study the radiation hardness and annealing effects, the CCE is analysed as a function of annealing time at different temperatures. Figures 5.1.3, 5.1.4, and 5.1.5 show the

CCE at 600 V for annealing temperatures of 20.5 °C, 40 °C, and 60 °C. The right side of each figure contains diodes from the Double Irradiated Second Round and High Fluence campaigns exposed to fluences corresponding to the end of the HL-LHC, while the left side shows diodes from the Double Irradiated campaign exposed to one quarter of these fluences. Lower fluences and thicker diodes are shown in the upper figures, followed by higher fluences and thinner diodes in the middle, and the bottom figure shows the ratio DI SR / HF for all fluences.

As the annealing times differ slightly between the DI SR and HF campaigns, the ratio is calculated using the measured DI SR value divided by a value interpolated between the nearest HF points at the corresponding annealing time. Values above one, shown in green, indicate a beneficial effect from the in between annealing, as the DI SR diodes have a higher CCE than the HF diodes. Analysing all ratio plots in Figures 5.1.3, 5.1.4, and 5.1.5, most DI SR diodes across all temperatures have a higher or equal CCE than the HF diodes, except for the 300 µm diodes irradiated to $4 \cdot 10^{15} n_{eq}/cm^2$.

The annealing time optima, defined as the point at which the CCE maximum begins to decrease with increasing annealing time, are similar between the DI SR and HF campaigns for all diodes at 20.5 °C and 40 °C. At 60 °C, the optima are shifted to earlier annealing times for diodes exposed to fluences equal to or below $4 \cdot 10^{15} n_{eq}/cm^2$. This indicates that the in between annealing has little effect on the CCE annealing time optima at lower temperatures, but has a measurable effect at higher annealing temperatures.

To compress the data across all temperatures, the average ratio DI SR / HF for all annealing times is calculated for each diode and is shown in Figure 5.1.6. The results show a clear dependence on both fluence and thickness. The 300 µm diodes irradiated to $2 \cdot 10^{15} n_{eq}/cm^2$ show a strong beneficial effect of approximately 25 % from the in between annealing, while this effect becomes negative at $4 \cdot 10^{15} n_{eq}/cm^2$. For 200 µm diodes, the in between annealing is beneficial across the full fluence range, with slower reduction compared to the 300 µm diodes. For 120 µm diodes, no significant effect from the in between annealing is observed, as the ratio remains close to one and the variation between $6 \cdot 10^{15} n_{eq}/cm^2$ and $1.5 \cdot 10^{16} n_{eq}/cm^2$ is small.

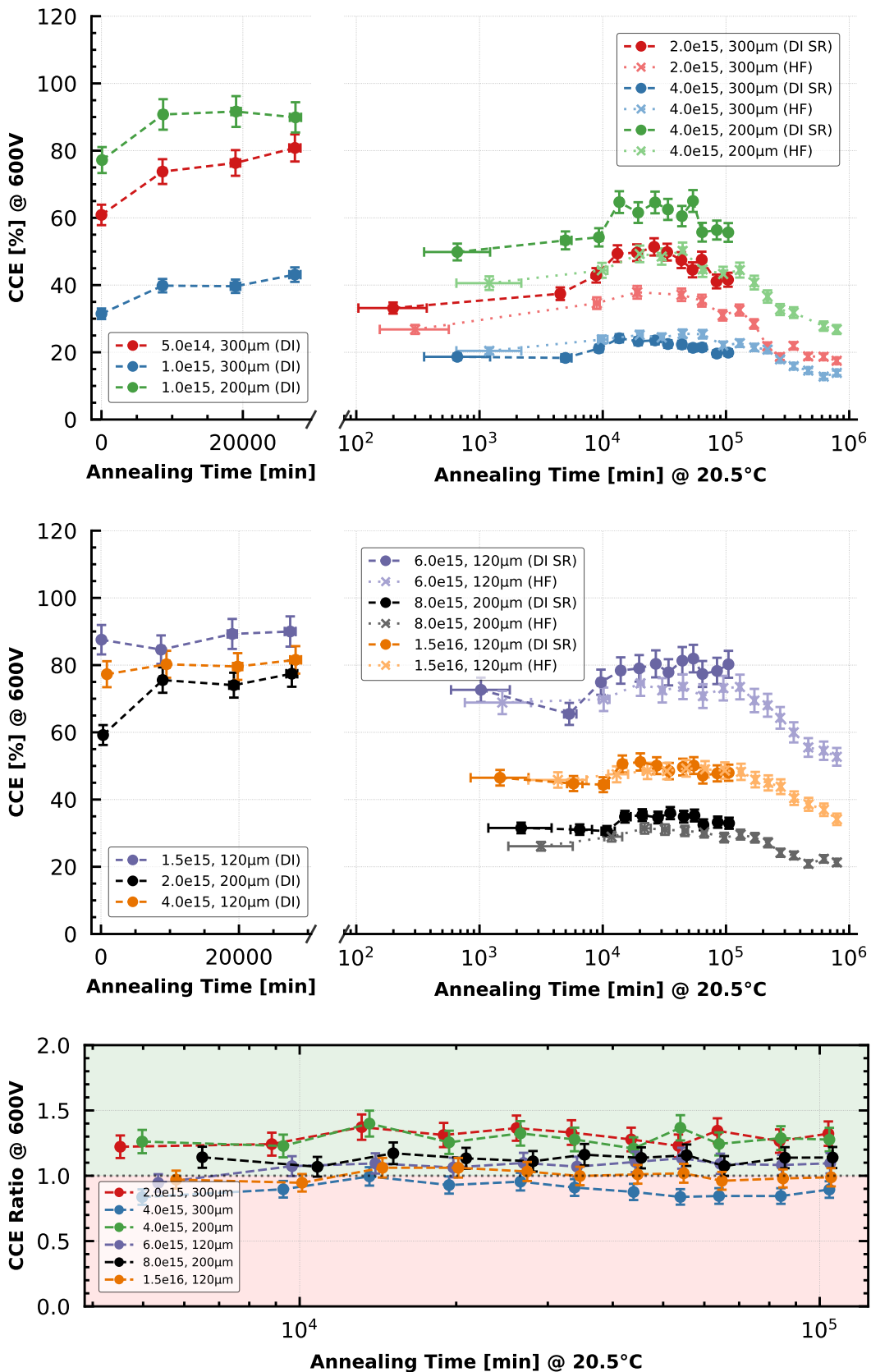


Figure 5.1.3: The two top plots show CCE as a function of annealing time from the DI campaign (left) and from the DI SR and HF campaigns (right), annealed at a temperature of 20.5 °C. The bottom plot shows the ratio DI SR/HF, where the green region indicates a beneficial effect of the in between annealing.

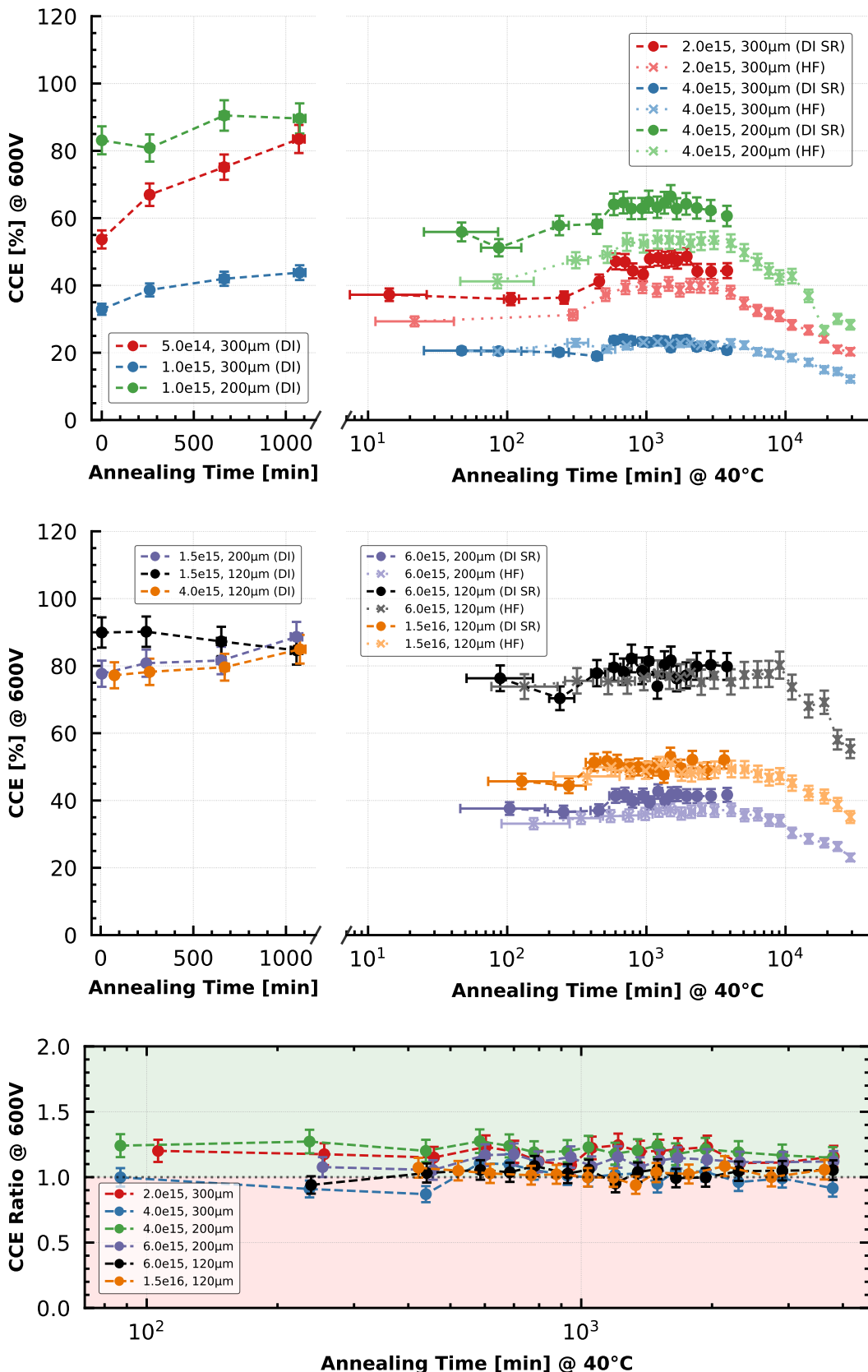


Figure 5.1.4: The two top plots show CCE as a function of annealing time from the DI campaign (left) and from the DI SR and HF campaigns (right), annealed at a temperature of 40 °C. The bottom plot shows the ratio DI SR/HF, where the green region indicates a beneficial effect of the in between annealing.

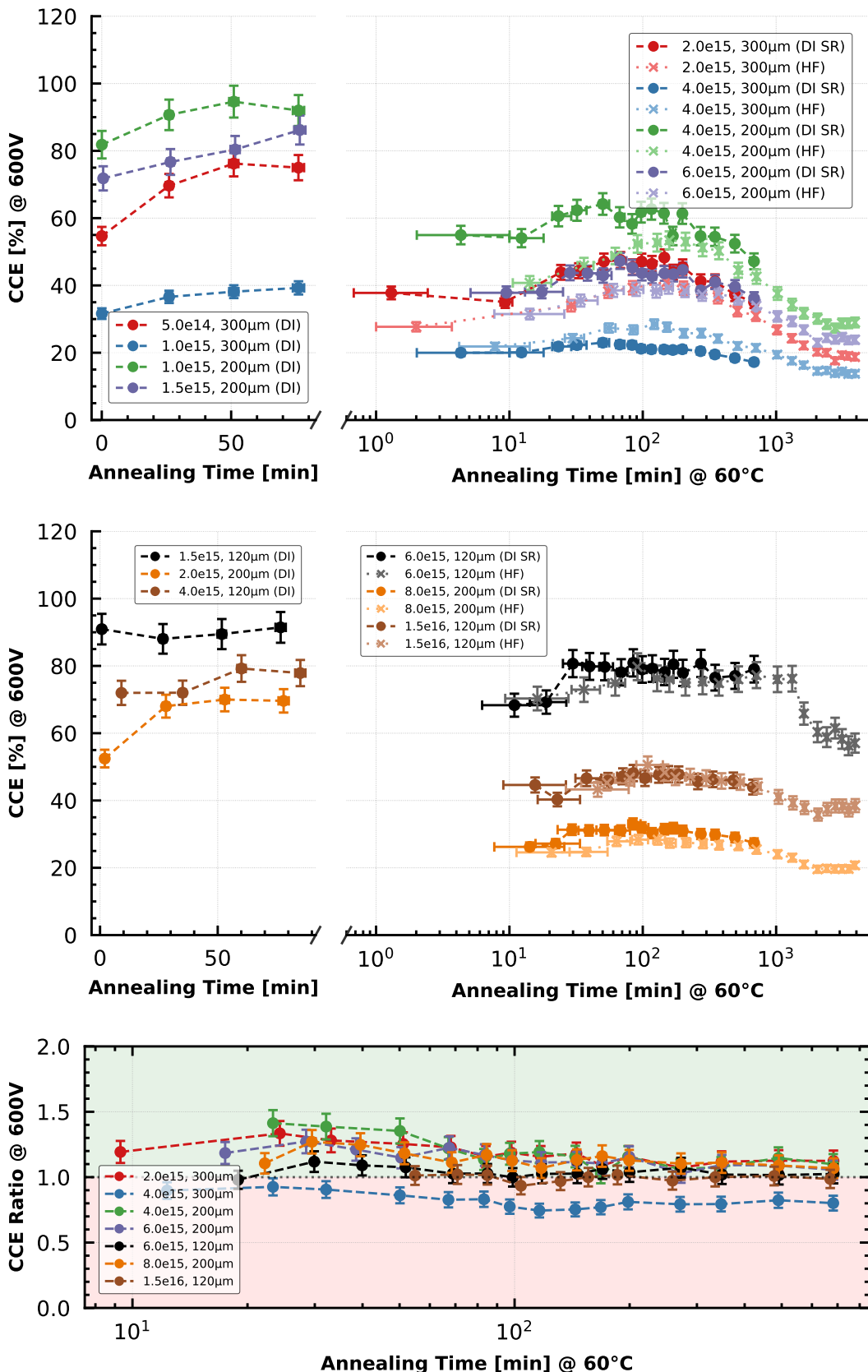


Figure 5.1.5: The two top plots show CCE as a function of annealing time from the DI campaign (left) and from the DI SR and HF campaigns (right), annealed at a temperature of 60 °C. The bottom plot shows the ratio DI SR/HF, where the green region indicates a beneficial effect of the in between annealing.

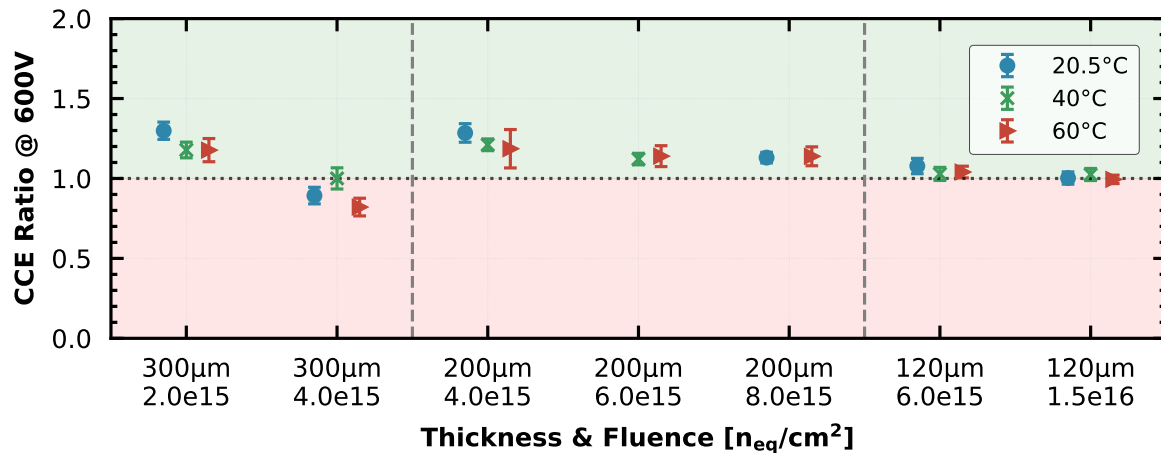


Figure 5.1.6: The average DI SR/HF ratio of the charge collection efficiency, calculated over all annealing times for each unique combination of annealing temperature, thickness, and fluence.

5.2 Saturation Voltage

The saturation voltage is analysed using the same approach as for the CCE. The method used to extract the saturation from both CV and TCT data is described in §4.4.1. For the comparison between the DI SR and HF campaigns, saturation voltages are extracted from CV measurements, as these data are smoother and contain more points than TCT measurements, providing more precise and consistent values. The saturation voltage extracted from CV data is frequency dependent, whereas the values extracted from TCT are closer to the true saturation voltage.

Figure 5.2.1 shows the saturation voltage extracted from CV and TCT data for diodes with thicknesses of 200 μm and 120 μm, irradiated to fluences of $4 \cdot 10^{15}$ and $6 \cdot 10^{15}$ n_{eq}/cm² and annealed at 20.5°C. These are the only diodes for which the saturation voltage could be extracted from TCT data at this annealing temperature. The saturation voltage extracted from TCT data is slightly higher than that extracted from CV data. This behaviour is observed consistently at all annealing temperatures.

Figure 5.2.2 shows the saturation voltage extracted from CV data at 2 kHz as a function of fluence for diodes annealed for 90 min at 60°C across all campaigns. Thinner diodes exhibit lower saturation voltages at a given fluence compared to thicker diodes. As discussed in §2.4.3 and §3.2.2, radiation damage introduces additional donor and acceptor levels in the band gap, which modifies the effective doping concentration N_{eff}, which also changes the saturation voltage based on Equation (2.4.3). As the saturation voltage is proportional to N_{eff} · D², where D is the diode thickness, thicker diodes require a higher voltage to reach full depletion. As observed in Figure 5.2.2, the saturation voltage for thicker diodes increases faster with fluence compared to thinner diodes. Note that the x-axis is in logarithmic scale.

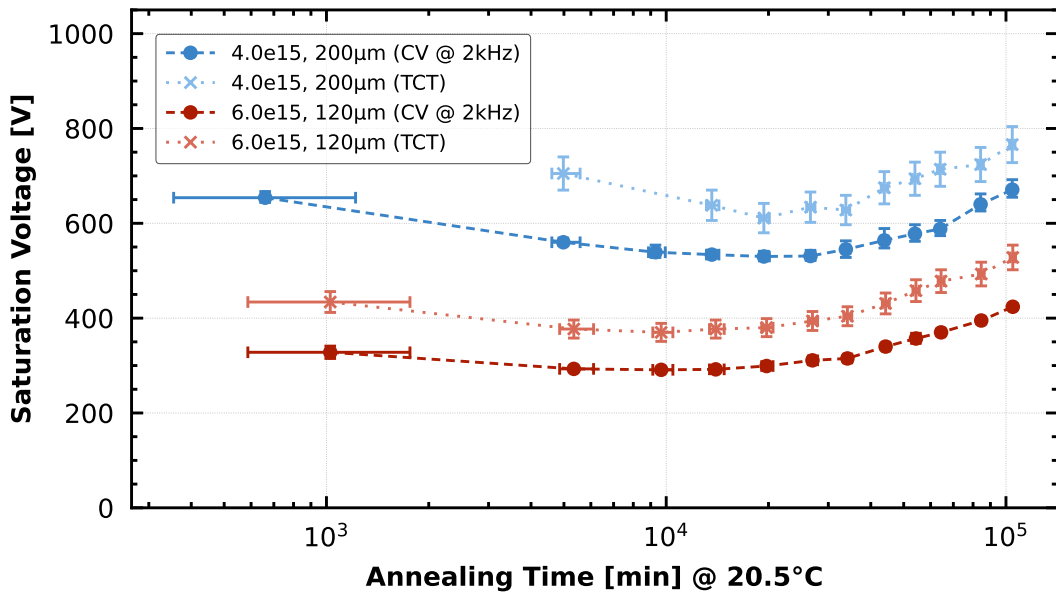


Figure 5.2.1: Saturation voltage extracted from CV at 2 kHz and TCT measurements as a function of annealing time for diodes annealed at 20.5 °C from the DI SR campaign, with thicknesses of 200 μm and 120 μm , and fluences of $4 \cdot 10^{15}$ and $6 \cdot 10^{15} \text{n}_{\text{eq}}/\text{cm}^2$.

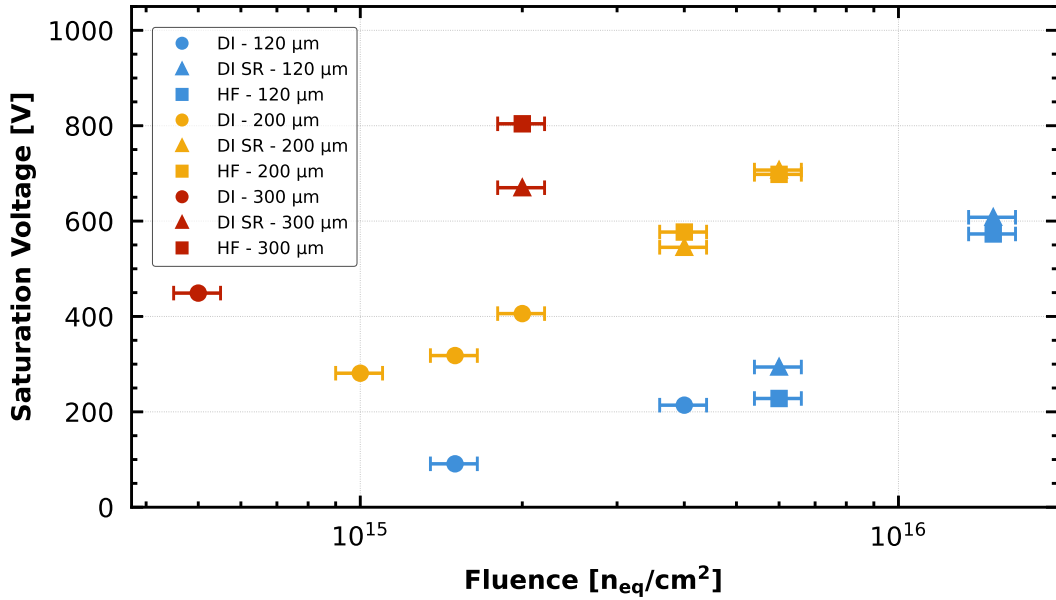


Figure 5.2.2: Saturation voltage extracted from CV measurements at 2 kHz as a function of fluence for all diodes annealed for 90 min at 60 °C across all campaigns. Red, yellow, and blue denote diodes with thicknesses of 300 μm , 200 μm , and 120 μm .

Figures 5.2.3, 5.2.4, and 5.2.5 show the saturation voltage as a function of annealing time. Comparing the left-hand plots, corresponding to the DI campaign, with the DI SR and HF campaigns shows that the initial annealing effect is stronger for diodes exposed to one quarter of the final fluence. A comparison between the individual diodes in the DI SR and HF campaigns across all temperatures shows that the in between annealing is more

beneficial at lower fluences, while the effect becomes comparable or worse at fluences equal to or above $8 \cdot 10^{15} \text{ n}_{\text{eq}}/\text{cm}^2$.

To compress the data across all temperatures, the ratio plots are averaged and shown in Figure 5.2.6. Similar thickness and fluence dependencies observed for the CCE are also present for the saturation voltage, with thicker diodes at lower fluences show a stronger beneficial effect from the in between annealing. A deviation is observed for the diode annealed at 60 °C with a thickness of 120 µm and a fluence of $6 \cdot 10^{15} \text{ n}_{\text{eq}}/\text{cm}^2$, where the DI SR diode has a significantly higher saturation voltage than the corresponding HF diode. The HF diode is observed to have a lower saturation voltage than the corresponding HF diodes annealed at 20.5 °C and 40 °C and is therefore classified as an outlier.

Annealing time optima are observed earlier in the DI SR campaign compared to the HF campaign. The DI SR annealing times do not include the annealing time from the initial DI campaign, which can explain the observed shift.

Figure 5.2.7 shows the saturation voltage for diodes annealed at a temperature of 40 °C, where the DI SR annealing times are shifted by one quarter of the maximum annealing time of the DI campaign, corresponding to one quarter of the final fluence. With this shift applied, the annealing time optima of the DI SR and HF campaigns become more aligned. The microscopic behaviour of point and cluster defects, and their response to in between annealing and multiple rounds of irradiation, is not yet fully understood of today. Therefore, it is difficult to conclude whether one quarter of the DI annealing should propagate to the DI SR annealing time, or whether a shorter or longer time would be more appropriate.

During the HL-LHC phase, the HGCAL silicon sensors are not expected to be annealed into the reverse annealing region. With or without applying any annealing shift to the DI SR campaign, the saturation voltages before the optima are lower or equal for the DI SR campaign compared to the HF campaign for all diodes up to fluences of $6 \cdot 10^{15} \text{ n}_{\text{eq}}/\text{cm}^2$.

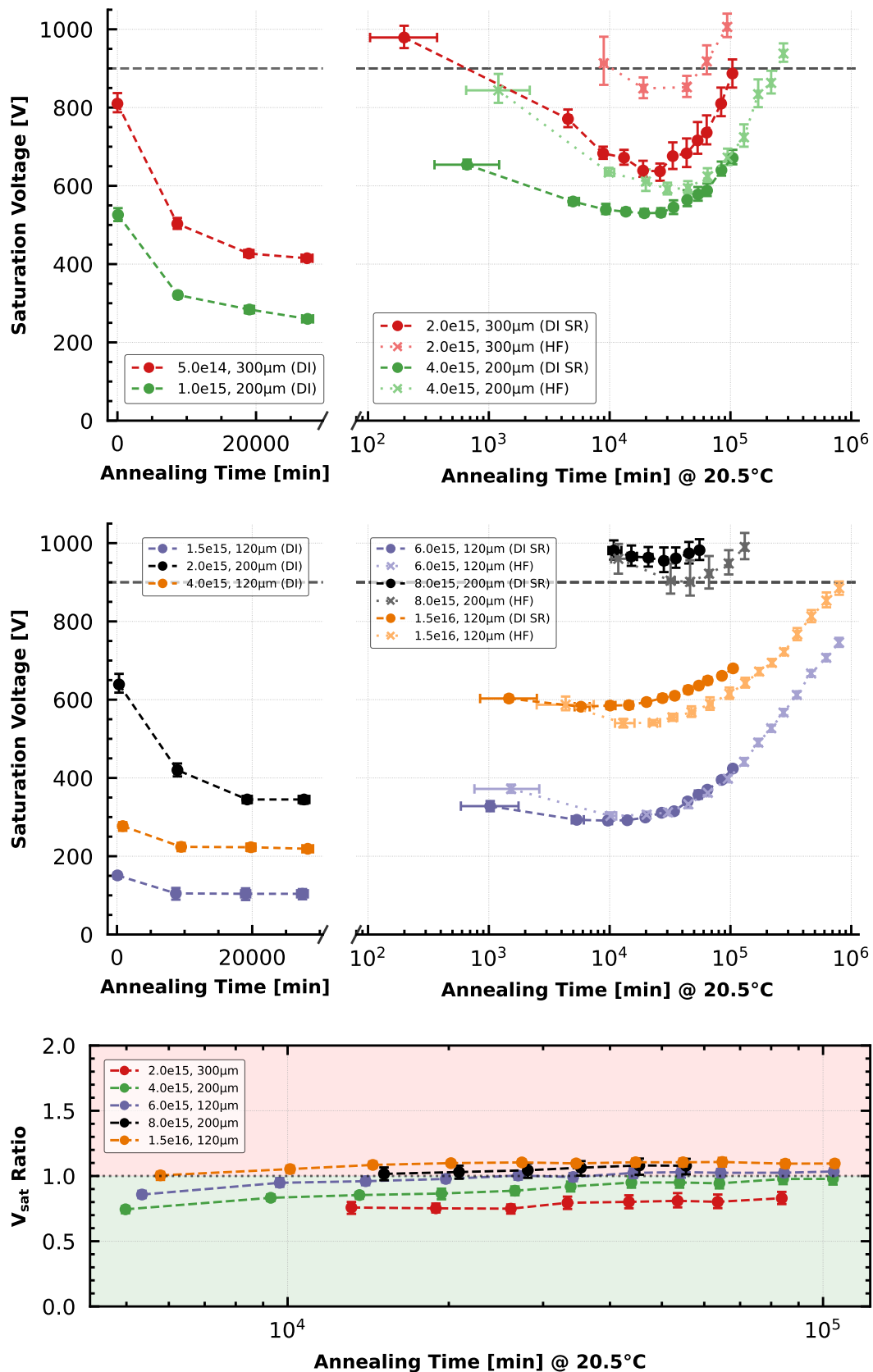


Figure 5.2.3: The two top plots show saturation voltage as a function of annealing time from the DI campaign (left) limit and from the DI SR and HF campaigns (right), annealed at 20.5 °C. The grey dashed line is the measurement limit. Bottom plot shows the ratio DI SR/HF, where the green region indicates a beneficial effect of the in between annealing.

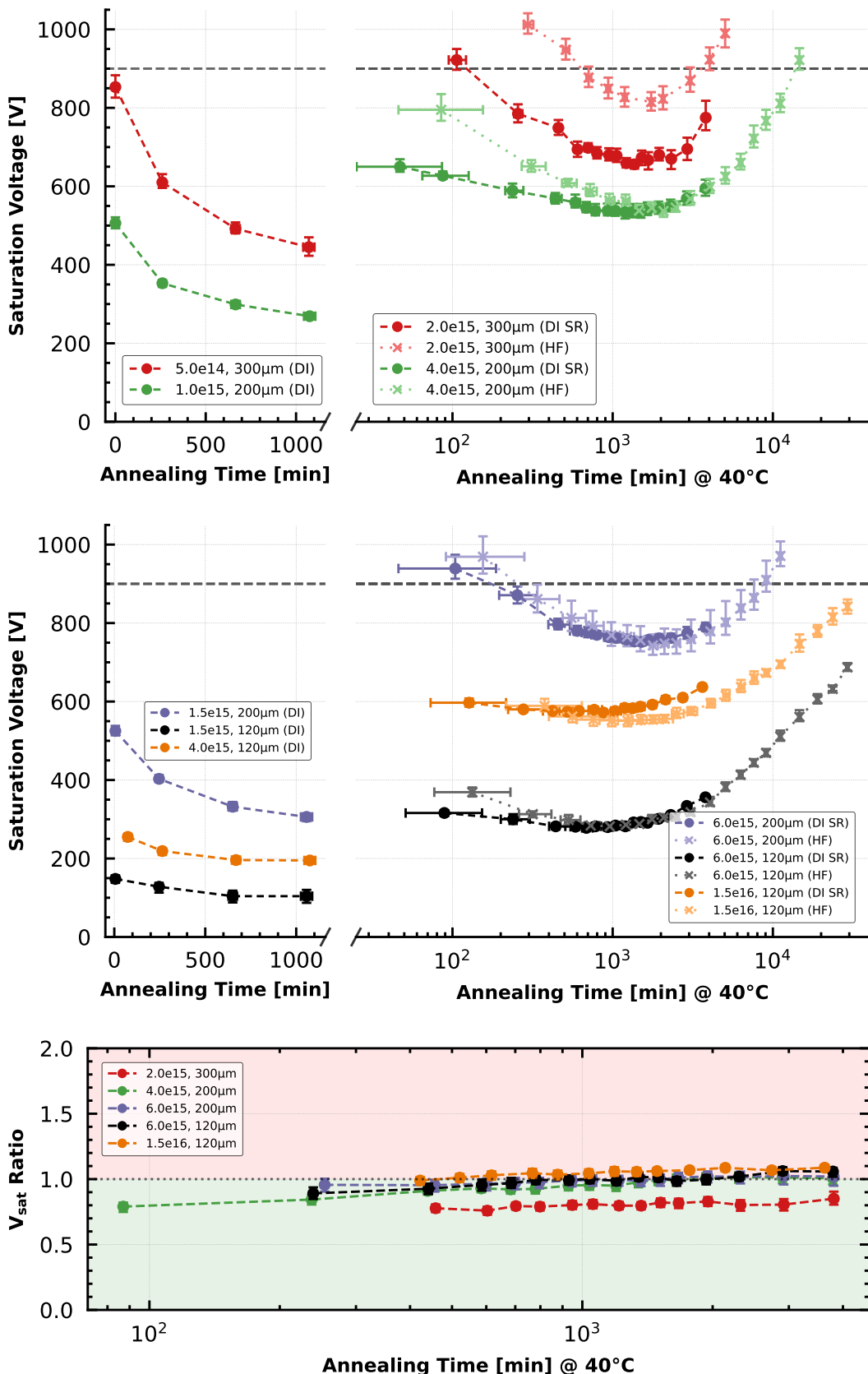


Figure 5.2.4: The two top plots show saturation voltage as a function of annealing time from the DI campaign (left) and from the DI SR and HF campaigns (right), annealed at 40 °C. The grey dashed line is the measurement limit. Bottom plot shows the ratio DI SR/HF, where the green region indicates a beneficial effect of the in between annealing.

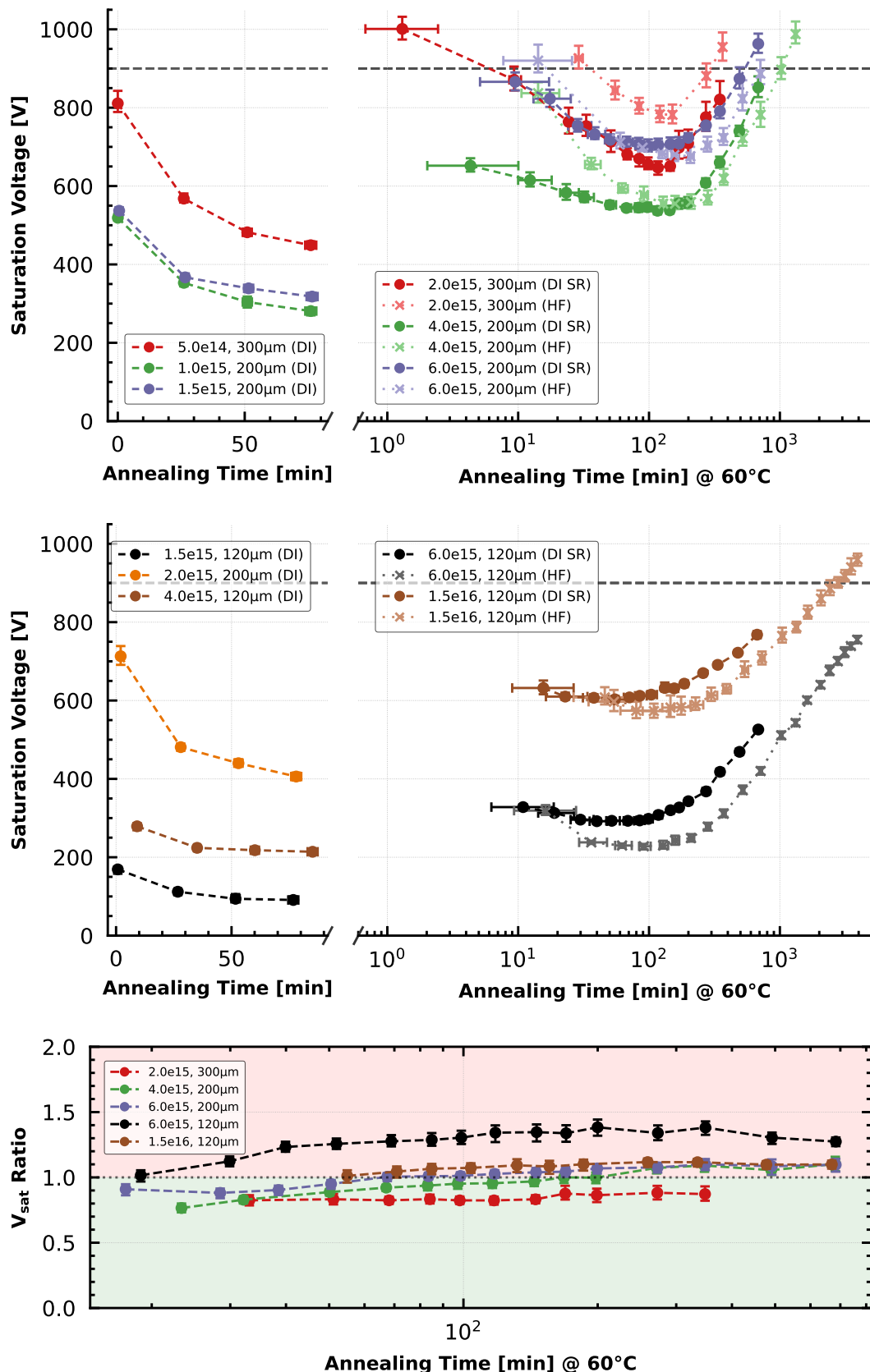


Figure 5.2.5: The two top plots show saturation voltage as a function of annealing time from the DI campaign (left) and from the DI SR and HF campaigns (right), annealed at 60 °C. The grey dashed line is the measurement limit. Bottom plot shows the ratio DI SR/HF, where the green region indicates a beneficial effect of the in between annealing.

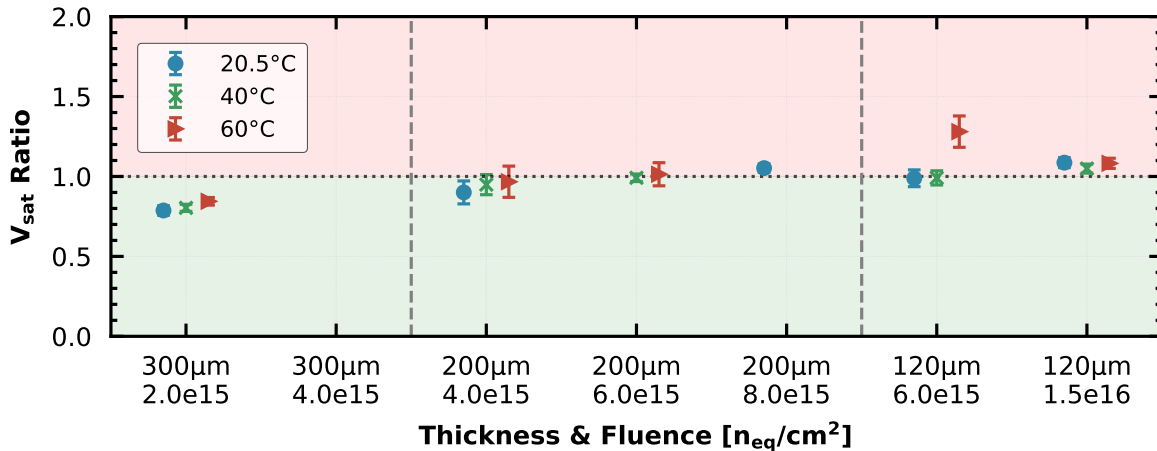


Figure 5.2.6: The average DI SR/HF ratio of the saturation voltage, calculated over all annealing times for each unique combination of annealing temperature, thickness, and fluence.

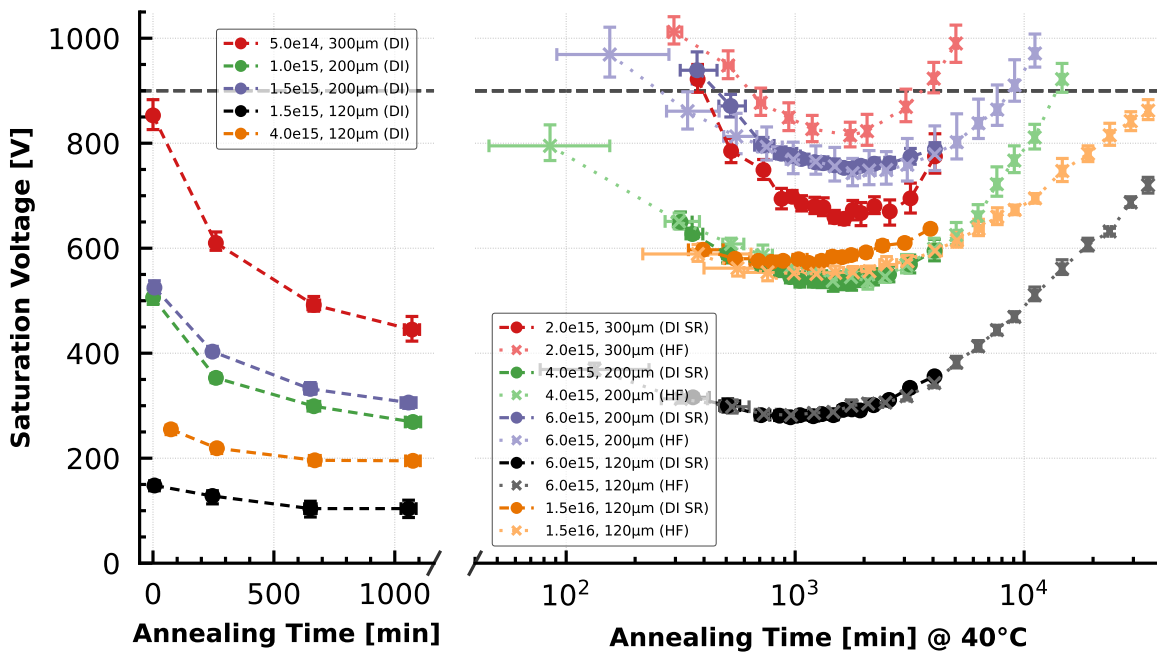


Figure 5.2.7: Saturation voltage as a function of annealing time for diodes annealed at a temperature of 40 °C. For diodes from the DI SR campaign, an additional one quarter of the maximum annealing time from the DI campaign is added to each data point.

5.3 Leakage Current

Before analysing the leakage current damage rate α at a fixed voltage, it is essential to consider its dependence on the applied reverse voltage bias. The analysis is performed at 400 V, one of the planned HGCAL operating voltages. All α values presented in this section are normalised to 20 °C using Arrhenius scaling. As shown in Figure 3.2.2a, α is expected to be constant at a given annealing time and temperature, independent of

fluence. This holds if the leakage current is measured at or above the saturation voltage, where the current is approximately flat. For irradiated diodes, as observed in Figure 4.4.1a, the leakage current was found to continue to increase with voltages above the saturation voltage. Measuring leakage current above the saturation voltage therefore leads to an overestimation of α . In contrast, voltages below the saturation voltage underestimate α because the full active volume is not depleted.

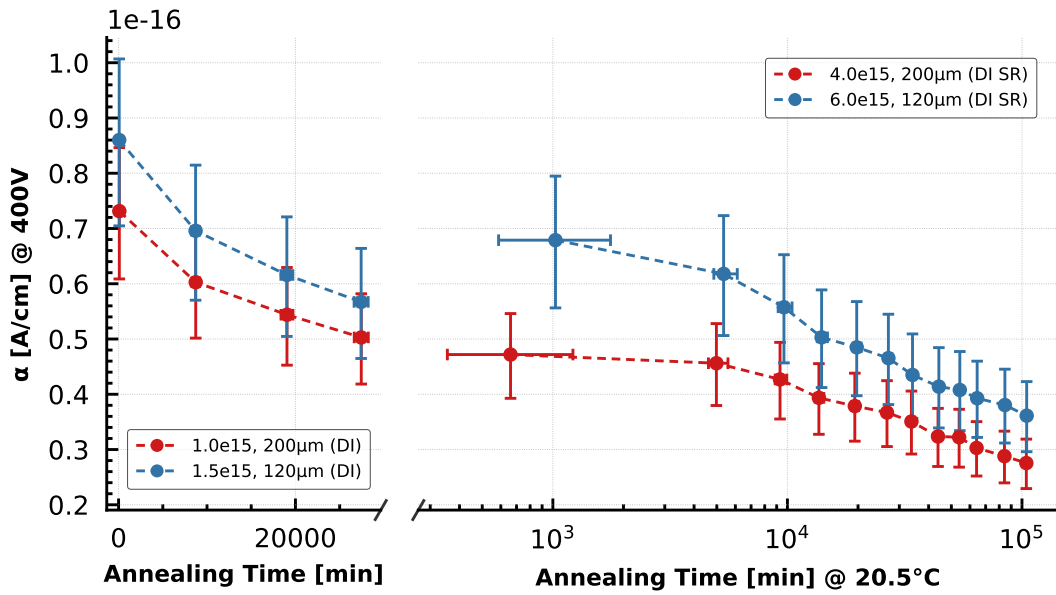


Figure 5.3.1: Leakage current damage rate α as function of annealing time. The left part shows α for DI campaign diodes annealed at 20.5 °C, with thicknesses of 200 μm and 120 μm and fluences of $1 \cdot 10^{15}$ and $1.5 \cdot 10^{15}$ $\text{n}_{\text{eq}}/\text{cm}^2$. The right part shows the same diodes exposed to higher fluence of $4 \cdot 10^{15}$ and $6 \cdot 10^{15}$ $\text{n}_{\text{eq}}/\text{cm}^2$.

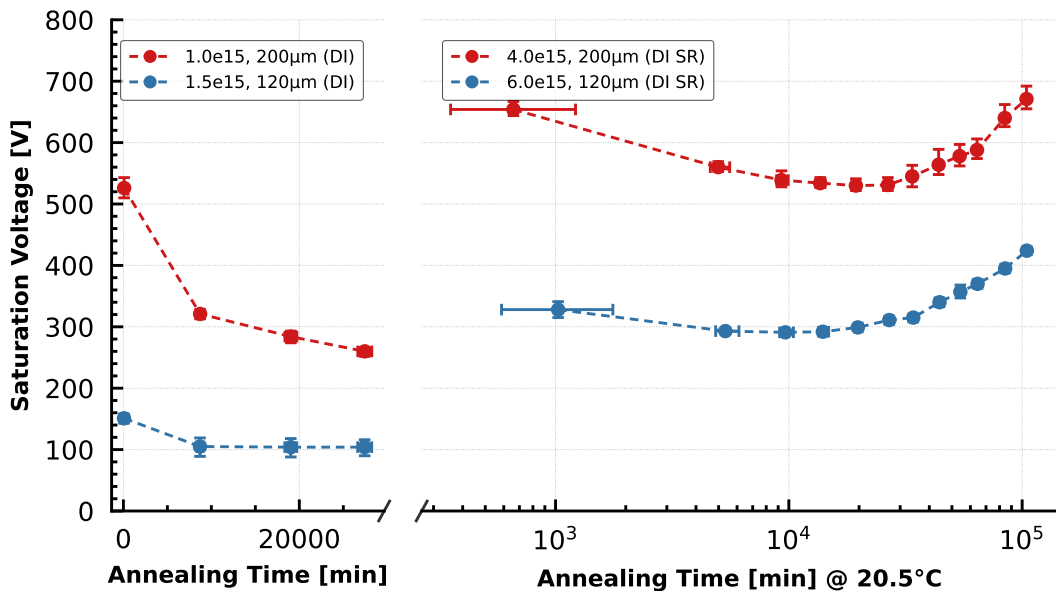


Figure 5.3.2: Saturation voltage as a function of annealing time for the same DI and DI SR diode shown in Figure 5.3.1, annealed at a temperature of 20.5 °C.

Figure 5.3.1 illustrates this effect for DI and DI SR campaigns, showing α as a function of annealing time with the corresponding saturation voltage in Figure 5.3.2. Diodes in the DI campaign, exposed to lower fluences, generally show higher α values. Comparing the last DI point for the $200\text{ }\mu\text{m}$ diode irradiated to $1 \cdot 10^{15} \text{ n}_{\text{eq}}/\text{cm}^2$ with the first DI SR point irradiated to $4 \cdot 10^{15} \text{ n}_{\text{eq}}/\text{cm}^2$, the DI value of α is higher because the diode is overdepleted, as the saturation voltage lies below 400 V. In contrast, the DI SR value of α is underestimated because the diode is underdepleted, as the saturation voltage lies above 400 V.

The optimum voltage for extracting the α values is the saturation voltage. The comparison between the DI SR and HF campaigns does not use the saturation voltage, as not all saturation voltages can be extracted. Figure 5.3.3 shows α using both a fixed voltage of 400 V and saturation voltage extracted from CV measurements at 2 kHz for diodes across all campaigns annealed for 30 min at 60°C . Using the saturation voltage reduces thickness-dependent variation and gives higher, more consistent α values between the data sets, as a more comparable fraction of the active volume contributes to the leakage current.

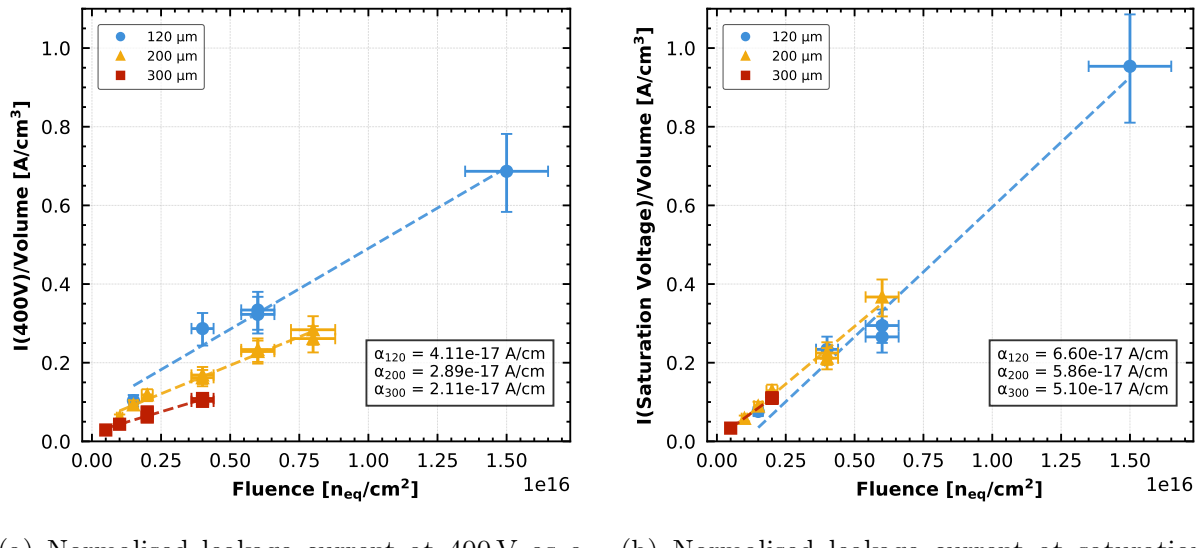


Figure 5.3.3: Leakage current normalised to the volume of the diode as a function of fluence for all diodes across all campaigns, annealed at a temperature of 60°C for 30 min. The leakage current damage rate α is extracted for each thickness, which equals the slope of the fitted lines.

With these observations taken into account, comparison of α values at 400 V between DI and DI SR are not relevant. As seen in §5.2, the saturation voltages between the DI SR and HF campaigns are similar, which makes the comparisons of α at a fixed voltage of 400 V valid between these two campaigns.

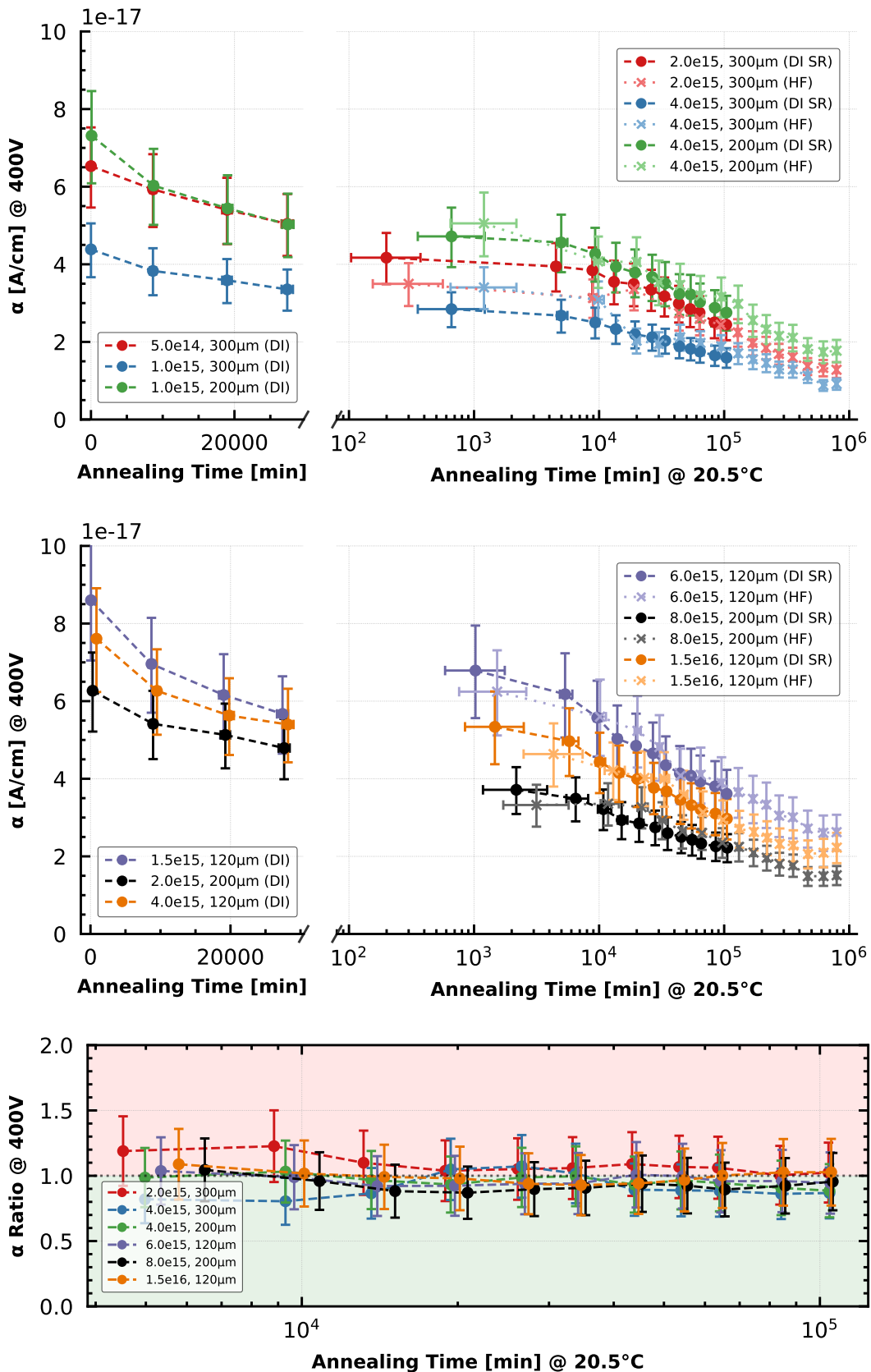


Figure 5.3.4: The two top plots show current related damage rate α as a function of annealing time from the DI campaign (left) and from the DI SR and HF campaigns (right), annealed at a temperature of 20.5 °C. The bottom plot shows the ratio DI SR/HF, where the green region indicates a beneficial effect of the in between annealing.

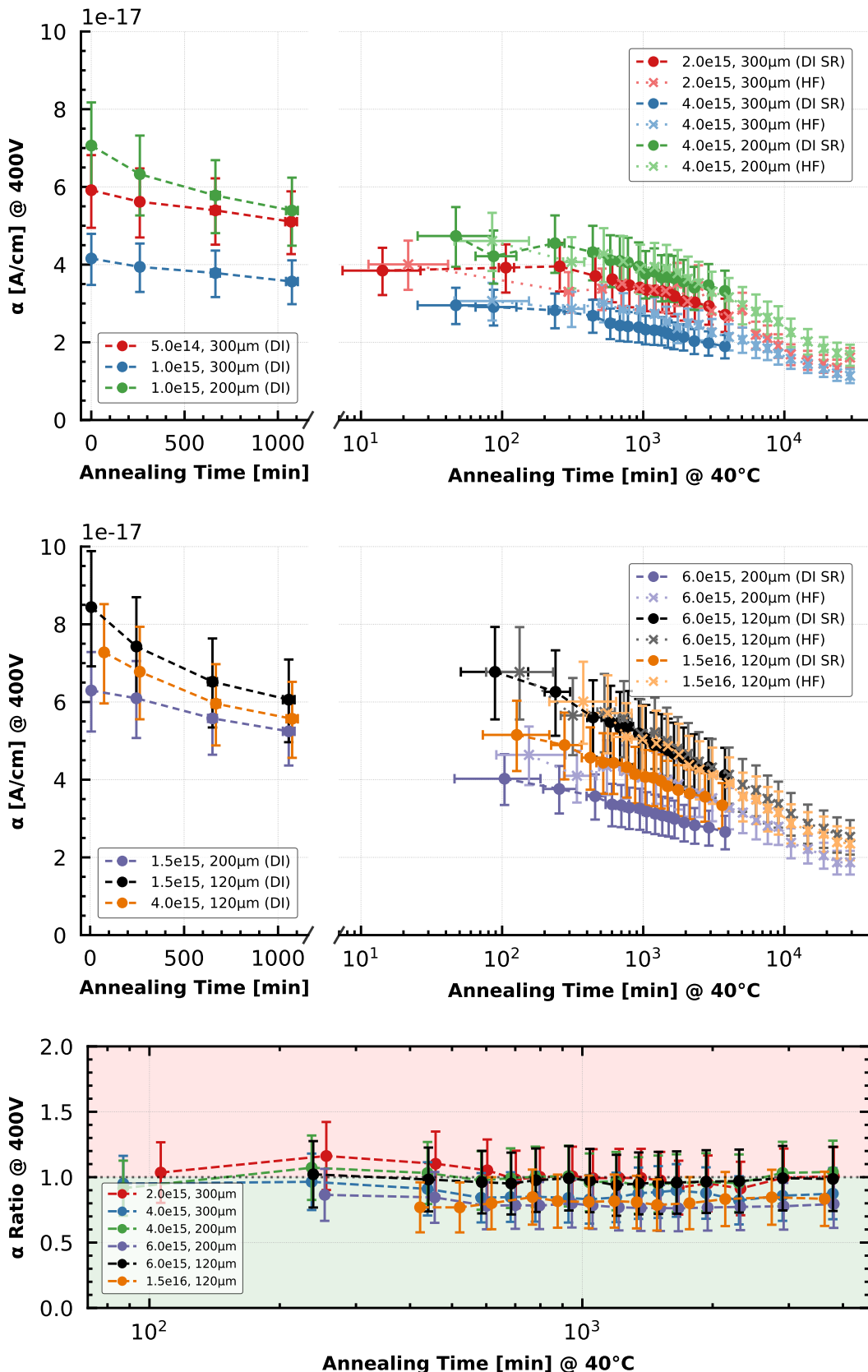


Figure 5.3.5: The two top plots show current related damage rate α as a function of annealing time from the DI campaign (left) and from the DI SR and HF campaigns (right), annealed at a temperature of 40 °C. The bottom plot shows the ratio DI SR/HF, where the green region indicates a beneficial effect of the in between annealing.

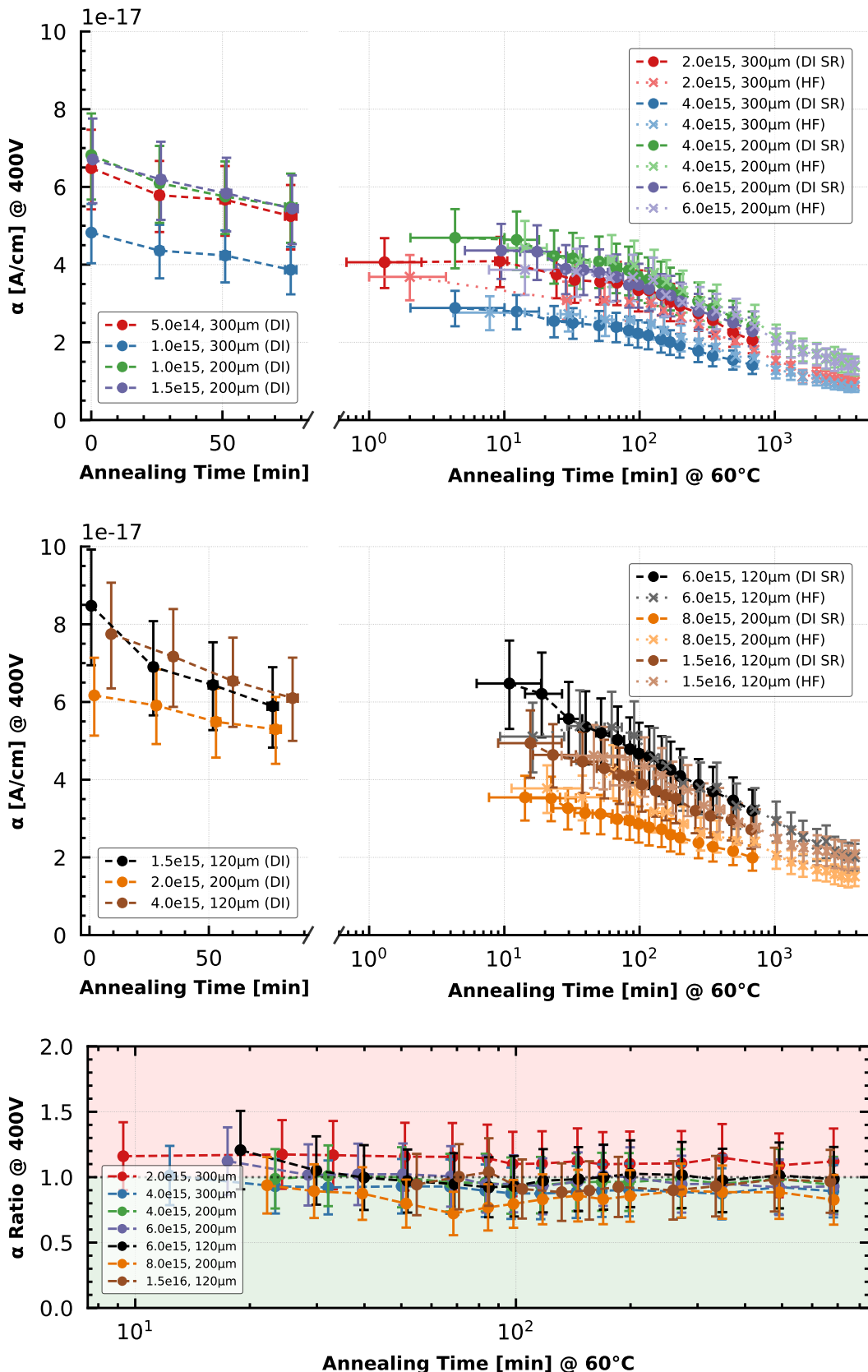


Figure 5.3.6: The two top plots show current related damage rate α as a function of annealing time from the DI campaign (left) and from the DI SR and HF campaigns (right), annealed at a temperature of 60 °C. The bottom plot shows the ratio DI SR/HF, where the green region indicates a beneficial effect of the in between annealing.

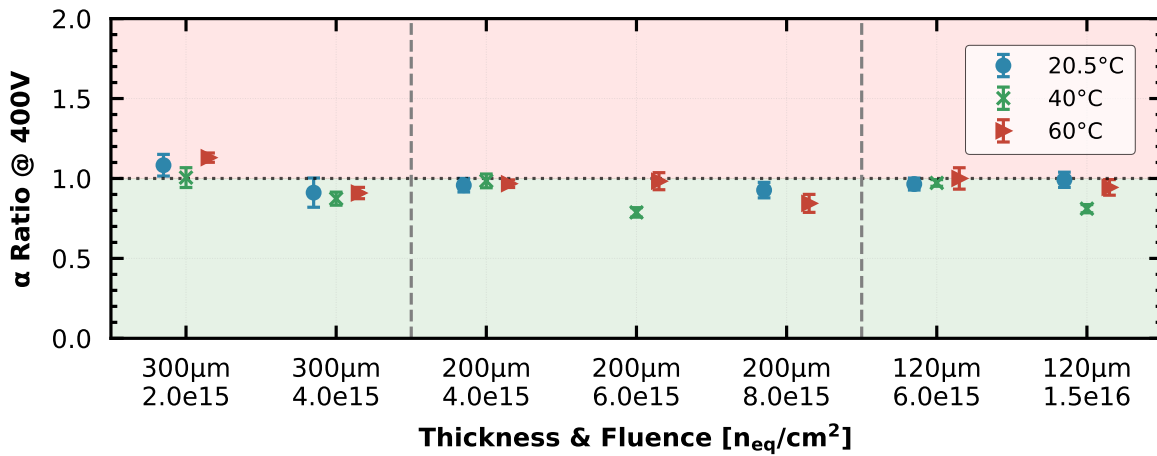


Figure 5.3.7: The average DI SR/HF ratio of the current related damage rate α , calculated over all annealing times for each unique combination of annealing temperature, thickness, and fluence.

As shown in Figure 5.3.7, most DI SR diodes have lower α values than HF diodes, resulting in ratios below one, which indicates a beneficial effect from in between annealing of the first quarter of the fluence. This behaviour is observed for all diodes except for the 300 μm diodes irradiated to a fluence of $2 \cdot 10^{15} \text{ n}_{\text{eq}}/\text{cm}^2$. As shown in Figure §5.2.6, these 300 μm DI SR diodes exhibit a 10 - 20 % lower saturation voltage than the corresponding HF diodes. At the same applied reverse voltage bias, a larger active volume is depleted in the DI SR diodes, which increases the leakage current and explains the higher observed α values compared to the HF diodes.

This chapter concludes the thesis by summarising the radiation hardness and annealing effects observed in the electrical characterisation analyses presented in §5. In §6.2, limitations of the study and ideas for future work are discussed.

6.1 Radiation Hardness and Annealing Effects of Electrical Characteristics

The goal of this thesis was to investigate the radiation hardness and annealing behaviour of silicon diodes for the CMS endcap calorimeter, HGCAL. The study aimed to mimic the HL-LHC timeline, including an in between annealing step representing Long Shutdown 4 between two main irradiations corresponding to Run 4 and Run 5. Charge collection efficiency, saturation voltage, and the leakage current damage rate were compared with the High Fluence campaign, in which diodes were irradiated to the expected HL-LHC end-of-life fluences in a single step, in order to investigate the effect of in between annealing.

The in between annealing effect on the charge collection efficiency is both thickness and fluence dependent. 300 µm diodes irradiated to $2 \cdot 10^{15} n_{eq}/cm^2$ and $4 \cdot 10^{15} n_{eq}/cm^2$ with in between annealing exhibit a CCE increase of 20 - 30 % and a decrease down to 20%, compared to HF diodes without in between annealing. For 200 µm diodes exposed to fluences from $4 \cdot 10^{15}$ to $8 \cdot 10^{15} n_{eq}/cm^2$, a beneficial effect from the in between annealing is observed with an increase of CCE by 10 - 30 %. For 120 µm diodes, no significant effect is observed.

Similar thickness and fluence dependencies are observed for the saturation voltage. Diodes with a thickness of 300 µm irradiated to $2 \cdot 10^{15} n_{eq}/cm^2$ show the strongest beneficial effect from the in between annealing with a saturation voltage decrease of 10 - 20 %. With decreasing thickness, this effect becomes weaker, and the saturation voltage ratio between the DI SR and HF campaigns approaches one.

The comparison of annealing time optima analysed from the CCE showed similar results between the DI SR and HF campaigns for all diodes annealed at 20.5 °C, 40 °C, and diodes exposed to fluences above $4 \cdot 10^{15} n_{eq}/cm^2$ at 60 °C. In contrast, earlier shifted annealing time optima for DI SR diodes compared to HF are observed from CCE for diodes exposed to fluences equal to or below $4 \cdot 10^{15} n_{eq}/cm^2$, and for all DI SR diodes observed from the saturation voltage.

There are no observed thickness and fluence dependencies of the leakage current damage rate. All diodes, except the 300 µm diodes irradiated to $2 \cdot 10^{15} n_{eq}/cm^2$, show a neutral or beneficial effect, with up to 20 % decrease in the current related damage rate due to in between annealing. The observed deviation for this specific thickness and fluence

combination is explained by the lower saturation voltage of the DI SR diodes compared to the corresponding HF diodes. This results in a larger depleted active volume and therefore contributes to higher leakage current at the same reverse voltage bias.

Across all studied electrical characteristics, thinner diodes are observed to be more radiation hard. The 120 μm diodes show higher CCE, lower saturation voltage, and lower leakage current than thicker diodes irradiated to similar fluences. In the CMS detector, thicker sensors are preferred because they produce a larger signal, corresponding to increasing charge collection, due to their larger active volume. However, the performance of thicker diodes decreases rapidly with increasing fluence as observed. The placement of sensors with different thicknesses in the HGCAL is therefore essential to optimise the detector signal-to-noise ratio throughout the HL-LHC phase.

As a result of this study, the understanding of the expected behaviour of the electrical characteristics of silicon sensors in the HGCAL during the 10-year operation of the HL-LHC has been improved.

6.2 Limitations and Future Work

The main limitation of this thesis was the time limitations of measurements. At the start of the study, each IVCV & TCT measurement required approximately 115 min, which halfway through was reduced to 90 min through optimisation of the TCT acquisition. Approximately 400 measurements were performed, corresponding to a total measurement time of about 700 h. As shown in the CCE analysis in §5.1, clear annealing time optima are not reached for all diodes, indicating that additional data points would be required to draw entirely accurate conclusions on the CCE annealing time optima.

The comparison of leakage current damage rate is affected by limitations of the saturation voltage extraction. The saturation voltage obtained from CV measurements is frequency dependent, whereas extraction from TCT data is limited by the number of data points and by the voltage limit. Extracting the leakage current at the saturation voltage would yield more accurate α values, but it would increase the risk of charge multiplication and runaway leakage current. Increasing the voltage limit above 900 V would involve further risks of damaging diodes exposed to higher fluences, as the leakage current could exceed 100 μA . These limitations decrease the precision of the α analysis.

Further research at the microscopic level is required to better understand the effects of in between annealing and multiple rounds of irradiation when some defects have already been annealed. This understanding would clarify the observed shifts in annealing time optima and the origin of both beneficial and negative effects on the electrical characteristics.

Bibliography

- [1] Michael Benedikt et al. *LHC Design Report*. CERN Yellow Reports: Monographs. Geneva: CERN, 2004. DOI: 10.5170/CERN-2004-003-V-3.
- [2] CMS Collaboration. *CMS Luminosity - Public Results*. 2025. URL: https://twiki.cern.ch/twiki/bin/view/CMSPublic/LumiPublicResults#Full_summary_proton_proton_colli.
- [3] Carsten Burgard. *Standard model of physics*. 2016. URL: <https://texample.net/model-physics/>.
- [4] Serguei Chatrchyan et al. “Observation of a new boson at a mass of 125 GeV with the CMS experiment at the LHC”. In: *Physics Letters B* 716.1 (2012), pp. 30–61. DOI: 10.1016/j.physletb.2012.08.021.
- [5] Georges Aad et al. “Observation of a new particle in the search for the Standard Model Higgs boson with the ATLAS detector at the LHC”. In: *Physics Letters B* 716.1 (2012), pp. 1–29. DOI: 10.1016/j.physletb.2012.08.020.
- [6] CERN LHC Commissioning. *Longer term LHC schedule*. 2024. URL: <https://lhc-commissioning.web.cern.ch/schedule/LHC-long-term.htm>.
- [7] CMS Collaboration. *The Phase-2 Upgrade of the CMS Endcap Calorimeter*. Tech. rep. Geneva: CERN, 2017. DOI: 10.17181/CERN.IV8M.1JY2.
- [8] CMS Collaboration. *Detector*. URL: <https://cms.cern/detector>.
- [9] CMS Collaboration. *The CMS magnet project*. Technical design report. CMS. Geneva: CERN, 1997. DOI: 10.17181/CERN.6ZU0.V4T9.
- [10] Nicola Amapane and Vyacheslav Klyukhin. “Development of the CMS Magnetic Field Map”. In: *Symmetry* 15.5 (2023), p. 1030. DOI: 10.3390/sym15051030.
- [11] CMS Collaboration. *The CMS tracker system project*. Technical design report. CMS. Geneva: CERN, 1997. URL: <https://cds.cern.ch/record/368412>.
- [12] CMS Collaboration. *The CMS electromagnetic calorimeter project*. Technical design report. CMS. Geneva: CERN, 1997. URL: <https://cds.cern.ch/record/349375>.
- [13] CMS Collaboration. *The CMS hadron calorimeter project*. Technical design report. CMS. Geneva: CERN, 1997. URL: <https://cds.cern.ch/record/357153>.
- [14] CMS Collaboration. *The CMS muon project*. Technical design report. CMS. Geneva: CERN, 1997. URL: <https://cds.cern.ch/record/343814>.
- [15] CMS collaboration. “Particle-flow reconstruction and global event description with the CMS detector”. In: *Journal of Instrumentation* 12.10 (2017), P10003. DOI: 10.1088/1748-0221/12/10/p10003.
- [16] CMS Collaboration. *Technical Proposal for the Phase-II Upgrade of the CMS Detector*. Tech. rep. Geneva: CERN, 2015. DOI: 10.17181/CERN.VU8I.D59J.

- [17] CMS Collaboration. *Cutaway and highlighted views of CMS Phase 2 detectors rendered in SketchUp*. © 2025 CERN, for the benefit of the CMS Collaboration. 2025. URL: <https://cds.cern.ch/record/2942124>.
- [18] David Barney. *Overview slide of CE with main parameters*. 2022. URL: <https://cms-docdb.cern.ch/cgi-bin/PublicDocDB>ShowDocument?docid=13251>.
- [19] John Wiley & Sons. *Wafer Manufacturing*. 1st. Chichester, UK: Wiley & Sons Ltd, Jan. 2021, p. 304. ISBN: 978-0-470-06121-3.
- [20] Erica Brondolin. “Silicon sensors for the CMS HGCAL upgrade: Challenges, sensor design & electrical characterization”. In: *Journal of Instrumentation* 15.05 (2020), p. C05068. DOI: [10.1088/1748-0221/15/05/c05068](https://doi.org/10.1088/1748-0221/15/05/c05068).
- [21] Leena Diehl et al. *Temperature dependence of the long-term annealing behavior of neutron irradiated diodes from 8-inch p-type silicon wafers*. 2025. arXiv: 2512.16643.
- [22] Hermann Kolanoski and Norbert Wermes. *Particle Detectors*. Oxford University Press, 2020. ISBN: 978-0-19-885836-2.
- [23] Frank Hartmann. *Evolution of Silicon Sensor Technology in Particle Physics*. Springer, 2017. ISBN: 978-3-319-64434-9.
- [24] Manfred Krammer and Frank Hartmann. *Silicon Detectors*. CERN EDIT School Lecture Notes, 2011. <https://indico.cern.ch/event/124392/contributions/1339904/attachments/74582/106976/IntroSilicon.pdf>. 2011.
- [25] Michael Moll. “Radiation damage in silicon particle detectors: Microscopic defects and macroscopic properties”. DESY-THESIS-1999-040. PhD Thesis. Hamburg University, Germany, 1999.
- [26] Yo Shi et al. “A numerical study of cluster center formation in neutron-irradiated silicon”. In: *Journal of Applied Physics* 67.2 (1990), pp. 1116–1118. DOI: [10.1063/1.345799](https://doi.org/10.1063/1.345799).
- [27] Victor Albert Joseph van Lint. *Mechanisms of Radiation Effects in Electronic Materials*. A Wiley-Interscience publication v. 1. Wiley, 1980. ISBN: 9780471041061.
- [28] Renate Wunstorf. “Systematische Untersuchungen zur Strahlenresistenz von Silizium-Detektoren für die Verwendung in Hochenergiephysik-Experimenten”. DESY-2013-00725. PhD Thesis. Hamburg University, Germany, 1992.
- [29] Ioana Pintilie et al. “Stable radiation-induced donor generation and its influence on the radiation tolerance of silicon diodes”. In: *Nuclear Instruments and Methods in Physics Research Section A: Accelerators, Spectrometers, Detectors and Associated Equipment* 556.1 (2006), pp. 197–208. DOI: [10.1016/j.nima.2005.10.013](https://doi.org/10.1016/j.nima.2005.10.013).
- [30] Oliwia Kaluzińska. *Silicon sensor characterisation and radiation hardness qualification for the CMS Endcap Calorimeter Upgrade for the High-Luminosity LHC*. 2022. DOI: [10.17181/yb129-ycg21](https://doi.org/10.17181/yb129-ycg21).
- [31] Marie Christin Mühlnikel. *Bulk radiation hardness and annealing studies of silicon sensors for the CMS endcap calorimeter upgrade*. 2024. URL: <https://repository.cern/records/mfbrj-7j897>.
- [32] Hamamatsu Photonics K.K. *Hamamatsu Photonics Official Website*. <https://www.hamamatsu.com/eu/en.html>.

- [33] CMS Collaboration. “The silicon sensors for the High Granularity Calorimeter of CMS”. In: *Nuclear Instruments and Methods in Physics Research Section A: Accelerators, Spectrometers, Detectors and Associated Equipment* 978 (2020), p. 164428. DOI: [10.1016/j.nima.2020.164428](https://doi.org/10.1016/j.nima.2020.164428).
- [34] Viktoria Hinger. *Silicon sensor process quality control for the CMS phase-2 upgrade*. 2021. DOI: [10.34726/hss.2021.47360](https://doi.org/10.34726/hss.2021.47360).
- [35] Vijay Mishra, VD Srivastava, and SK Kataria. “Role of guard rings in improving the performance of silicon detectors”. In: *Pramana* 65.2 (2005), pp. 259–272. DOI: [10.1007/BF02898614](https://doi.org/10.1007/BF02898614).
- [36] Luka Snoj, Gašper Žerovnik, and Andrej Trkov. “Computational analysis of irradiation facilities at the JSI TRIGA reactor”. In: *Applied Radiation and Isotopes* 70.3 (2012), pp. 483–488. DOI: [10.1016/j.apradiso.2011.11.042](https://doi.org/10.1016/j.apradiso.2011.11.042).
- [37] Kleman Ambrožič, Gašper Žerovnik, and Luka Snoj. “Computational analysis of the dose rates at JSI TRIGA reactor irradiation facilities”. In: *Applied Radiation and Isotopes* 130 (2017), pp. 140–152. DOI: [10.1016/j.apradiso.2017.09.022](https://doi.org/10.1016/j.apradiso.2017.09.022).
- [38] Jan Kieseler et al. “Isothermal annealing of radiation defects in silicon bulk material of diodes from 8” silicon wafers”. In: *Journal of Instrumentation* 18.09 (2023), P09010. DOI: [10.1088/1748-0221/18/09/P09010](https://doi.org/10.1088/1748-0221/18/09/P09010).
- [39] Particulars. *Particulars - Advanced Measurement Systems*. <https://particulars.si/index.php>.
- [40] Oliwia Agnieszka Kałuzińska et al. “Annealing behaviour of charge collection of neutron irradiated diodes from 8-inch p-type silicon wafers”. In: *Journal of Instrumentation* 20.06 (2025), P06054. DOI: [10.1088/1748-0221/18/09/P09010](https://doi.org/10.1088/1748-0221/18/09/P09010).
- [41] Max Andersson. *Particulars Setup & Visual Inspection of HGCAL using AI*. 2024. URL: <https://repository.cern/records/g2kdj-4y468>.
- [42] CERN LHC Commissioning. *Luminosity forecasts*. 2024. URL: <https://lhc-commissioning.web.cern.ch/schedule/HL-LHC-plots.htm>.

A.1 Schedule and Expected Integrated Luminosity of LHC & HL-LHC

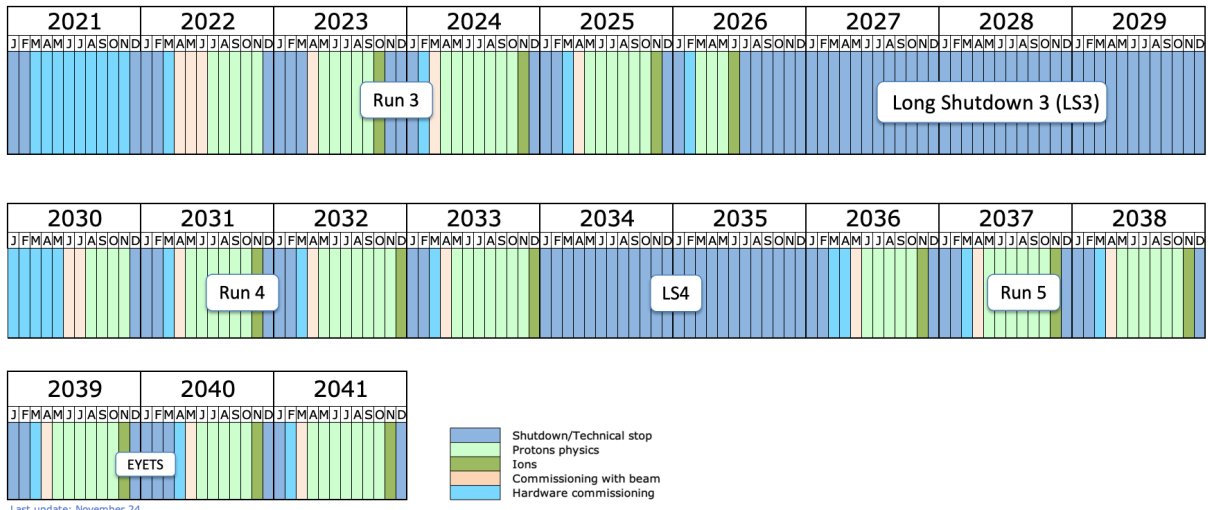


Figure A.1.1: Long-term schedule of LHC and HL-LHC operation. The LHC is planned to be upgraded to HL-LHC during Long Shutdown 3. Credit: [6].

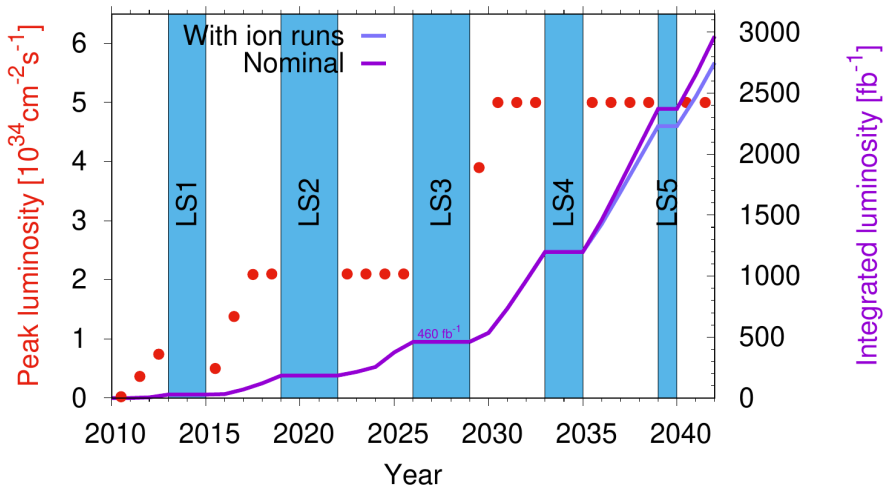


Figure A.1.2: Expected peak and integrated luminosity from 2010 to 2042. The HL-LHC is planned to begin operation after Long Shutdown 3 and to reach an integrated luminosity of 3000 fb^{-1} over ten years. Credit: [42].

A.2 Leakage Current Deviation from IVCV Probe Station

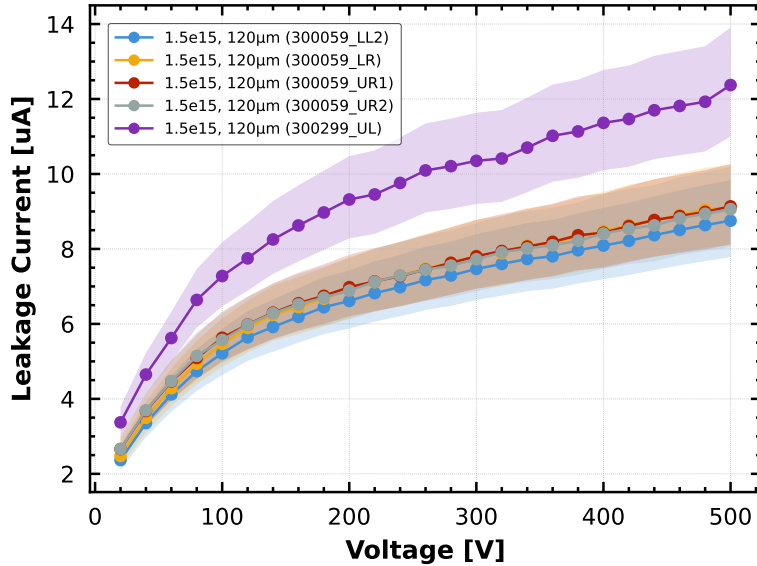


Figure A.2.1: Subset of initial IV measurements of the DI campaign with no additional annealing except for the in-reactor annealing. Measurements were performed in the IVCV probe station setup at $-20\text{ }^{\circ}\text{C}$ with an uncertainty of $\pm 1\text{ }^{\circ}\text{C}$.

Leakage current deviation is shown in Figure A.2.1 for a subset of the DI campaign with a fluence of $1.5 \cdot 10^{15} \text{ n}_{\text{eq}}/\text{cm}^2$ and a thickness of $120\text{ }\mu\text{m}$. The diode with ID 300299_UL deviates from the rest beyond the expected spread from fluence uncertainties of 10% and was therefore excluded from further measurements in the IVCV & TCT setup. A similar selection procedure was applied to the whole dataset, including the initial CV measurements.

A.3 Charge Collection Efficiency at 400 V and 800 V

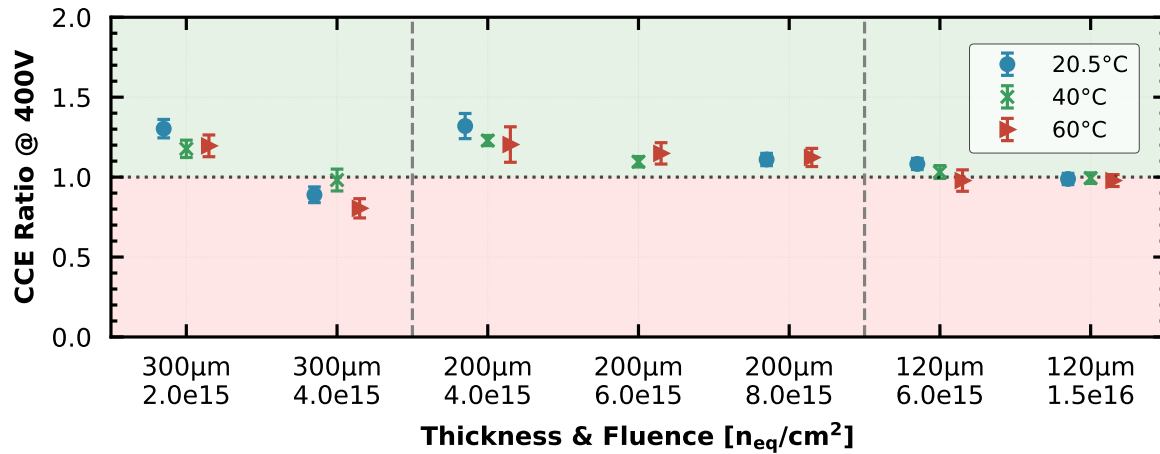


Figure A.3.1: The average DI SR/HF ratio of the CCE at 400 V, calculated over all annealing times for each unique combination of annealing temperature, thickness, and fluence.

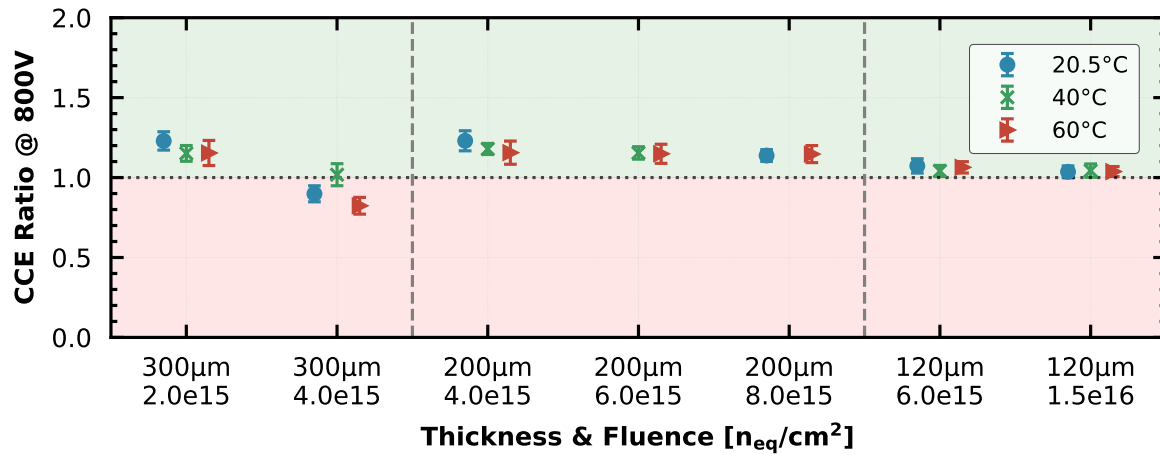


Figure A.3.2: The average DI SR/HF ratio of the CCE at 800 V, calculated over all annealing times for each unique combination of annealing temperature, thickness, and fluence.

A.4 Electrical Characteristics Ratios with Shifted Annealing Time

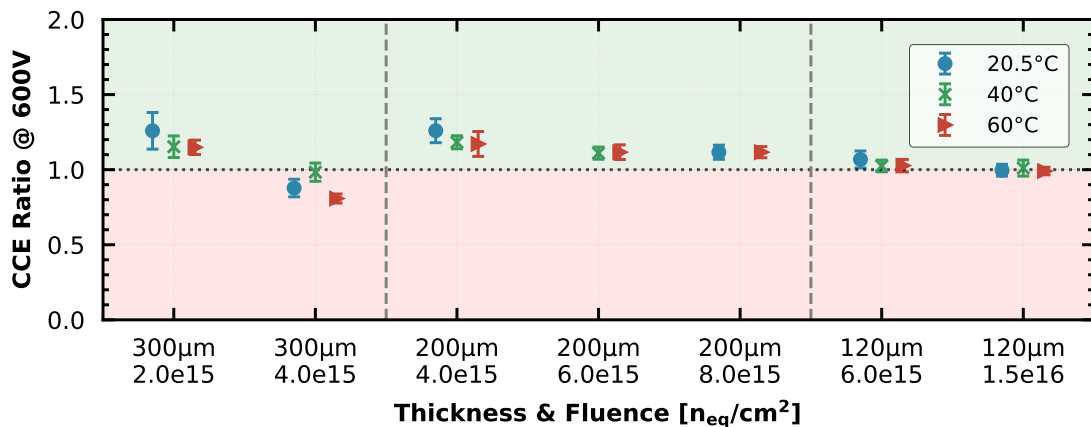


Figure A.4.1: CCE ratio at 600 V with 1/4 of the DI annealing time added to DI SR.

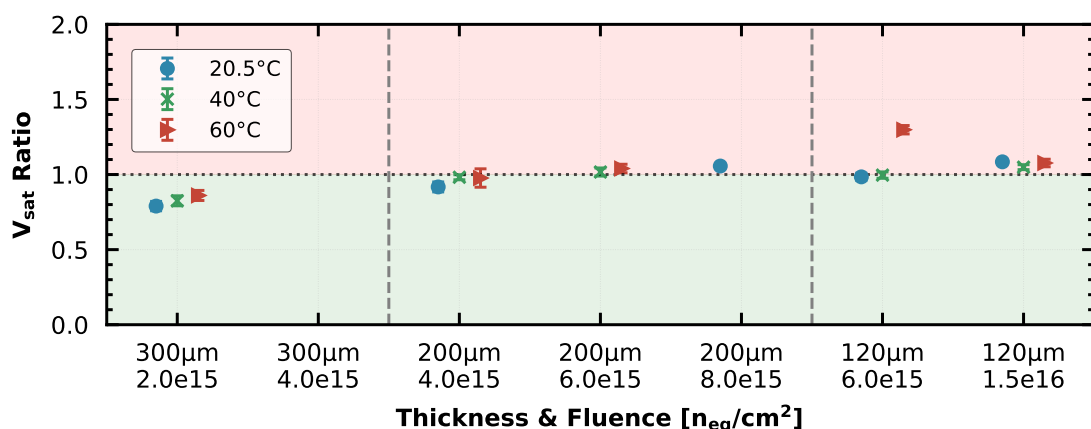


Figure A.4.2: Saturation voltage ratio with 1/4 of the DI annealing time added to DI SR.

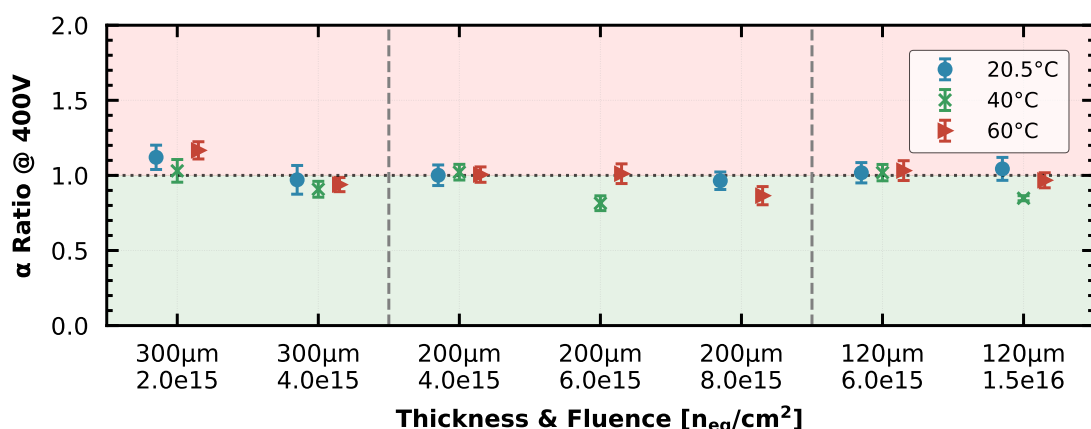


Figure A.4.3: Alpha ratio at 400 V with 1/4 of the DI annealing time added to DI SR.